

DESIGN OF INSTRUMENTATION AND METHODOLOGIES FOR
DETERMINATION OF FREE NEUTRON CHARACTERISTICS

A DISSERTATION IN

Physics

and

Mathematics

Presented to the Faculty of the University
of Missouri-Kansas City in partial fulfillment of
the requirements for the degree

DOCTOR OF PHILOSOPHY

by

CORY BLAKE HOSHOR

B.S. in Mathematics and Statistics, University of Missouri-Kansas City, 2012

M.S. in Physics, University of Missouri-Kansas City, 2016

Kansas City, Missouri

2017

DESIGN OF INSTRUMENTATION AND METHODOLOGIES FOR
DETERMINATION OF FREE NEUTRON CHARACTERISTICS

Cory Blake Hoshor, Candidate for the Doctor of Philosophy Degree

University of Missouri-Kansas City, 2017

ABSTRACT

Measuring neutron source-dependent free neutron properties over a large neutron energy range, with human-portable instrumentation, continues to push the frontier of neutron detection instrumentation design and analysis techniques. In addition, a variety of nuclear nonproliferation and health physics applications require instrumentation that can provide free neutron property measurement and analysis in real time. To overcome the challenges inherent to these applications and advance the state of the current art in neutron detection instrumentation, the first representatives of a new class of solid-state moderating-type neutron spectrometer have been designed, modeled, fabricated, and tested. This work introduces state-of-the-art human-portable instruments by discussing the fundamental theory of their operation, investigating and analyzing—via Monte Carlo simulation—the principle considerations for optimal instrument design, and empirically evaluating the capability of each of the fabricated spectrometers to meet the application needs. Utilizing the unique three-

dimensional neutron thermalization information afforded by this new class of instrumentation, novel algorithmic methodologies are introduced to determine free neutron characteristics of interest to the aforementioned applications in real time.

APPROVAL PAGE

The faculty listed below, appointed by the Dean of the College of Arts and Sciences have examined a dissertation titled “Design of Instrumentation and Methodologies for Determination of Free Neutron Characteristics,” presented by Cory Blake Hoshor, candidate for the Doctor of Philosophy degree, and certify that in their opinion it is worthy of acceptance.

Supervisory Committee

Anthony Caruso, Ph.D., Committee Chair
Department of Physics and Astronomy

Paul Rulis, Ph.D.
Department of Physics and Astronomy

Mark Brodwin, Ph.D.
Department of Physics and Astronomy

Xianping Li, Ph.D.
Department of Mathematics and Statistics

Kamel Rekab, Ph.D.
Department of Mathematics and Statistics

CONTENTS

ABSTRACT	iii
ILLUSTRATIONS	ix
TABLES	xiii
ACKNOWLEDGEMENTS	xiv
Chapter	
1. INTRODUCTION	1
1.1 Research Motivation	1
1.2 Free Neutron Interactions with Matter	2
2. METHODS	4
2.1 MCNP Simulation	4
2.2 Experimental Methods	6
2.3 Time-Dependent Certainty of Source Detection above Background	13
3. DESIGN, OPTIMIZATION, AND TESTING OF FOUR MODERATING-TYPE NEUTRON SPECTROMETERS	22
3.1 Introduction	22
3.2 Instrument Design and Optimization	23
3.3 Instrument Builds and Testing	48
3.4 Conclusions	64
4. METHODS FOR REAL-TIME SOURCE LOCALIZATION AND IDENTIFICATION WITH A MODERATING-TYPE NEUTRON SPECTROMETER	67
4.1 Introduction	67

4.2 Neutron Response Vectorization (NRV) Method for Determining Neutron Source Location	69
4.3 Pearson Product-Moment Cross-Correlation Spatial Response Analysis Techniques for Neutron Source Identification	80
4.4 Extension of 2-D & 3-D Pearson Cross-Correlation Methods: Simultaneous Neutron Source Localization and Identification	92
4.5 Post-Hoc Improvement to the NRV Method: NRV-Poly Method	98
4.6 Conclusions and Recommendations for Future Work	103
5. ENHANCED KERNEL HILBERT SPACE TEMPLATE-MATCHING TECHNIQUES FOR SIMULTANEOUS NEUTRON SOURCE LOCALIZATION AND IDENTIFICATION	106
5.1 Introduction	106
5.2 Kernel Principle Component Analysis (KPCA)	110
5.3 Simulation Testing and Comparison of KPCA Template-Matching Algorithms	128
5.4 Conclusions and Recommendations for Future Work	141
6. METHODS FOR NEUTRON ENERGY SPECTRUM UNFOLDING	144
6.1 Motivation and Conceptual Introduction	144
6.2 Neutron Spectrum Unfolding Problem	145
6.3 Maximum Entropy Method (MEM) Unfolding with the 6C Spectrometer	149
6.4 Machine Learning Method Employing Artificial Neural Networks	159
7. REVIEW OF CONCLUSIONS AND FUTURE RECOMMENDATIONS	166
REFERENCES	173

VITA	181
------------	-----

ILLUSTRATIONS

Figure	Page
2.1.1. Example MCNP Instrument Simulation	5
2.2.1. Experimental Setup for the Shadow Shield Method	7
2.2.2. Experimental Setup for Horizontal-Planar Angular Orientation Testing	11
2.3.1. Conceptual Illustration of Gaussian Probability Distributions	19
3.2.1. Conceptual Illustrations of Moderating Media	25
3.2.2. Heuristic Illustration of the Thermalized Neutron Intensity Distribution	27
3.2.3. 5C Neutron Spectrometer Conceptual Illustration #1	29
3.2.4. 5C Neutron Spectrometer Conceptual Illustration #2	29
3.2.5. Renderings of the Cylindrical and Rectangular Prism Moderator Geometries	34
3.2.6. Results of the Simulated Intrinsic Neutron Detection Efficiency to Bare ^{252}Cf for the Rectangular Prism and Cylindrical Geometries	34
3.2.7. Simulated Instrument Intrinsic Detection Efficiency to ^{252}Cf as a function of MSND Thermal Neutron Detection Efficiency	37
3.2.8. Intrinsic Neutron Detection Efficiency to ^{252}Cf as a Function of Detector Layer (Diode) Radius for Varying Detector-to-Moderator Radius Ratios	39
3.2.9. Normalized Detector-Board-Summed Response Functions for Instrument Models with Various Moderator Materials	41
3.2.10. Instrument Intrinsic Efficiency to ^{252}Cf as a Function of Moderator Radius and Thickness for Various Moderator Materials	44

3.2.11. Pearson Cross-Correlation Between ^{252}Cf and AmBe Instrument Responses as a Function of Moderator Radius and Thickness for Various Moderator Materials	46
3.3.1. Photographs and Renderings of the 5C Spectrometer	48
3.3.2. Photographs and Renderings of the 6C Spectrometer	50
3.3.3. 6C Spectrometer Intrinsic Efficiency to ^{252}Cf and Pearson Cross-Correlation Between ^{252}Cf and AmBe 6C Spectrometer Responses as a Function of HDPE Moderator Radius and Thickness	51
3.3.4. Photographs and Renderings of the 4RP Spectrometer	53
3.3.5. Photographs and Renderings of the 4C Spectrometer	54
3.3.6. Simulated and Measured Intrinsic Efficiency to Bare ^{252}Cf for Each Spectrometer Model	56
3.3.7. 5C Spectrometer Simulated Relative Intrinsic Efficiency, Simulated Relative Absolute Efficiency, and Experimental Relative Absolute Efficiency to Bare ^{252}Cf , as a Function of Neutron Incident Angle	58
3.3.8. Neutron Source Identification Experimental Setup	60
3.3.9. Neutron Source Identification Experiment Summary Plot	62
4.1.1. Simulated Examples of 6C Spectrometer Responses to a Bare ^{252}Cf Neutron Source	68
4.2.1. Neutron Response Vectorization (NRV) Method Illustrations	73
4.2.2. Summery Plot of 6C Empirical Test Results for Determining Source-to-Spectrometer Angular Orientation in the Horizontal Plane Using the NRV Method	79

4.3.1. Example of a 1-Dimensional Cross-Correlation Data Grouping	84
4.3.2. Example of a 2-Dimensional Cross-Correlation Data Grouping	85
4.3.3. Screen Shot from the 6C Spectrometer Software	88
4.3.4. Summary Plot of Empirical Source Identification Results	90
4.4.1. Example of the Alternative 2-Dimensional Cross-Correlation Data Grouping	93
4.4.2. Illustration of 6C Spectrometer Cross-Sectional Areas	95
4.5.1. NRV-Poly Method Function Fitting	100
4.5.2. Desired NRV-Poly Method Characterization	101
4.5.3. Example NRV-Poly Method Output Plots	102
5.2.1. Contour Plot of Correlation Kernel Function Values as a Function of Pearson Correlation Coefficient Between Vectors x_i and x_j and Possible Values for the Adjustable Parameter γ	118
5.2.2. Example Illustration of 3D and 2D Descriptions of a Typical 6C Spectrometer Response	123
5.3.1. Simulation Test Illustrations	129
5.3.2. 3D Correlation KPCA Template-Matching Algorithm Simulation Test Results	131
5.3.3. 3D Cosine KPCA Template-Matching Algorithm Simulation Test Results	133
5.3.4. 2D Correlation KPCA Template-Matching Algorithm Simulation Test Results	135
5.3.5. 2D Cosine KPCA Template-Matching Algorithm Simulation Test Results	137

5.3.6. Summary Plots of KPCA Template-Matching Algorithm	
Simulation Test Results	139
5.3.7. Plot of the Simulated Neutron Energy Spectra	140
6.3.1. Photograph of the Experimental MEM Test Setup at KSU	155
6.3.2. Maximum Entropy Method Unfolding Algorithm Results	157
6.4.1. Artificial Neural Network Construction	160
6.4.2. ANN Method Applied to ^{252}Cf Training Set Data	161
6.4.3. ANN Method Applied to AmBe Training Set Data	162
6.4.4. ANN Method Applied to Pu Metal Training Set Data	163
6.4.5. ANN Method Applied to Simulated PuBe Measurement Data	164

TABLES

Table	Page
3.2.1. Potential Instrument Moderator Material Salient Properties	43

ACKNOWLEDGMENTS

This work was funded by the Office of Naval Research, award nos. N00014-11-1-0157 and N00014-13-1-0402, and by the Defense Threat Reduction Agency, award no. HDTRA1-14-P-005.

To Heidi and Vada, my beautiful girls, with all my heart

God only knows what I'd be without you

CHAPTER 1

INTRODUCTION

1.1. Research Motivation

Instruments with the ability to passively detect sources of neutron radiation and determine characteristics of their free neutron emissions are of interest (and need) in a wide variety of nonproliferation, medical physics, and pure physics applications. Although great need for such technology has existed within government, private, and academic sectors since James Chadwick first discovered the neutron in 1932, no portable instrument has yet been able to accurately spectroscopically characterize the radiative neutron emissions from nuclear reactions over the entire energy range of interest to these applications, which covers many orders of magnitude (from < 25 meV to > 20 MeV). To directly measure characteristics of radiative neutron emissions, a detection mechanism would require the utilization of interactions that are based on intrinsic properties of free neutrons, such as translational momentum, spin, magnetic moment, and/or the (proposed) electric dipole moment [1]; however, energy transduction via intrinsic neutron properties is currently impractical due to insufficient interaction energy and/or significant technological immaturity. Therefore, the majority of both traditional and state-of-the-art technologies rely on indirect (higher-order) strong force interactions to detect free neutrons, and subsequent data analysis is necessary to determine one or more of their characteristic properties (e.g., the energy spectrum, direction of incidence, source of emission, etc.). Since current art does not allow for direct measurement of such properties, one must infer the desired information from measured quantities that are only indirectly related, and the complexity of this process increases when utilizing higher-order (3rd order, 4th order, etc.) interaction mechanisms, which is often the

most pragmatic means. Making such inferences on characteristic free neutron properties requires shrewdly designed, and rigorously optimized, instrumentation, coupled with sophisticated data analysis techniques that should be established upon a solid mathematical framework, and developed from intimate knowledge of the physics of neutron transport and the fundamental interactions upon which the indirect measurements are based. The interdisciplinary nature of this research is therefore ubiquitous and unambiguous throughout this work; seeking meaningful mathematical connections between empirical measurements of free neutrons and their fundamental properties, through a comprehensive understanding of the physics of radiative neutron emission and subsequent nuclear interactions of free neutrons with matter.

1.2. Free Neutron Interactions with Matter

There are two primary categories of free neutron interactions with atomic nuclei, scattering and absorption. Neutron scattering interactions occur when a portion of a free neutron's kinetic energy is transferred to a target nucleus; these interactions are subcategorized as either elastic or inelastic. In elastic scattering interactions, (n, n) , this portion of the free neutron's initial kinetic energy is transferred entirely in the form of nucleus recoil kinetic energy, such that the total kinetic energy of the neutron-nucleus system is conserved (analogous classical elastic collisions, e.g., billiard balls). In inelastic scattering interactions, (n, n') , some portion of the neutron's kinetic energy is transferred in the form of nucleus recoil kinetic energy, and some portion is transferred in the form of nuclear excitation, such that momentum is conserved, but kinetic energy is not conserved for the neutron-nucleus system. As the name suggests, neutron absorption interactions occur when a free neutron is absorbed into a target nucleus; these interactions can be described in four

subcategories, based upon how the compound nucleus de-excites after neutron absorption: radiative capture, neutron-induced fission, neutron emission (or neutron multiplicity), and charged particle emission. In radiative capture, (n, γ) , the nucleus de-excites by emitting one or more gamma-rays (defined here as photons emitted from an atomic nucleus). For fissionable isotopes, a neutron absorption interaction can induce a nuclear fission reaction, (n, f) , in which the compound nucleus de-excites by splitting into two smaller nuclei (called fission fragments), simultaneously emitting one or more neutrons and/or gamma-rays (called “prompt” neutron/gamma-ray emissions). Subsequent decay of the fission fragments can result in a variety of “delayed” particle emissions as well, depending on the fragment nuclei produced. In neutron emission (or neutron multiplicity) interactions, (n, n^*) , $(n, 2n)$, $(n, 3n)$, etc., a compound nucleus (after absorbing a free neutron) de-excites by emitting one or more neutrons. Finally, in charged particle emission, the nucleus de-excites by emitting one or more charged particles, such as alpha particles (i.e., ${}^4\text{He}$ nuclei), (n, α) , protons, (n, p) , deuterons (i.e., ${}^2\text{H}$ nuclei), (n, d) , tritons (i.e., ${}^3\text{H}$ nuclei), (n, t) , etc. Note: free neutrons are not stable particles; they have an average lifetime of approximately 14.76 minutes. If a free neutron is not absorbed by an atomic nucleus, it will eventually beta-decay into a proton, emitting a beta particle (i.e., a high-energy free electron), and an antineutrino ($n \rightarrow p + e^- + \bar{\nu}$).

CHAPTER 2

METHODS

2.1. MCNP Simulation

Throughout this work, the Monte Carlo N-Particle transport code (MCNP), written and maintained by researchers at Los Alamos National Laboratory [2-5], will be used extensively to simulate the transport of free neutrons and their progeny, for the design, evaluation, and testing of the instruments and methodologies introduced herein. Although this code may be used to simulate a wide variety of radiation transport scenarios, instead of describing MCNP itself in detail, this section will provide a brief description of the primary way in which the code will be used in subsequent chapters. For the majority of the simulations described herein, first, a three-dimensional MCNP instrument model is created by defining the geometry (and absolute position in space), isotopic composition, and density of all instrument components in as much detail as reasonably possible (Fig. 2.1.1). Once an instrument model is defined, a point or planer approximation (in most cases) of a neutron source of interest to a particular simulation is created, by defining its position (or distribution of possible positions), neutron emission energy (or distribution of possible neutron energies, i.e., energy spectrum), and emission direction (or distribution of possible directions, assumed to be isotropic in most simulations described herein, a cone of possible directions is shown in Fig. 2.1.1B). With an instrument model and neutron radiation source defined, a large number of particle “histories” are simulated individually (the first 100 particle histories of an example simulation are shown as green lines, called particle tracks, in Fig. 2.1.1B, with small red dots indicating where individual histories terminated via neutron absorption). For each particle history, a single neutron, as well as any of its progeny, is transported from the

defined neutron source through the problem geometry, with each nuclear interaction (as described in section 1.2) determined using cross section data from the Evaluated Nuclear Data Files (ENDF, [6]) and/or nuclear physics models. For the majority of simulations in this work, the desired information was the instrument’s detector response. This was obtained by recording, or “tallying”, the number of neutron absorptions, specifically (n, t) reactions, occurring within the instrument model’s individual detectors throughout the simulation.

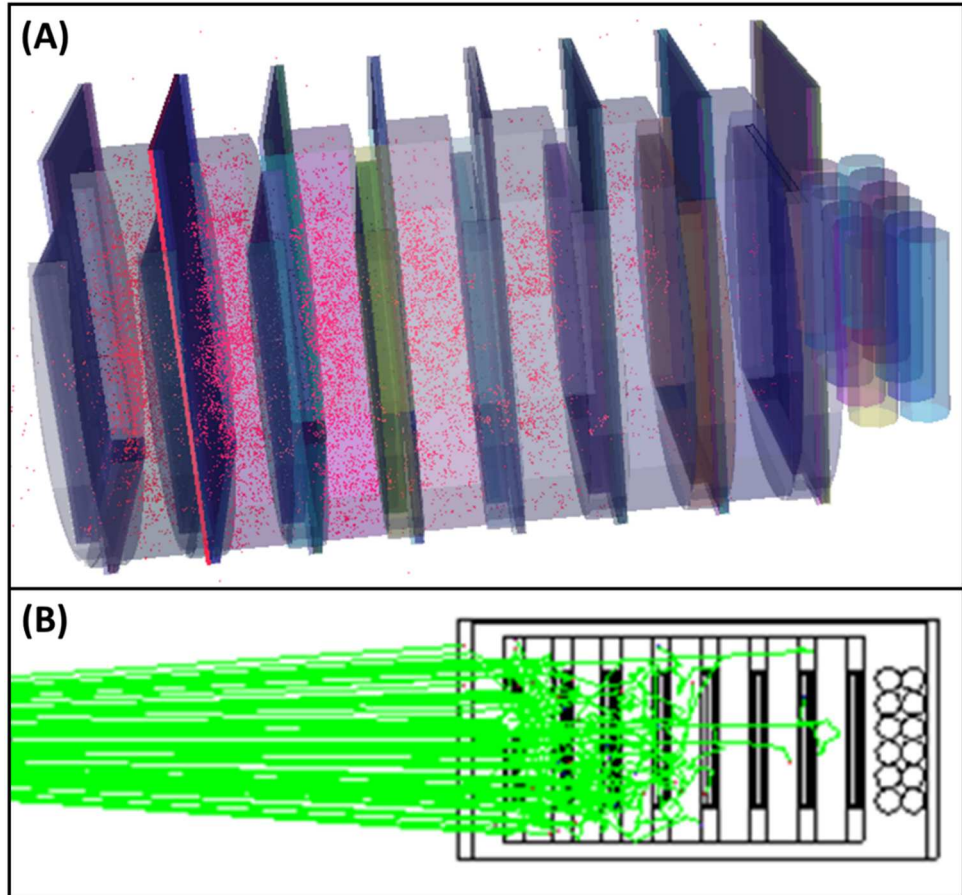


Figure 2.1.1: Example MCNP instrument simulation, showing (A) a 3D model (MCNP VISED) of the active portion of an instrument’s active volume (instrument case not shown), with small red dots indicating simulated neutron interactions, and (B) a 2D view (MCNP VISED) of the 3D model shown in (A) (instrument case shown), with green lines representing individual particle tracks, and small red dots indicating the termination of each track.

2.2. Experimental Methods

2.2.1. Shadow Shield Method for Environmental Scatter Correction

When making empirical measurements of free neutron radiation, regardless of the instrumentation used, one must consider the ways in which neutron interactions in the local environment can negatively affect the experiment. For many instrument measurements, environmental neutron scattering interactions are responsible for the largest detrimental effect, often referred to in the field as “room scatter” or “room return” (“floor shine” is another commonly used term). The “Room scatter” effect occurs when some portion of the free neutrons detected by the instrument, after being emitted from a source-type of interest to the measurement, undergo one or more elastic scattering interactions with nuclei of atoms in the local environment (e.g., floor, walls, ceiling, objects, or even air), altering one or more of the neutron’s fundamental characteristics of interest to the measurement (e.g., neutron energy loss and/or change in direction). This section discusses how a shadow shield (Fig. 2.2.1B), when available, can be used to correct for these environmental scattering effects.

Since the instruments introduced in this work were primarily designed for applications in which local environmental conditions are not practically controllable (i.e., outside of the laboratory), the instruments themselves (detailed in section 3), and the analysis techniques applied to their measurements (detailed in sections 3-5), were designed to limit the negative effects of environmental neutron scatter as much as possible, without sacrificing instrument performance and without the use of any additional tools (e.g., a shadow shield). Thus, the shadow shield method was *not* used for any empirical tests of algorithms intended for implementation in an instrument’s software (i.e., algorithms intended for use outside of the laboratory), but *was* used for empirical tests of algorithms intended for use in laboratory

environments (e.g., neutron energy spectrum unfolding algorithms, section 6), and for experimental measurements of intrinsic instrument properties (e.g., efficiency), when applicable.



Figure 2.2.1: Experimental setup for the shadow shield method, showing (A) an unshielded ^{252}Cf spontaneous fission neutron source (circled in red) aligned with the central axes of both (B) a cylindrical shadow shield, and the cylindrical active volume of (C) the 6C neutron spectrometer.

By way of example, we will discuss how the shadow shield method is used to empirically determine an instrument’s intrinsic efficiency to a particular neutron source type, defined as the total number of “source neutrons” (i.e., neutrons that travel directly from the source to the instrument) detected over a given measurement time, divided by the number of source neutrons incident on the front face of the instrument’s active volume (i.e., the leftmost circular face of the internal white cylinder in Fig. 2.2.1C) over that measurement time. The shadow shield method is used to approximate the number of source neutrons detected over a given measurement time. This method requires two separate measurements to be taken for the same amount of time.

For the first measurement, as shown in Fig. 2.2.1, the source of interest (Fig. 2.2.1A) is placed at a set distance, d , from the front face of the instrument (Fig. 2.2.1C), and a shadow shield is placed between the source and the instrument. A shadow shield should be designed such that—assuming the source of interest emits neutrons isotropically into 4π sr—it captures (i.e., absorbs) any neutrons that would travel directly from the source to the instrument if the shield were not there, but does not impede any environmentally scattered neutrons from reaching the instrument from other directions (i.e., it is designed to cast a neutron “shadow”, meaning a lack of incident neutrons, on the instrument’s front face). The shadow shield used for the experiments in this work, shown in Fig. 2.2.1B, is a 6"-diameter (same diameter as the circular front face of the instrument’s active volume, shown in Fig. 2.2.1) \times 20"-length cylinder of high-density polyethylene (HDPE, $(C_2H_4)_n$, neutron moderating material) that is wrapped (on the rounded sides) in a 1-cm layer of cadmium (^{113}Cd , thermal neutron absorbing material), and has a 2-cm layer of cadmium on the back face (the circular face closest to the instrument in Fig. 2.2.1); the entire shadow shield is

wrapped in aluminum foil, and is handled with gloves, to avoid skin contact with cadmium. Thus, high-energy source neutrons that enter the front-face of the shadow shield (the circular face closest to the source in Fig. 2.2.1) undergo elastic scattering interactions, and resultant energy loss, with hydrogen and/or carbon nuclei in the HDPE until they are sufficiently thermalized to be absorbed by either hydrogen nuclei in the HDPE or (much more frequently) cadmium nuclei in the outer layers. The total number of neutrons detected in this first measurement is interpreted as an approximation (because no shadow shield can be expected to work perfectly) of the number of detection events due to environmentally scattered neutrons alone, under the experimental conditions of this measurement. For the second measurement, the first measurement is repeated identically, except the shadow shield is removed. The total number of neutrons detected in this second measurement is interpreted as the number of source neutrons detected plus the number environmentally scattered neutrons detected; thus, subtracting the result of the first measurement, $D_{No\ Shield}$, from the result of the second measurement, $D_{No\ Shield}$, provides an estimate for the number of detection events due to source neutrons alone, D_{Source} , and the instrument's intrinsic efficiency to the neutron source type of interest, ε_{Source} , can be approximated by

$$\varepsilon_{Source} \equiv \frac{D_{Source}}{N_{Source}} \cong \frac{D_{No\ Shield} - D_{Shield}}{N_{Source}}. \quad (2.2.1)$$

If the source's neutron emission rate, R_{Source} , is known, the number source neutrons incident upon the instrument's active volume, N_{Source} , can be estimated by

$$N_{Source} = R_{Source} \cdot t \cdot \frac{\Omega}{4\pi}, \quad (2.2.2)$$

where t is the common measurement time and Ω is the source-to-instrument solid angle.

Since the active volume of the instrument shown in Fig. 2.2.1 is cylindrical, it's front face is

circular, such that the source-to-instrument solid angle is that of a cone, with base radius, r , equal to the radius of the instrument's front face, r , height equal to the source-to-instrument distance, d , and apex angle $\theta = \tan^{-1}(r/d)$. This solid angle is given by

$$\Omega = 2\pi(1 - \cos \theta) = 2\pi \left[1 - \cos \left(\tan^{-1} \left(\frac{r}{d} \right) \right) \right], \quad (2.2.3)$$

such that the empirical intrinsic efficiency to the measured source type is calculated by

$$\varepsilon_{Source} \cong \frac{D_{No\ Shield} - D_{Shield}}{R_{Source} \cdot t \cdot \frac{1}{2} \left[1 - \cos \left(\tan^{-1} \left(\frac{r}{d} \right) \right) \right]}. \quad (2.2.4)$$

2.2.2. Experimental Setup for Angular-Orientation Measurements

In this work, multiple algorithmic methodologies are introduced for determining the relative source-to-instrument angular orientation in the horizontal plane. For all empirical tests of these methods, the experimental setup shown in Fig. 2.2.2 was used.

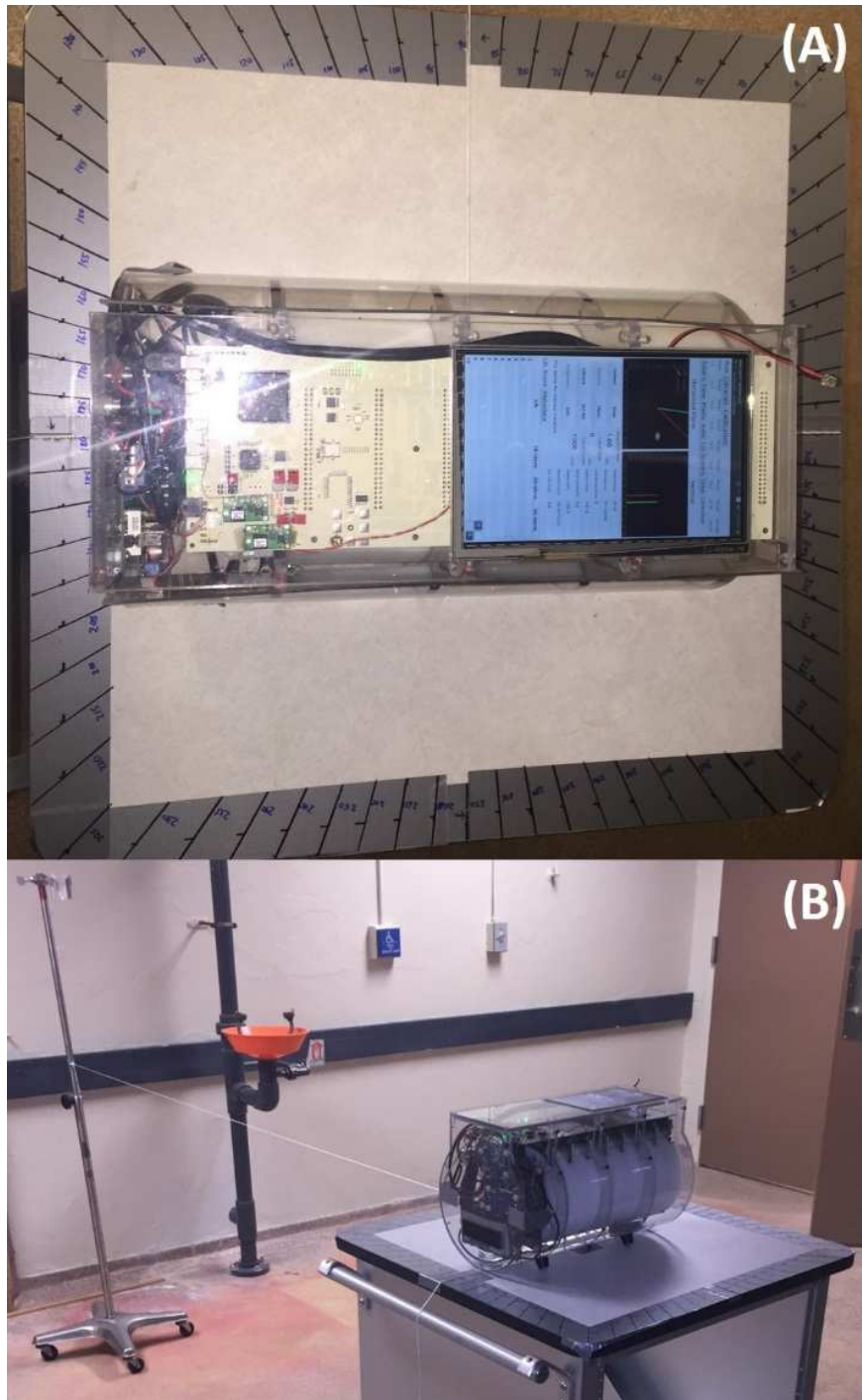


Figure 2.2.2: Experimental setup for horizontal-planar angular orientation testing, showing (A) the 6C neutron spectrometer atop the angular calibration table, with labeled markers indicating relative angular orientations of 0° to 355° in 5° increments (white string indicating 90° orientation), and (B) an alternate view of the experimental setup shown in figure A, (i.e., 90° orientation), showing the neutron source stand with the white fixed-distance angular orientation indicator string attached.

The “angular calibration table”, shown in Fig. 2.2.2A, was constructed by, first, driving a single screw into the exact center of the square tabletop (underneath the instrument in the figure), with the pan head (i.e., rounded top and flat bottom) of the screw left ~0.3 cm above the table’s surface, such that one end of a length of string (white string shown in both Figs. 2.2.2A and 2.2.2B) could be securely looped around the screw’s shank, but with the enough space between the table’s surface and the bottom surface of the screw head to allow the string’s looped end to freely rotate about the shank (without the string winding). The midpoint of one of the tables sides (the right side in Fig. 2.2.2A) was chosen to represent an angular orientation of 0°, and angles were precisely measured from this 0° reference orientation to 355° in 5° increments, and were marked and labeled on duct tape at the edges of the table, as shown in Fig. 2.2.2A. For empirical tests, the instrument is placed on the table, such that its active volume is precisely centered above the screw, and the center of its front face (right face in Fig. 2.2.2A) is aligned with the 0° reference marker. The other end of the length of string was looped around the vertical shaft of a lab stand, vertically even with the table’s surface, such that the string is parallel to the floor when fully extended (Fig. 2.2.2B). Since the lab stand and angular calibration table are both on wheels, the source-to-instrument angular orientation can be adjusted by either moving the lab stand or rotating the table; for the tests in this work, the table was rotated, so that the environmental scattering conditions would remain as consistent as possible between measurements (the shadow shield method was not used for these experiments). The ^{252}Cf spontaneous fission neutron source used for these tests is fixed to the end of a plastic rod, which hangs vertically downward from an adjustable fixture on the lab stand (as shown in Fig. 2.2.1A, Fig. 2.2.2B shows the adjustable fixture at the top of the lab stand with the source + plastic

rod removed). For all the tests conducted for this work, the horizontal-planar position of the source was adjusted with the lab stand fixture such that it was aligned with the string, the vertical position of the source was adjusted with the lab stand fixture such that it was aligned with the vertical center of the instrument's active volume, and the string length was adjusted to maintain a set distance (specified in subsequent experiment descriptions) between the source and the center of the instrument's active volume.

2.3. Time-Dependent Certainty of Source Detection above Background

Regardless of operational scenario, it is always crucial for the operator/interpreter of a neutron detection instrument to be able to discern whether an observed detection intensity is truly due to the presence of a neutron source (i.e., true positive detection), or simply due to instrument noise and/or natural ambient background radiation (i.e., false positive detection). The method derived here, and applied to empirical measurements from various instruments in latter sections, seeks to determine the statistical certainty with which this distinction can be made.

In order to ascertain the distinction we seek, an initial local count rate measurement must be taken when it is known that there is no neutron source present (i.e. any counts registered will not be due to “foreground” neutrons). This count rate measurement, denoted N_B/t_B , embodies the natural ambient neutron background count rate (e.g. the count rate due to cosmic ray-induced spallation neutrons and their progeny) plus any count rate due to instrument noise. From this point forward, this will be simply referred to as the “background count rate”. Assuming that a background measurement has been taken for an acceptable length of time (optimal allocation of background/foreground data collection time is described by Eq. 2.3.2 below), consider a scenario in which an operator uses an instrument to measure

the total count rate, N_T/t_T , from a neutron source of interest in the presence of a steady-state (i.e., static flux) ambient neutron background. To obtain an estimate of the count rate due to the neutron source alone, N_S/t_S , one could simply subtract the background count rate from the total count rate.

$$\frac{N_S}{t_S} = \frac{N_T}{t_T} - \frac{N_B}{t_B} \quad (2.3.1)$$

Now that a distinction has been made between the measured background count rate and the estimated true neutron source count rate (e.g. estimated count rate above ambient background and instrument noise), it is necessary to determine a measure of statistical certainty for our estimation (Eq. 2.3.1). The following derivation is closely related to Glenn Knoll's derivation of the well-known Currie equation for the minimum detectable amount (MDA) of measurable activity [7], but with 2 very important distinctions. First, and most notably, the MDA is not the metric we seek. Instead, we seek a measure of certainty in our estimation of N_S/t_S , as approximated by Eq. 2.3.2. Second, the Currie equation makes the simplifying assumption of equal allocation of time to each measurement ($t_T = t_B$), and this derivation does not. Assuming that a fixed total measurement time is available, $t = t_B + t_T$, it can be shown [7] that the optimal measurement time allocation satisfies the relation

$$\left. \frac{t_T}{t_B} \right|_{optimal} = \sqrt{\frac{N_T/t_T}{N_B/t_B}} = \sqrt{\frac{N_T}{N_B} \cdot \frac{t_B}{t_T}}. \quad (2.3.2)$$

The equal time allocation assumption made in the Currie equation derivation, is thus optimal for situations in which it is expected that $N_S/t_S \ll N_B/t_B$. Since optimal measurement times may not be achievable in any given operational scenario, this simplifying assumption must not be made here.

To begin, it is important to note that the estimation of N_S/t_S in Eq. 2.3.1 was obtained from two separate neutron counting measurements, and care must be taken to treat them as such. Assuming that each of the two measurements was taken over a long enough period of time to obtain a relatively large number of neutron counts (≥ 30 counts is generally acceptable for most common applications), we can assume that the count measurements N_T and N_B are approximately Gaussian distributed with means $\mu_{N_T} = N_T$ and $\mu_{N_B} = N_B$, and standard deviations $\sigma_{N_T} = \sqrt{N_T}$ and $\sigma_{N_B} = \sqrt{N_B}$. Under this assumption, the error propagation formula may be applied to our estimation:

$$\sigma_u^2 = \left(\frac{\partial u}{\partial x}\right)^2 \sigma_x^2 + \left(\frac{\partial u}{\partial y}\right)^2 \sigma_y^2 + \left(\frac{\partial u}{\partial z}\right)^2 \sigma_z^2 + \dots \quad (2.3.3)$$

where x, y, z, \dots are measured counts or related variables with known standard deviations $\sigma_x, \sigma_y, \sigma_z, \dots$ respectively, and $u = u(x, y, z, \dots)$ is any derived quantity that is a function of these count measurements/variables. Note: the error propagation formula, Eq. 2.3.3, is the foundational principle from which the desired quantity is derived in this section, and it is similarly applied to obtain additional measures of statistical significance that will be discussed, but not detailed, in later sections. Thus, the intent of this current section is twofold: (1) to derive the time-dependent certainty of source neutron detection above background, a metric that is vital to a wide variety practical applications, and (2) to provide an example of how the error propagation formula can be applied to determine the statistical certainty of any derived quantity that is a function of Gaussian- (or Poisson-) random variates, such as radiation count measurements.

For proper treatment of the problem at hand, we must now consider two possible cases: (1) a neutron count measurement, N_T , is taken for some time, $t_T \neq t_B$, with no

neutron source present, but in the presence of ambient background radiation/instrument noise, and (2) a neutron count measurement, N_T , is taken for some time, $t_T \neq t_B$, *with a neutron source present plus ambient background radiation/instrument noise.*

Case (1) A neutron count measurement, N_T , is taken for a time, $t_T \neq t_B$, with no neutron source present, but in the presence of ambient background radiation/instrument noise

Since there is no source present in this case, $N_T/t_T = N_B/t_B$ and $N_S/t_S = 0$. Since $t_T \neq t_B$, let $t_T = n \cdot t_B$ ($n \in \mathbb{R}$). Then $N_T = n \cdot N_B$. Recall that we are under the assumption that our measurement N_T is Gaussian distributed with mean $\mu_{N_T} = N_T$ and standard deviation $\sigma_{N_T} = \sqrt{N_T}$. So in this case, N_T is Gaussian distributed with mean $\mu_{N_T} = n \cdot N_B$ and standard deviation $\sigma_{N_T} = \sqrt{n \cdot N_B}$. Eq. 2.3.1 now becomes

$$\frac{N_S}{t_S} = \frac{N_T}{t_T} - \frac{N_B}{t_B} = \frac{n \cdot N_B}{n \cdot t_B} - \frac{N_B}{t_B} = 0. \quad (2.3.4)$$

So the estimated count rate due to the neutron source alone, N_S/t_S , has a mean $\mu_{N_S/t_S} = 0$, but the error propagation formula, Eq. 2.3.3, must be applied to determine its standard deviation σ_{N_S/t_S} . Since the instruments under consideration in this work can measure time with an extremely small uncertainty (with onboard CPUs), any time measurement can be assumed constant when considering the propagation of measurement error (i.e. it is assumed that there is no error in the instrument's time measurements). Furthermore, since both count measurements, N_T and N_B , are Gaussian distributed, and the set of all Gaussian distributions $\{G\}$ is closed under linear transformations, N_T/t_T and N_B/t_B must also be Gaussian distributed. Formally:

$$\text{Since } N \in \{G\} \implies a \cdot N + b \in \{G\} \quad \forall a, b \in \mathbb{R},$$

$$N_T, N_B \in \{G\} \text{ and } \frac{1}{t_T}, \frac{1}{t_B} \in \mathbb{R} \Rightarrow \frac{N_T}{t_T}, \frac{N_B}{t_B} \in \{G\}.$$

Since we know that N_T/t_T and N_B/t_B are Gaussian distributed, Eq. (2.3.3) may now be applied to these count rates to obtain their standard deviations as follows.

Without loss of generality,

let $u(N) = a \cdot N$, where $N \in \{G\}$ and $a \in \mathbb{R}$.

Then application of Eq. 2.3.3 yields $\sigma_{a \cdot N}^2 = \left(\frac{\partial}{\partial N} (a \cdot N) \right)^2 \sigma_N^2$.

$$\Rightarrow \sigma_{a \cdot N}^2 = (a)^2 \cdot (\sqrt{N})^2 = a^2 \cdot N$$

$$\Rightarrow \sigma_{a \cdot N} = a \cdot \sqrt{N} \quad (2.3.5)$$

$$\therefore \sigma_{N_T/t_T} = \frac{\sqrt{N_T}}{t_T} = \frac{\sqrt{n \cdot N_B}}{n \cdot t_B} \text{ and } \sigma_{N_B/t_B} = \frac{\sqrt{N_B}}{t_B}. \quad (2.3.6)$$

Since N_T/t_T and N_B/t_B are Gaussian distributed, and the set of all Gaussian distributions $\{G\}$ is closed under linear combinations, N_S/t_S must also be Gaussian distributed. Formally:

Since $N, M \in \{G\} \Rightarrow a \cdot N + b \cdot M \in \{G\} \quad \forall a, b \in \mathbb{R}$,

$$\frac{N_B}{t_B}, \frac{N_T}{t_T} \in \{G\} \text{ and } 1, -1 \in \mathbb{R} \Rightarrow \frac{N_T}{t_T} - \frac{N_B}{t_B} = \frac{N_S}{t_S} \in \{G\}.$$

Now that we know that N_S/t_S is Gaussian distributed, and σ_{N_T/t_T} and σ_{N_B/t_B} are known, we can apply the error propagation formula a second time to determine the standard deviation of our calculated neutron source count rate, N_S/t_S .

Now let $u\left(\frac{N_T}{t_T}, \frac{N_B}{t_B}\right) = \frac{N_T}{t_T} - \frac{N_B}{t_B} = \frac{N_S}{t_S}$. Then application of Eq. 2.3.3 yields

$$\sigma_{N_S/t_S}^2 = \left(\frac{\partial}{\partial(N_T/t_T)} \left(\frac{N_T}{t_T} - \frac{N_B}{t_B} \right) \right)^2 \sigma_{N_T/t_T}^2 + \left(\frac{\partial}{\partial(N_B/t_B)} \left(\frac{N_T}{t_T} - \frac{N_B}{t_B} \right) \right)^2 \sigma_{N_B/t_B}^2.$$

$$\begin{aligned}
\Rightarrow \sigma_{N_S/t_S}^2 &= (1)^2 \cdot \left(\frac{\sqrt{n \cdot N_B}}{n \cdot t_B} \right)^2 + (-1)^2 \cdot \left(\frac{\sqrt{N_B}}{t_B} \right)^2 \\
\Rightarrow \sigma_{N_S/t_S}^2 &= \frac{n \cdot N_B}{n^2 \cdot t_B^2} + \frac{N_B}{t_B^2} = \frac{N_B}{n \cdot t_B^2} + \frac{N_B}{t_B^2} = \frac{N_B}{n \cdot t_B \cdot t_B} + \frac{N_B}{t_B^2} = \frac{N_B}{t_T \cdot t_B} + \frac{N_B}{t_B^2} \\
\therefore \sigma_{N_S/t_S} &= \sqrt{\frac{N_B}{t_T \cdot t_B} + \frac{N_B}{t_B^2}}
\end{aligned} \tag{2.3.7}$$

We now have a full description of N_S/t_S when there is no neutron source present. We know that N_S/t_S , as calculated in Eq. 2.3.4, is Gaussian distributed with mean $\mu_{N_S/t_S} = 0$ and standard deviation as shown in Eq. 2.3.7. Since there is no neutron source present during this measurement, any positive measurement of N_S/t_S would be a false positive detection, (labeled *FP* in Fig. 2.3.1). Also, any negative measurement of N_S/t_S would obviously mean that there is no source present, so only positive deviations from the mean should be considered here (i.e. one-tailed probabilities are appropriate for this analysis). It is often desirable in such circumstances to set a critical limit (L_C in Fig. 2.3.1),

$$L_C = z_{FP} \sigma_{N_S/t_S} = z_{FP} \cdot \sqrt{\frac{N_B}{t_T \cdot t_B} + \frac{N_B}{t_B^2}}, \tag{2.3.8}$$

by choosing a value for z_{FP} such that the probability of a false positive is very small (e.g. $z_{FP} = 1.64 \rightarrow$ one tailed $P(FP) = (100\% - 90\%)/2 = 5\%$). However, for the purpose of this derivation, z_{FP} will remain an unassigned variable for further analysis in Case 2.

Case (2) A neutron count measurement, N_T , is taken for a time, $t_T \neq t_B$, with a neutron source present plus ambient background radiation/instrument noise

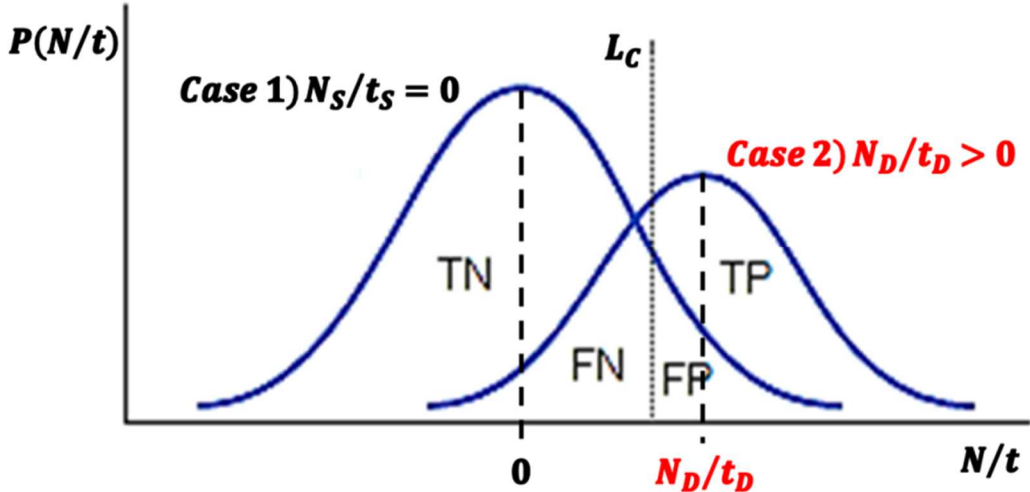


Figure 2.3.1: Conceptual illustration of Gaussian probability distributions for Case 1 (left) and Case 2 (right). TN = true negative, TP = true positive, FN = false negative, FP = false positive.

Since this is a different measurement of the count rate from the neutron source alone, we will make the notation change $N_S/t_S \rightarrow N_D/t_D$. And since there is a neutron source present in this case, we assume that $N_T/t_T > N_B/t_B$ and $N_D/t_D > 0$ (Fig. 2.3.1), and Eq. 2.3.1 becomes

$$\frac{N_D}{t_D} = \frac{N_T}{t_T} - \frac{N_B}{t_B} > 0. \quad (2.3.9)$$

Again, we wish to determine the standard deviation of this estimated count rate due to the neutron source alone, N_D/t_D , and we will proceed in the same manner as Case 1. By Eq. 2.3.5, we know that the standard deviations of N_T/t_T and N_B/t_B must be, respectively,

$$\sigma_{N_T/t_T} = \frac{\sqrt{N_T}}{t_T} \text{ and } \sigma_{N_B/t_B} = \frac{\sqrt{N_B}}{t_B}. \quad (2.3.10)$$

Since σ_{N_T/t_T} and σ_{N_B/t_B} are now known, we may once again apply the error propagation formula, Eq. 2.3.3, to determine the standard deviation of our calculated neutron source count rate, N_D/t_D .

Now let $u\left(\frac{N_T}{t_T}, \frac{N_B}{t_B}\right) = \frac{N_T}{t_T} - \frac{N_B}{t_B} = \frac{N_D}{t_D}$. Then application of Eq. 2.3.3 yields

$$\begin{aligned} \sigma_{N_D/t_D}^2 &= \left(\frac{\partial}{\partial(N_T/t_T)} \left(\frac{N_T}{t_T} - \frac{N_B}{t_B} \right) \right)^2 \sigma_{N_T/t_T}^2 + \left(\frac{\partial}{\partial(N_B/t_B)} \left(\frac{N_T}{t_T} - \frac{N_B}{t_B} \right) \right)^2 \sigma_{N_B/t_B}^2. \\ \Rightarrow \sigma_{N_D/t_D}^2 &= (1)^2 \cdot \left(\frac{\sqrt{N_T}}{t_T} \right)^2 + (-1)^2 \cdot \left(\frac{\sqrt{N_B}}{t_B} \right)^2 \\ \Rightarrow \sigma_{N_D/t_D}^2 &= \frac{N_T}{t_T^2} + \frac{N_B}{t_B^2} \\ \therefore \sigma_{N_D/t_D} &= \sqrt{\frac{N_T}{t_T^2} + \frac{N_B}{t_B^2}} \end{aligned} \quad (2.3.11)$$

We now have a full description of N_S/t_S when there is *no* neutron source present and N_D/t_D when there *is* a neutron source present. We know that N_S/t_S , as calculated in Eq. 2.3.4, is Gaussian distributed with mean $\mu_{N_S/t_S} = 0$ and standard deviation as shown in Eq. 2.3.7, and N_D/t_D , as calculated in Eq. 2.3.9, is Gaussian distributed with mean $\mu_{N_D/t_D} = N_D/t_D$ and standard deviation as shown in Eq. 2.3.11. Since there is a neutron source present during the Case 2 measurement, any neutron count originating from the source that do not contribute to our estimate of N_D/t_D would be false negative detection, FN (Fig. 2.1). From Fig. 2.1, notice that N_D/t_D could be described, relative to L_C , as

$$\frac{N_D}{t_D} = L_C + z_{FN}\sigma_{N_D/t_D} = z_{FP}\sigma_{N_S/t_S} + z_{FN}\sigma_{N_D/t_D}. \quad (2.3.12)$$

Since both false positives and false negatives contribute to the net uncertainty in our estimated count rate from the neutron source, we will assign each error type equal importance by setting $z_{FP} = z_{FN} \equiv z$, such that Eq. 2.3.12 becomes

$$\frac{N_D}{t_D} = z \cdot (\sigma_{N_S/t_S} + \sigma_{N_D/t_D}). \quad (2.3.13)$$

Solving Eq. 2.3.13 for z gives us

$$z = \frac{\frac{N_D}{t_D}}{\sigma_{N_S/t_S} + \sigma_{N_D/t_D}}.$$

Substituting the results of Eq. 2.3.9 for N_D/t_D , Eq. 2.3.7 for σ_{N_S/t_S} , and Eq. 2.3.11 for σ_{N_D/t_D} yields

$$z = \frac{\frac{N_T}{t_T} - \frac{N_B}{t_B}}{\sqrt{\frac{N_B}{t_T \cdot t_B} + \frac{N_B}{t_B^2}} + \sqrt{\frac{N_T}{t_T^2} + \frac{N_B}{t_B^2}}}.$$
 (2.3.14)

This is now an expression for z that can be calculated by the onboard CPU in a neutron detection instrument in real time, using an updated N_T and t_T every user-defined time step (typically, a 1-second time step is used) and the previously measured N_B and t_B . This z value can then be used to calculate the time-dependent certainty in N_D/t_D (updated and displayed to the user once every user-defined time step) as

$$\text{Certainty in } \frac{N_D}{t_D} = \frac{1}{2} + \frac{1}{2} \cdot \text{erf}\left(\frac{z}{\sqrt{2}}\right),$$
 (2.3.15)

where $\text{erf}(\cdot)$ is the error function. This measure of statistical certainty, which was the primary goal of this derivation, can now be interpreted as the certainty in the neutron count rate due to a neutron source of interest above ambient background and instrument noise.

CHAPTER 3

DESIGN, OPTIMIZATION, AND TESTING OF FOUR MODERATING-TYPE NEUTRON SPECTROMETERS

3.1 Introduction

Portable instruments that can detect and identify neutron sources by high intrinsic efficiency and energy-sensitive measurement of free neutrons, ranging from thermal energies (~ 25 meV) to top end of the evaporation spectrum (~ 20 MeV), are important to applications in non-proliferation and health physics. For non-proliferation applications, the goal is a sensitivity and spectroscopic resolution that will allow for unknown source detection and identification from neutrons alone as a complement to portable gamma-ray spectroscopic instruments; detection over the large energy range is important for sources in unknown shielding (i.e., moderating/absorbing) configurations. In health physics applications, the neutron dose equivalent rises and falls more than two-orders of magnitude over the thermal to 14 MeV energy range, presenting substantial dosimetry challenges. In commercially available rem meters [8], the average dose equivalent error is significant due to poor energy sensitivity in the upper end of this large range. To address the challenges inherent to these applications, this section presents and compares the empirical and computational design and results of a new class of real-time human-portable neutron spectrometer, building from the foundation established by Bonner [9], and enabled by the high thermal neutron detection efficiency density (thermal neutron detection efficiency per unit active volume) and spatial resolution of semiconductor-based neutron detectors [10].

3.2 Instrument Design and Optimization

3.2.1 Background

The instrument geometries, detector-moderator configurations, analysis methods, and results described here are a synthesis of, and improvement on, the multi-sphere- and long-counter-based moderating-type neutron spectrometers [9, 11]. The major deficiencies in the multi-sphere spectrometers are: (a) the inability to measure neutron intensity with each sphere radius simultaneously, (b) the poor spatial resolution of detected thermalized neutrons, (c) the very low intrinsic neutron detection efficiency, and (d) the unportable mass of the near-largest- to largest-radius moderating sphere used to measure neutron intensity at the top end of the fast neutron energy range (i.e., $\geq 30\text{-cm}$ radius). In the long counter design, neutron intensity is measured axially in a cylindrical geometry, replacing the radial dependence of the measured neutron intensity in the spherical geometry. Although the cylindrical geometry prevents equal sensitivity over 4π , an instrument with a portable mass that can still provide enough low-Z cross section to thermalize a 14-MeV neutron is gained. The downfall of the single position-sensitive sensor in the long counter design is its low intrinsic efficiency and crude energy resolution, even in advanced designs [12, 13]. While adding axial sensors radially can theoretically improve the intrinsic efficiency as well as the energy and spatial resolution of a long-counter, a large fraction of the moderating medium must be displaced, increasing both the volume and overall instrument mass [14]. What is needed is a different type of thermal neutron sensor that yields minimal displacement of the moderating medium, while simultaneously providing volumetric resolution of the average neutron thermalization along three coordinate axes within the moderator-detector assembly (see Fig. 3.2.1). Three-dimensional resolve is important in improving the source

identification accuracy (and in increasing the number of detector responses one can unfold against for absolute neutron energy determination), while also providing the ability to achieve directional resolution (discussed in detail in chapters 4 and 5). The efficacy of the analysis techniques described in this chapter is based on the uniqueness (between various neutron source types/radioisotopes) of the measured neutron detection intensity as a function of three-dimensional position in the moderating medium (*vide infra*). Based on mean free path in common moderating media, the volumetric resolution for thermal and epithermal incident and scattered neutrons should be no larger than $\sim 1 \text{ cm}^3$, which forms the most restrictive neutron sensor design constraint. While state-of-the-art gaseous, doped-plastic, doped-glass, and doped-liquid thermal neutron detectors may be capable of meeting a small volume, their thermal neutron detection efficiency density is at least five times lower than advanced semiconductor-based detectors, especially when the readout electronics are also considered [1]. It is for these reasons, in addition to technological maturity, gamma-ray insensitivity, and availability, that the microstructured neutron detectors (MSNDs) [10] have been chosen for use in this work.

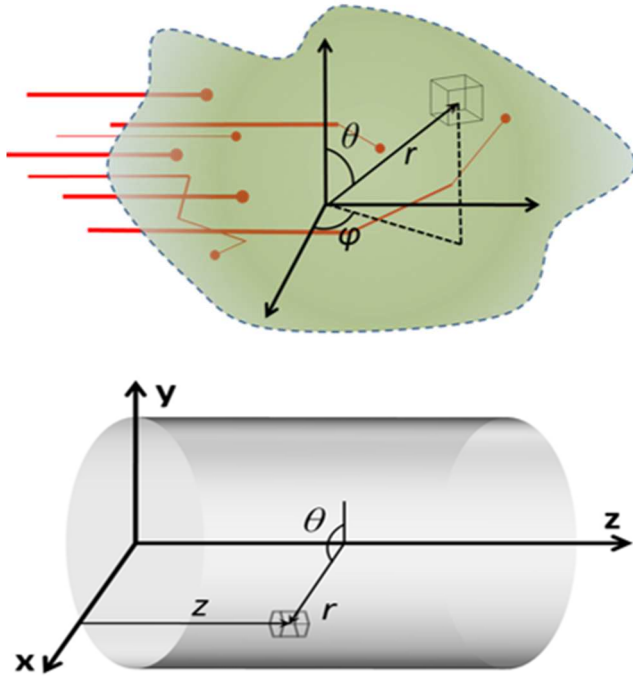


Figure 3.2.1. Conceptual illustrations of moderating media, showing (TOP) an illustration of free neutrons thermalizing in a moderating medium, emphasizing the concept of volumetric resolution to better than $\sim 1 \text{ cm}^3$ along three coordinate axes, and (BOTTOM) an illustration of a cylindrical moderator, and cylindrical coordinate system.

3.2.2 Theory of Operation

Passively searching for and/or identifying neutron sources in non-proliferation applications requires the collection and analysis of one or more free neutron properties with high efficiency and energy sensitivity. To measure the neutron dose equivalent for health physics applications, identify one or more neutron sources, or determine the relative direction of a neutron source, analysis of the free neutron signature is one of the most powerful means. A high intrinsic and absolute neutron detection efficiency is important given the limited time available for measurement in these operational environments and energy sensitivity is crucial to neutron source identification and measuring the neutron dose equivalent [1, 15]. Only moderating-type neutron spectrometers are capable of enabling resolution of free neutron

kinetic energy over the 10^{-8} to 10^1 MeV energy range while maintaining hand-held portability [1, 14, 15].

Although spectral deconvolution (unfolding) can be used to determine absolute neutron energy, relative or proportional signatures can provide as much or more information by template matching (measuring the degree of correlation of) the calibrated intensity profile to an absolute incident neutron energy signature (i.e., thermalized neutron intensity as a function of physical detector position along one or more coordinate axes in a moderating medium). Further, analysis of proportional signatures does not carry the computational overhead or assumptions required in solving the classically underdetermined and ill-conditioned inverse problem [16, 17] (in chapter 6, two promising spectral deconvolution/unfolding techniques will be investigated, in light of the novel three-dimensional neutron thermalization information provided by the instruments discussed in this section). To measure quantities proportional to free neutron kinetic energy using the moderating mechanism, it is critical to design an instrument configuration that is maximally sensitive to small variations in incident spectral features. To accomplish this connection, a combination of tuned scattering and absorption materials with thermal neutron detectors is required, and is discussed in detail below.

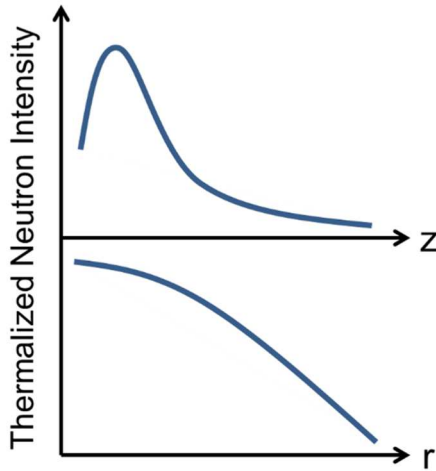


Figure 3.2.2. Heuristic illustration of the thermalized neutron intensity distribution as a function of the axial and radial position in a cylindrical moderator in cylindrical coordinates. Neutrons with a Watt energy spectrum are assumed to be incident on the front face of a cylindrical moderator ($z = 0$ is the front face) and uniformly distributed over r .

Fig. 3.2.2 is a starting point in understanding how the thermalized neutron intensity can be used as a signature of the incident neutron spectrum or the neutron source's location relative to the instrument. It is the spectral "fingerprint" (detection intensity as a function of one or more coordinate axes) uniqueness and intrinsic efficiency values, that serve as metrics for the process by which the instruments reported here are iteratively designed. Absolute neutron detection efficiency, which is determined by the area onto which the neutrons impinge, is not an essential feedback criteria of the designs considered here; rather, energy-dependent intrinsic neutron detection efficiency, that normalizes area, is used. In this work, an instrument's intrinsic neutron detection efficiency to a particular neutron source spectrum, S , (e.g., unshielded ^{252}Cf , AmBe shielded by 1 in. of HDPE, etc.) is defined as

$$\eta_{int}(S) = \frac{N_{det}(S)}{N_{inc}(S)}, \quad (3.2.1)$$

where $N_{det}(S)$ is the total number of neutrons detected by the instrument from source S and $N_{inc}(S)$ is the total number of neutrons from source S that impinge upon the instrument volume. Fig. 3.2.2 illustrates that a Maxwellian-type neutron energy spectrum will cause a reproduction of that curve shape as a function of the axial position into the moderator, and that neutron scatter and escape will cause a drop-off in intensity as a function of radius. In this simplified example, the axial and radial distributions yield a signature of the neutron source that can be compared against reference intensity distributions. The problem is then how to design the detector-moderator assembly to best resolve these signatures and/or use the captured data to generate more complex distributions for comparison using source spectra of interest to the application.

3.2.3 Detector and Moderator Design

Based on the need to detect thermalized neutrons along three-coordinate axes in $\leq 1\text{-cm}^3$ voxels in a moderating medium with axial symmetry (e.g., Fig. 3.2.1 BOTTOM), the instrument design initially converged on a 2-D array of pixelated detectors (Fig. 3.2.3 LEFT) that could be stacked axially to yield a 3-D array (Fig. 3.2.3 RIGHT). With each detector read out individually, thermalized neutron intensity can be summed for any coordinate, product of coordinates, or approximate volume (e.g., quadrants, octants) that best fits the application needs (see Fig. 3.2.4). For crude directional analysis, octant summing is useful (e.g., neutrons are incident from the forward-right-up position), and for crude source identification, summing each wafer plane and plotting the intensity vs. axial position can be useful (Fig. 3.2.2 TOP). To enable space-filling and approximate radial symmetry, a hexagonal pattern (Fig. 3.2.3 LEFT) was chosen for the first instrument design and build; later instruments used a square detector shape and square 2-D assembly to reduce the build

complexity. In all, four instruments of varying mass and detector arrangement were designed, built, tested and will be discussed and compared.

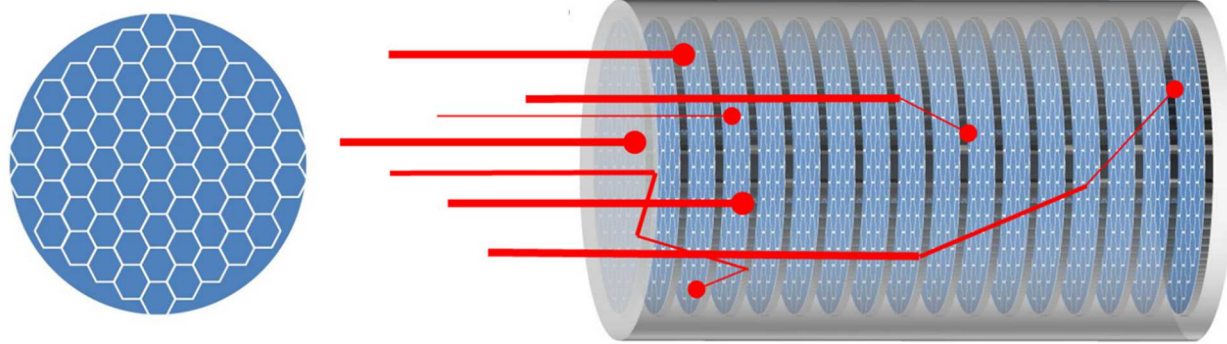


Figure 3.2.3. LEFT – illustration of a MSND board with hexagonal patterning to form a 2-D detector array with approximate radial symmetry. RIGHT – an axial stack of 2-D detector arrays, separated and embedded by neutron moderator.

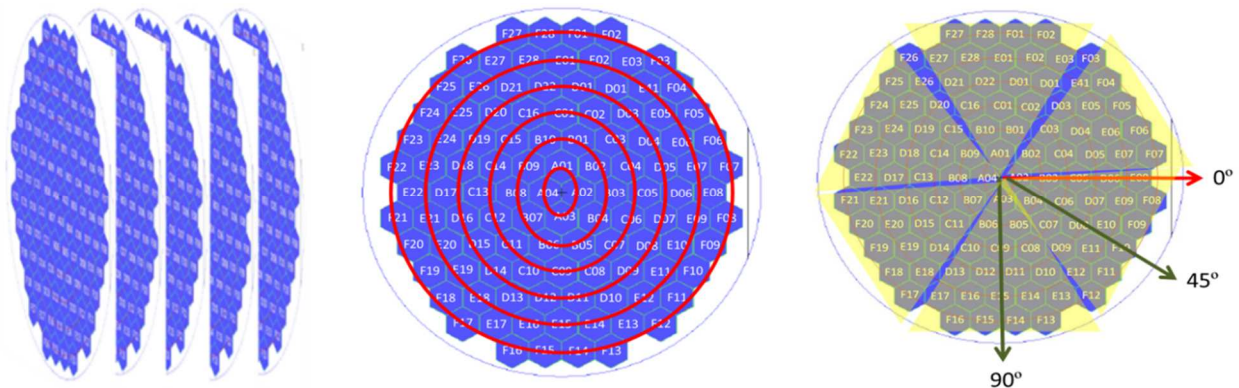


Figure 3.2.4. Example illustrations of detector plane intensity summations vs. axial position (LEFT), vs. radius (MIDDLE), and vs. angular sector (RIGHT).

In addition to the individual detector shape, the 2-D detector array design requires finding the optimal thermal neutron detection efficiency, active area, summed area, and summed shape(s). However, the overall instrument optimization process is ultimately

determined based on the intimate relationship between detector and moderator, in reference to the source spectra of interest to the application and method of operation. Therefore, the design of the detectors should be made in the context of the overall instrument, in light of its concept-of-operations and the expected spectral distribution, including environmental scattering factors.

For simplicity, the source spectra used to optimize the instrument designs described here are that of bare ^{252}Cf [18] and bare AmBe [18]. Although the use of other sources, including moderated variants thereof, would follow the same procedure, bare ^{252}Cf and AmBe were chosen due to the similarities of their induced responses in moderating-type neutron spectrometers. Operationally, the instrument can be carried or set down for measurement. Neutrons can be incident from any direction when in source search mode; however, most of the source neutrons must enter the front cylinder face to optimally perform the identification analysis while in spectral mode. It is not absolutely required that the front face represent the reference datum point, since a signature can be developed for any incident angle relative to the long-axis of a cylindrical moderator-detector assembly; the downside for non-longitudinal incident neutrons is a lower net identification certainty, the discussion of which is outside the scope of this work. It is in this case, however, that a spherical geometry could be the best theoretical design due to 3-dimensional symmetry.

The design work discussed here is based on the simultaneous optimization of: (1) the intrinsic efficiency to spontaneous fission neutron sources (spontaneous fission being the neutron source type of interest to most applications), and (2) the ability to spectroscopically differentiate spontaneous fission sources from (α , n) and/or spallation neutron sources (representing the ability to discern potential threats from non-threats and/or ambient

background radiation), and moderated/shielded variants thereof. Using (2) as a measure of the signature sensitivity, the efficacy of varying analysis techniques for each moderator-detector design type can be compared systematically. Source differentiation is an operational feedback tool analogous to energy resolution; when the spectral fingerprint between two sources or source configurations is most different, the energy resolution (in the most relevant energy range) or equivalent quantity should be optimal.

To perform the signature (or energy) sensitivity analysis for proposed instrument designs, a one-dimensional cross correlation analysis is used to provide an operational optimization metric (extensions of, and potential improvements to, this one-dimensional analysis will be discussed in chapters 4 and 5). In this case, the Pearson product-moment cross-correlation coefficient [19] is used to yield a “score” between the axial intensity distributions created from a simulation (MCNP) of bare ^{252}Cf neutrons and a simulation of bare AmBe neutrons incident on the front face of a proposed instrument model. The Pearson correlation, r , (Eq. 3.2.2) results in a value in the range [-1, 1] which is a measure of linear correlation (similarity) between the two spectrometer responses, where $r = 1$ indicates a total positive correlation (the signatures are exactly the same), $r = 0$ indicates no correlation (the signatures are entirely different), and $r = -1$ indicates a total negative correlation (the signatures are exactly opposite). Therefore, the energy sensitivity of a proposed instrument design is optimal when this correlation is minimized (i.e., when the two signatures are least similar and can be more easily differentiated).

$$r_{Cf,AmBe}(z) = \frac{1}{n} \cdot \sum_{i=1}^n \frac{N_{Cf}(z_i) - \overline{N_{Cf}(z)}}{\sigma_{N_{Cf}(z)}} \cdot \frac{N_{AmBe}(z_i) - \overline{N_{AmBe}(z)}}{\sigma_{N_{AmBe}(z)}}, \quad (3.2.2)$$

where $N_{Cf}(z) = \begin{bmatrix} N_{Cf}(z_1) \\ \vdots \\ N_{Cf}(z_n) \end{bmatrix}$ is the ^{252}Cf response, $N_{AmBe}(z) = \begin{bmatrix} N_{AmBe}(z_1) \\ \vdots \\ N_{AmBe}(z_n) \end{bmatrix}$ is the AmBe

response, $\overline{N(z)}$ is the average of $N(z)$, and $\sigma_{N(z)}$ is the standard deviation of $N(z)$.

In order to optimize between the maximum intrinsic efficiency and minimum Pearson correlation metrics for the second and third instrument designs, numerous simulation series were conducted using the Monte Carlo N-Particle transport code (MCNP5). For each of the simulation series described here, although most other available parameters (e.g., moderator thickness, radius, and material) are varied within the design constraints (size, weight, cost, etc.), the MCNP representation of the detector boards remains unchanged and eight detector boards were used in each simulation (unless otherwise stated). Each of the eight detector boards consists of a 4×4 square array of 2-cm \times 2-cm MSNDs. Each detector array is covered in front with an aluminum shield and mounted on a 10.16-cm \times 10.16-cm FR-4 (E-Glass) printed circuit board (PCB) with all circuit components mounted to the side opposite the detector array (see Fig. 3.2.5).

The MSNDs are comprised of Si diodes, etched to form trenches and backfilled with ^6LiF powder; they yield an empirical thermal neutron detection efficiency of $\eta_{th} \approx 22\%$. The MSND detection mechanism has been described in detail previously [20]. To reduce computation time for the MCNP simulations described in this work, it was necessary to simplify the geometrical representation of the MSNDs. Each MSND was modeled as one 2-cm \times 2-cm \times 0.0525-cm rectangular prism (true MSND outer dimensions) containing both ^6LiF and Si, and the appropriate ratio of ^6LiF to Si was determined by matching the simulated and empirically measured thermal neutron detection efficiencies. To accomplish this, several preliminary simulations were run in which thermal neutrons (approximated by a Maxwellian

distribution with a temperature parameter of 0.0257 eV), emitted uniformly from a planar source, were directed toward the MSND model. Since the neutron detection transduction mechanism of the MSNDs depends upon the reaction ${}^6_3Li + {}^1_0n \rightarrow {}^4_2\alpha + {}^3_1t$, the number of (n, t) reactions (i.e., neutron capture reactions in which tritons, 3H nuclei, are produced) occurring in the MSND model were tallied (counted) in each simulation, and the thermal neutron detection efficiency, η_{th} , was calculated by

$$\eta_{th} = \frac{N_{(n,t)}}{N_{th}}, \quad (3.2.3)$$

where $N_{(n,t)}$ is the total number of (n, t) reactions occurring in the MSND model and N_{th} is the total number of thermal neutrons that impinge upon the MSND model. Keeping the percentages of 6Li and F equal, the ratio of 6LiF to Si was adjusted in each simulation until 22% thermal neutron detection efficiency was achieved.

3.2.3.1 Moderator Geometry and Dimension Optimization

Although one could consider many other geometries, only the cylindrical and rectangular prism moderator geometries were designed and built (Fig. 3.2.5) using high-density polyethylene (HDPE). A spherical design offers the most flexibility and can intrinsically mitigate the effect of environment-scattered or multi-directional neutrons, and conical designs may show merit, but their manufacturing complexity and/or required thermalization mass is too high. Fig. 3.2.6 shows the simulated intrinsic neutron detection efficiency and spectral sensitivity for both the cylindrical and rectangular prism designs as a function of moderator radius, R, and thickness, T, between each of the eight detector boards. In the case of the rectangular prism, the radius is defined, as shown in Fig. 3.2.5, by the distance from the center to the corner of the moderator's front face.

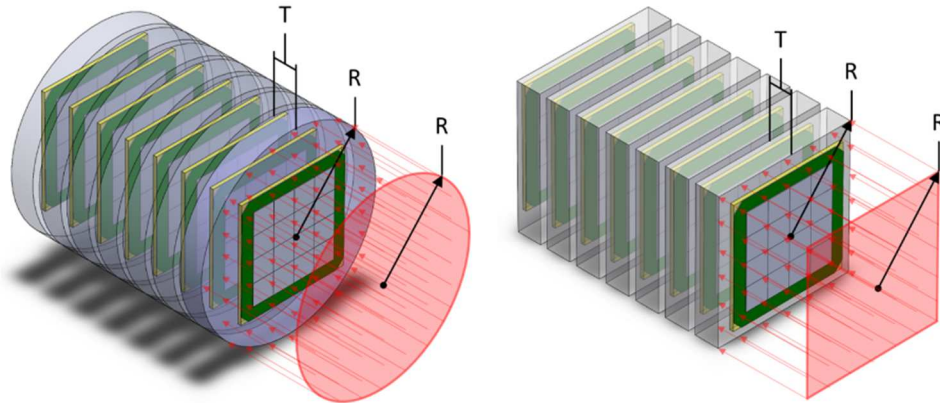


Figure 3.2.5. Renderings of the cylindrical (LEFT) and rectangular prism (RIGHT) moderator geometries with eight 4×4 arrays of 4-cm^2 detectors, and the thickness and radius of the moderator slabs indicated. The red plane represents the neutron source used in the simulations to produce the results in Fig. 3.2.6.

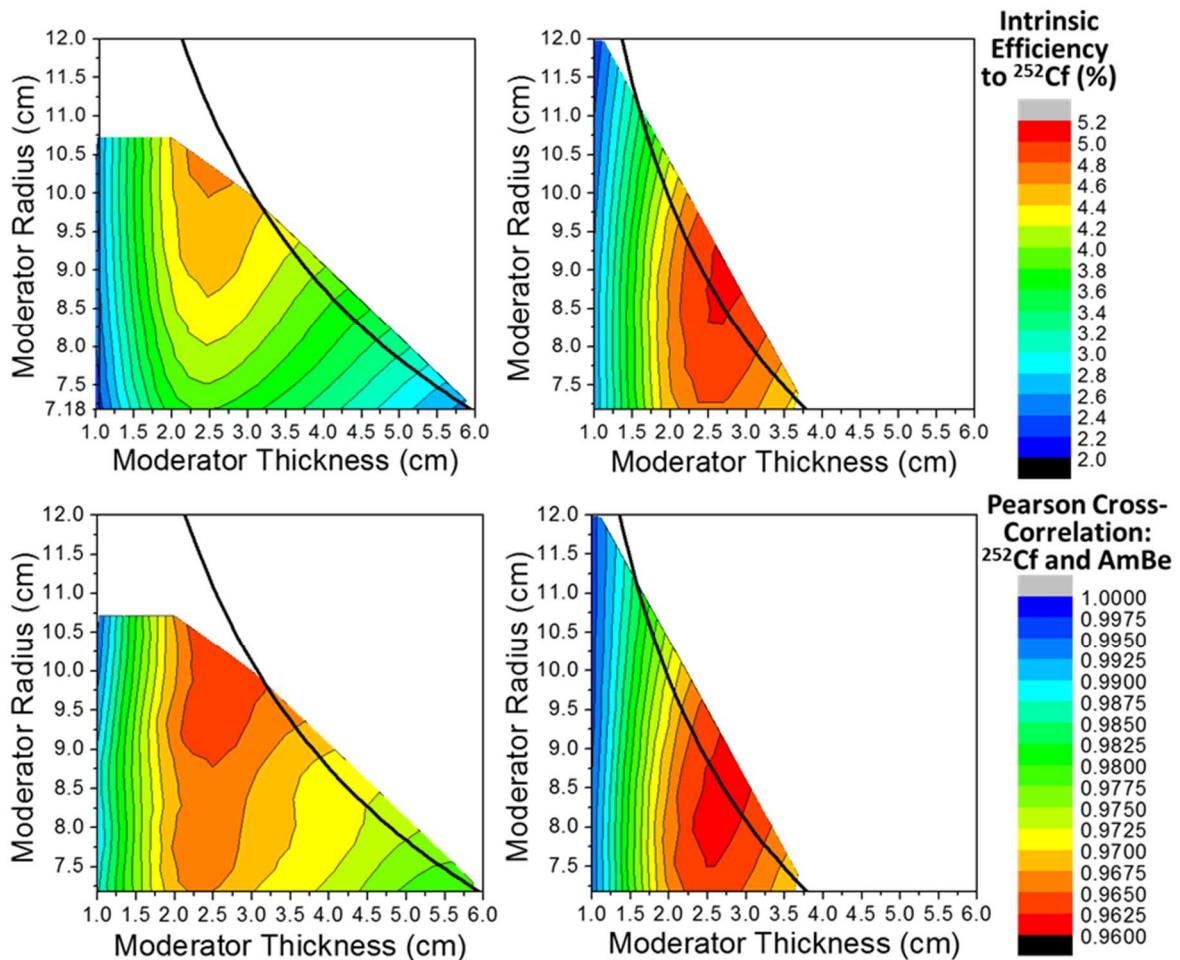


Figure 3.2.6. Results of the simulated intrinsic neutron detection efficiency to bare ^{252}Cf for the rectangular prism (TOP LEFT) and cylindrical (TOP RIGHT) geometries, with a

common color scale (red indicating maximum intrinsic efficiency). And results of the simulated spectral sensitivity metric (^{252}Cf -AmBe spectral difference) for the rectangular prism (BOTTOM LEFT) and cylindrical (BOTTOM RIGHT) geometries, with a common color scale (red indicating minimum Pearson correlation). The thick black line in each plot is an iso-mass curve, indicating the radius and thickness combinations that yield a total HDPE moderator + detector board weight of 10 lbs.

The instrument optimization and analysis methods used to create Fig. 3.2.6 serve as a primary theoretical baseline and operational feedback tool for the instrument designs described in this section. As stated previously, the 4×4 array detector boards are considered here to be a fixed design parameter for investigating the effects of moderator geometries and dimensions on the aforementioned operational performance metrics for detection efficiency and source identification (energy sensitivity). The limit of eight detector boards per instrument is estimated based on conservatively-projected cost limitations, forming another fixed design parameter. Holding these two parameters constant, the physical moderator dimensions described in Fig. 3.2.5 are varied under an active weight constraint of 10 lbs., and simulated for a coarse grid of discrete radius and thickness combinations (representing single (x, y) points in each plot in Fig. 3.2.6). Intrinsic neutron detection efficiencies to bare ^{252}Cf and Pearson correlations between bare ^{252}Cf and bare AmBe instrument responses are then calculated for each discrete radius and thickness combination and plotted in a third (metric) dimension. A three-dimensional interpolation is then applied to the data, indicating regions of the tunable parameter space that may warrant further exploration. These promising regions are then broken down into finer grids of discrete points for subsequent simulation, and the process is repeated until no practically significant improvement can be made toward the desired optimization metric. This optimization technique is explored further and utilized to a fuller extent in following sections.

In analysis of Fig. 3.2.6, the most immediately apparent result is that, for an active instrument weight of less than 10 lbs., the cylindrical moderator geometry outperforms the rectangular prism geometry for both operational metrics. Since portability is of primary concern to both nuclear nonproliferation and health physics applications, the cylindrical geometry is clearly more optimal for meeting the application needs under the simplifying assumptions made here. It is also significant (and serendipitous) to note that, for both geometry types, the optimal moderator thickness is roughly the same for both performance metrics, indicating that simultaneous optimization may be possible without significant tradeoffs to either metric.

3.2.3.2 Detector Efficiency Optimization

Commercially available microstructured semiconductor neutron detectors are capable of thermal neutron detection efficiencies in excess of 44% [21, 22]. To explore the effect of increasing thermal neutron detector efficiency of the constituent MSNDs on the intrinsic neutron detection efficiency of a cylindrical spectrometer design, a series of simulations was conducted in which neutrons from a bare ^{252}Cf source were incident upon the front circular face of a moderator-detector assembly with thirty 525- μm thick \times 5-in. diameter cylindrical detector boards, separated axially by twenty-nine 1-cm thick \times 5-in. diameter HDPE cylinders (initial **5C** design, Fig. 3.2.3, discussed further in Section 3.3). The thermal neutron detection efficiencies of the constituent MSNDs were varied in each simulation from 3% to 51%. Fig. 3.2.7 shows that as the thermal detection efficiencies of the MSNDs increases above 22% there is a diminishing return to the instrument intrinsic efficiency to bare ^{252}Cf .

Quantitatively, the intrinsic neutron detection efficiency increases by more than a factor of 4 (from 0.669% to 2.85%) when using a 22% detector over a 4% detector, while

only increasing by a factor of 1.68 (from 2.85% to 4.79%) when using a 44% detector over a 22% detector. Due to this diminishing return in intrinsic efficiency, the instruments designed in this work were held to 22% thermal neutron detection efficiency MSNDs.

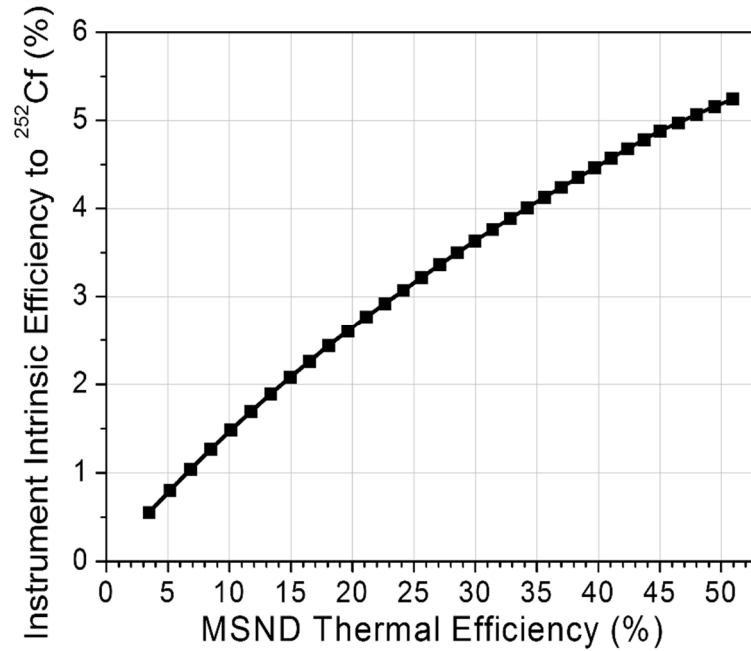


Figure 3.2.7. Simulated instrument intrinsic detection efficiency to ^{252}Cf as a function of MSND thermal neutron detection efficiency.

3.2.3.3 Moderator Radius to Detector Radius Ratio Optimization

As shown in Fig. 3.2.2 (BOTTOM), in the case that the detector plane is the same radius or area as the axially symmetric moderator, the intensity of neutron counts (from normal incident on the front cylinder face) fall off as a function of radius. If a neutron reflecting material is placed outside of the outer detector radius, some neutrons can be re-scattered or reflected inward and the intrinsic neutron detection efficiency can increase. Fig. 3.2.8 shows how an instrument's intrinsic efficiency to bare ^{252}Cf changes as a function of outer detector radius for various moderator-to-detector radius ratios. In these simulations,

high density polyethylene is used as both the central moderator and reflector. In all simulations with an outer detector radius less than 5 cm, the intrinsic efficiency increases as the moderator-to-detector radius ratio increases. Above a 5-cm outer detector radius the intrinsic efficiency increase slows and reaches a maximum of 36% at a 10-cm outer detector radius for the 1.125 and 1.25 moderator-to-detector radius ratios. The falloff above a 10-cm outer detector radius for all moderator-to-detector ratios is due to the moderator radius being larger than the average mean free path of the bare ^{252}Cf neutrons in high density polyethylene. This leads to increased neutron absorption by hydrogen nuclei in the moderator volume (${}_0^1n + {}_1^1H \rightarrow {}_2^2H + \gamma$ (2.223 MeV)). For a portable instrument with cylindrical symmetry and total weight of ~15-lbs., the moderator volume, at maximum, would be restricted to a 7.6-cm radius and 30-cm length. To achieve the highest intrinsic efficiency (not necessarily the highest absolute efficiency) for the cylindrical geometry (~15%) and total weight of ~15-lbs., the detector radius would not exceed 3.8-cm.

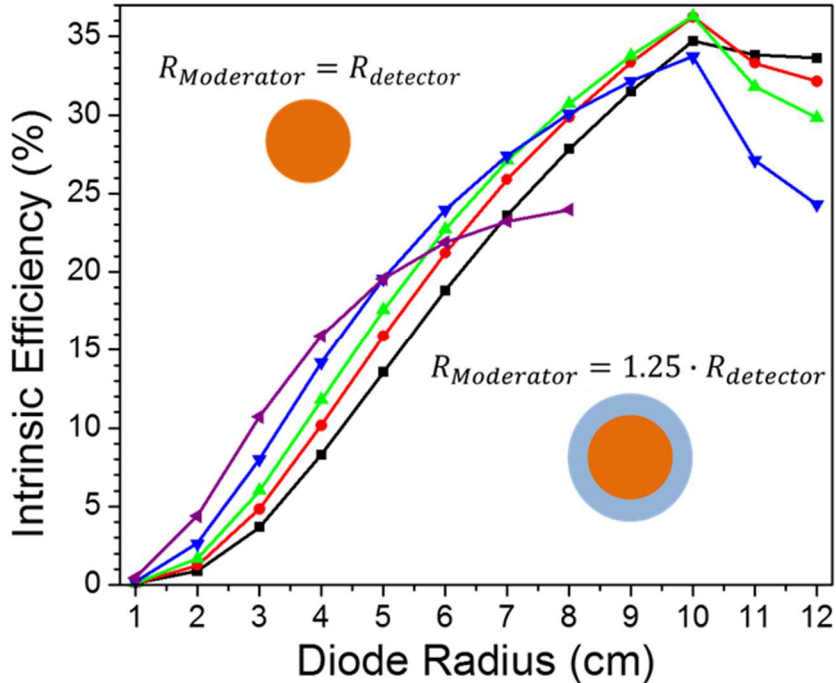


Figure 3.2.8. Intrinsic neutron detection efficiency to ^{252}Cf as a function of detector (diode) layer radius for varying detector-to-moderator radius ratios ($\blacksquare R_{\text{moderator}} = R_{\text{detector}}$, $\bullet R_{\text{moderator}} = 1.125 \cdot R_{\text{detector}}$, $\blacktriangle R_{\text{moderator}} = 1.25 \cdot R_{\text{detector}}$, $\blacktriangledown R_{\text{moderator}} = 1.5 \cdot R_{\text{detector}}$, $\blacktriangleleft R_{\text{moderator}} = 2 \cdot R_{\text{detector}}$).

3.2.3.4 Moderator Type Optimization

A major goal of this work is to design an instrument that will yield the most unique distribution of detected thermalized neutrons while also maintaining the highest possible intrinsic efficiency. Since the type of neutron moderating material used can greatly influence both of these operational characteristics, it is important to consider the role of moderators other than high density polyethylene (HDPE). HDPE is a popular neutron moderating material because it is inexpensive, readily available, mechanically strong but easily machinable, and resilient to most environmental factors. Its hydrogen concentration by volume is very high (i.e., $8.07702\text{E}+22$ Atoms H/cm 3), which is important for neutron scattering and moderation. However, could a very high hydrogen concentration also be

detrimental to thermal and lower-epithermal energy resolution, as neutrons in these energy ranges can be thermalized and detected with little traverse into the instrument detector layers? Or conversely, could a higher hydrogen concentration material, or possibly high carbon containing, help to improve the thermalized intensity distribution (i.e., signature of higher-epithermal or fast neutrons) by better physical separation of the higher energy neutrons detected?

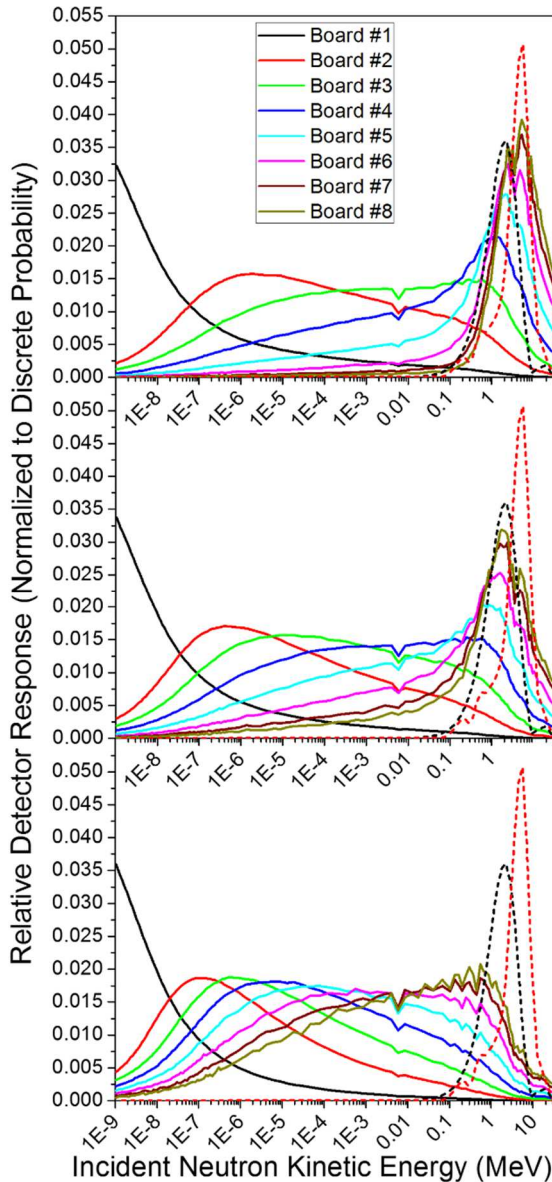


Figure 3.2.9. Normalized detector-board-summed response functions (solid lines) for instrument models with various moderator materials. All instrument models had a cylindrical moderator design with 7.62-cm radius and 3.6-cm thickness, as defined by Fig. 3.2.5, with 8 rectangular detector boards. The simulated moderator materials were HDPE (TOP), polystyrene (MIDDLE), and polysulfone (BOTTOM). In each case, the first detector board (most sensitive to the lowest energy neutrons) is represented by a solid black line and peaks leftmost, while the last detector board (most sensitive to the highest energy neutrons) is represented by a solid olive line and peaks rightmost. Normalized ^{252}Cf (dashed black line) and AmBe (dashed red line) neutron emission spectra are also included in each plot for reference.

To help answer these questions, simulations were performed using high-density polyethylene (HDPE), polystyrene, and polysulfone moderator materials, all in the same instrument configurations, in order to study the effect of varying hydrogen and carbon concentration on the overall performance of the instrument; a summary of each moderator's salient properties is shown in Table 3.2.1 . Note: although these 4 moderator materials are highlighted here for illustrative purposes, a multitude of potential materials were tested and compared in an extensive study; additional materials investigated include (but were not limited to) polypropylene, nylon, composite nylon/Kevlar, Delrin, acetyl copolymer, phenolic paper, polybutylene terephthalate, Lexan, PVDF fluoropolymer, PVDF fluoropolymer composite, polyetherimide, Teflon, PVC, CPVC, BeH₂, MgH₂, LiH, and LiAlH₄. Fig. 3.2.9 shows how the detector response functions vary for HDPE, polystyrene, and polysulfone in one of the tested instrument configurations (7.62-cm radius and 3.6-cm thickness, as defined in Fig. 3.2.5 LEFT). Figs. 3.2.10 and 3.2.11 were constructed using the optimization procedures described in section 2.3.1; however, the weight restriction of the initial data point grid was relaxed and the radius-thickness parameter space was explored more thoroughly. Fig. 3.2.10 depicts the effect that the varied moderator type had on the instrument's intrinsic detection efficiency to bare ²⁵²Cf. Fig. 3.2.11 shows how the spectral sensitivity metric (Pearson cross-correlation between bare ²⁵²Cf and bare AmBe instrument responses, Eq. 3.2.2) is affected by the different moderators.

Table 3.2.1. Potential instrument moderator material salient properties.

Moderator Material	Chemical Formula	H Concentration (Atoms/cm ³)	C Concentration (Atoms/cm ³)
High Density Polyethylene	(C ₂ H ₄) _n	8.07702E+22	4.29172E+22
Polystyrene	(C ₈ H ₈) _n	4.85521E+22	4.85521E+22
Polysulfone	(OC ₆ H ₄ OC ₆ H ₄ SO ₂ C ₆ H ₄) _n	2.76176E+22	4.14264E+22

The response functions' peak positions and full widths at half maximum (FWHM) provide another means by which spectral sensitivity can be analyzed [23]. As an example, if all of the response functions were non-overlapping delta functions, the energy resolution would be perfect at each response's energy but the sensitivity would be limited only to those energies and, hence, the efficiency would be very small and unacceptable. On the other side, if all of the response functions span the entire energy range, and have the same shape and relative efficiency, the system yields no energy resolution, which is also unacceptable. The desired response functions are those that are narrow in energy, numerous, next to each other with little overlap, and cover the energy range of interest to the application.

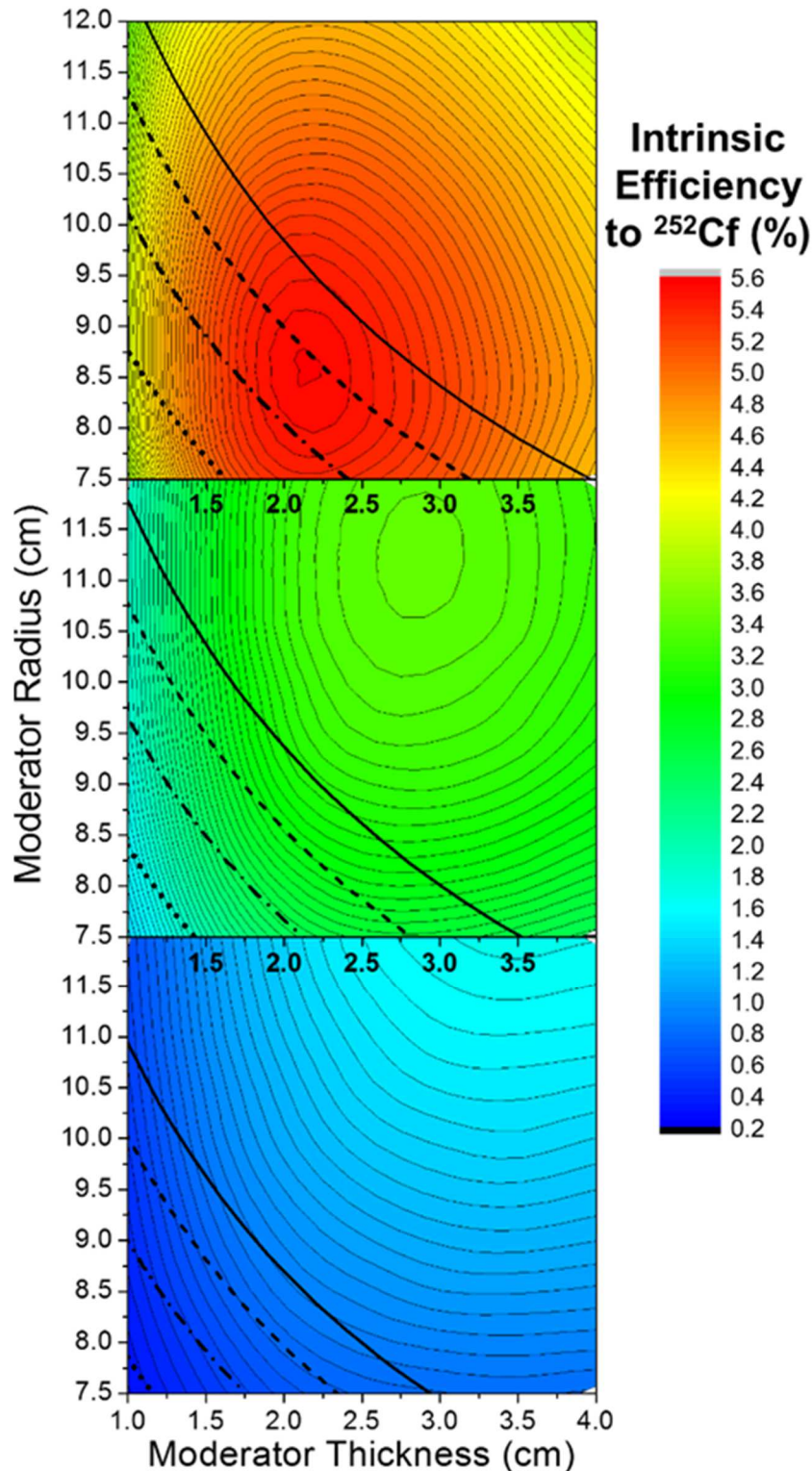


Figure 3.2.10. Instrument intrinsic efficiency to ^{252}Cf as a function of moderator radius and thickness using HDPE (TOP), polystyrene (MIDDLE), and polysulfone (BOTTOM), with iso-mass curves indicating the radius and thickness combinations that yield a total moderator + detector board weight of 6-lbs. (···), 8-lbs. (— · — ·), 10-lbs. (— — —), and 12-lbs. (—).

As shown in Fig. 3.2.9, as the atomic ratio of hydrogen to carbon is decreased from H/C = 2.0 (HDPE) to H/C = 1.0 (polycarbonate) to H/C = 0.6 (polysulfone), the peak position of each detector board response function (with the exception of the front board which has no anterior moderator) is shifted to a lower energy. While this shift to lower energies provides more even coverage of the entire 10^{-9} MeV to 40 MeV energy range shown in Fig. 3.2.9, the vast majority of neutron emissions from bare ^{252}Cf and AmBe (dashed black and red lines in Fig. 3.2.9 respectively) exceed 10^{-1} MeV. The effects of the low energy shift on spectrometer performance are evident from Figs. 3.2.10 and 3.2.11, which depict a significant decrease in instrument intrinsic efficiency to bare ^{252}Cf and increase in Pearson correlation between bare ^{252}Cf and AmBe instrument responses with decreasing hydrogen-to-carbon atomic ratio. However, while these trends are detrimental to instrument performance in application to bare spontaneous fission and (α , n) neutron sources, they are somewhat beneficial to performance in application to moderated variants thereof. After evaluating the effect of this low energy shift on moderated source types, it was determined that the performance benefits for moderated neutron sources are far outweighed by the detriment to bare neutron source performance, and HDPE proved to be the most optimal for a wider range of relevant applications.

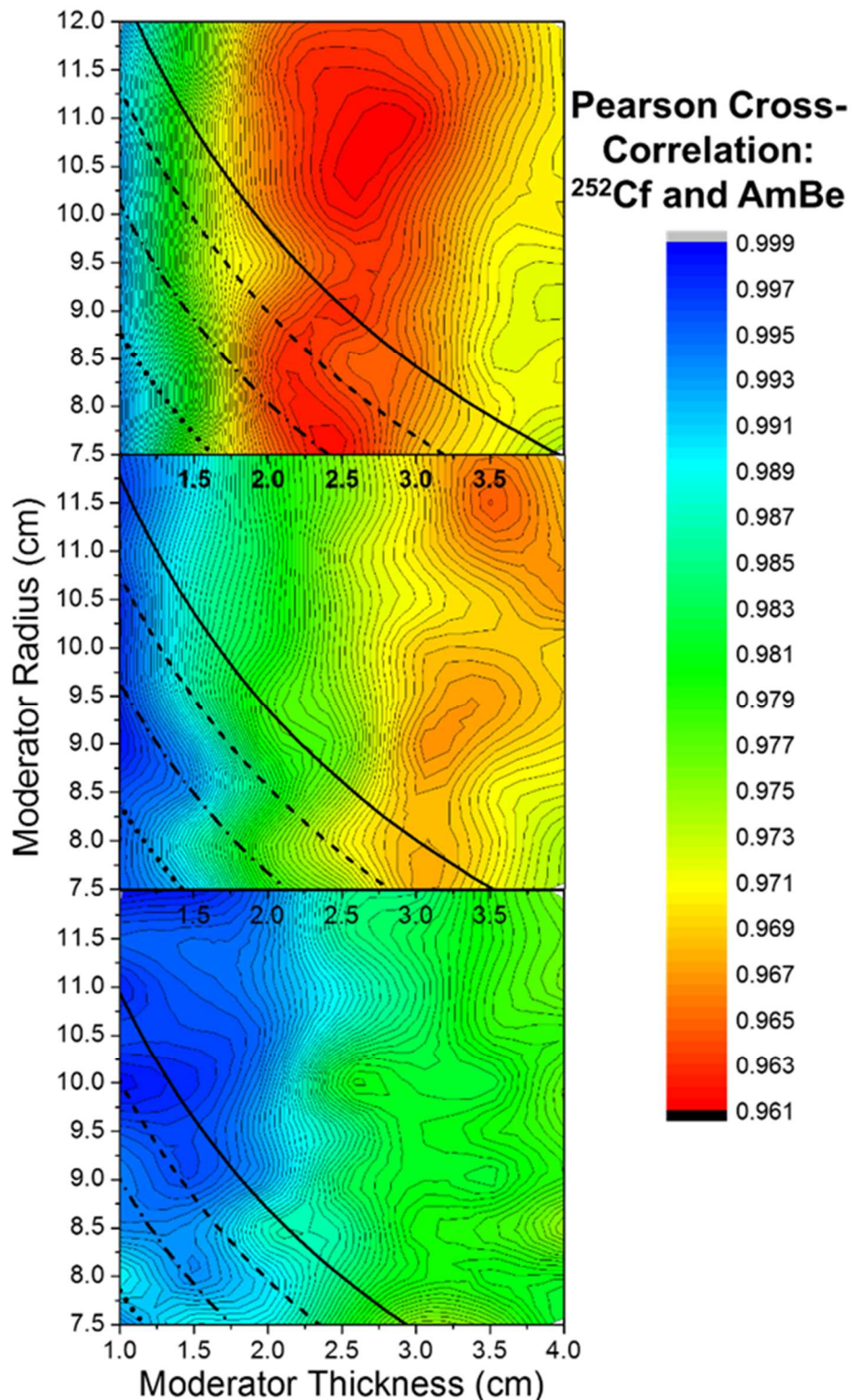


Figure 3.2.11. Pearson Cross-Correlation between ^{252}Cf and AmBe instrument responses as a function of moderator radius and thickness using HDPE (TOP), polystyrene (MIDDLE), and polysulfone (BOTTOM), with iso-mass curves indicating the radius and thickness combinations that yield a total moderator + detector board weight of 6-lbs. (•), 8-lbs. (- · -), 10-lbs. (- - -), and 12-lbs. (-).

3.2.3.5 The Role of Absorbers

Just as varying the moderator type can change the macroscopic neutron scattering distribution, and hence alter the instrument response, intrinsic efficiency, and spectral sensitivity, so too can neutron absorbing materials. As shown in prior work for the long counter and similar geometries to those considered here [15, 22, 24-29], the addition of absorbers can provide two important physical attributes. First, if the neutron absorbers are tuned to capture neutrons at an energy threshold and/or resonance, and those thresholds cover many decades of energy and are strategically placed in space (e.g., stacked), they can act to filter neutrons by energy; this trait alone (i.e., without moderator) creates a crude neutron spectrometer, and can enhance a moderating-type neutron spectrometer. Second, neutron absorbers placed behind stacked detectors, in a moderating-type neutron spectrometer, act to capture some backscattered neutrons. Most backscattered neutrons cause a loss of energy resolution as they defeat the axial depth dependence of forward down-scattering. However, absorbers simultaneously decrease the intrinsic neutron detection efficiency of the instrument and usually cause secondary reaction products (e.g., capture gamma-rays), so their use should be carefully considered in light of the gamma-ray blindness or discrimination capability of the instrument's neutron detectors and the efficiency requirements of the intended application. In the case of the instruments described here, neutron absorbers were serendipitous and unavoidable, as the semiconductor-based neutron detectors were mounted to 0.81-mm (0.032-in.) thick FR4 (E-Glass) printed circuit boards (PCBs), containing the neutron absorbing isotopes ^{79}Br , ^{81}Br , and ^{10}B . The FR4 PCBs absorb 16% of the thermalized neutrons at each detector layer, improving energy resolution by screening backscattered neutrons, at the cost of decreased intrinsic neutron detection efficiency.

3.3 Instrument Builds and Testing

Based on the design methods described above, four moderating-type neutron spectrometers were built to test and compare the empirical response of different instrument configurations. Here forward, the instrument systems will be referred to as the 5-inch cylinder (5C), shown in Fig. 3.3.1, the 6-inch cylinder (6C), shown in Fig. 3.3.2, the 4-inch rectangular prism (4RP), shown in Fig. 3.3.4, and the 4-inch cylinder (4C), shown in Fig. 3.3.5.

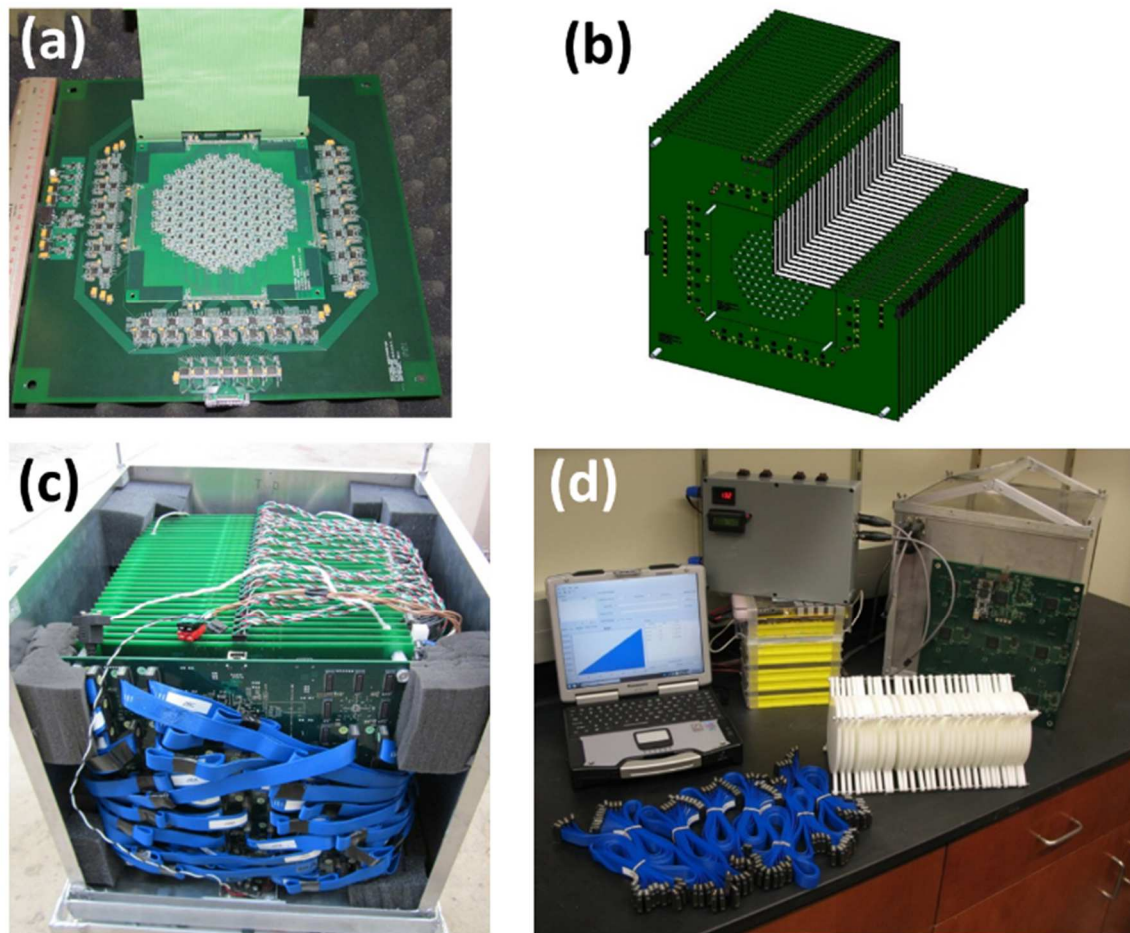


Figure 3.3.1. Photographs and renderings of the 5C spectrometer, showing (a) an individual printed circuit board with mounted microstructured neutron detector die, (b) assembly cut-away view showing thirty alternating board-moderator pairs, (c) assembled instrument with

the top and back cover removed, and **(d)** instrument case, HDPE moderator, cables, battery, power supply, battery, and digital signal processing board.

The 5C was the first instrument built; comprised of thirty detector boards, each containing 108 hexagonally-shaped 1-cm² MSNDs and arranged into the pattern shown in Fig. 3.2.4. On each detector board, all 108 MSNDs were etched as a single monolith into a 5-inch diameter silicon wafer and read out individually through coaxial cables to a digital signal processing board, containing 8 field-programmable gate arrays for the 3240 total channels. When completed, the moderator and detector board assembly weighed 48-lbs. without the case, battery, power supply or laptop. Due to this nearly non-portable mass, overall complexity, and excessive number of channels (*vide infra*), the next three designs focused on reducing the overall mass and volume, while improving operational reliability and effectiveness.

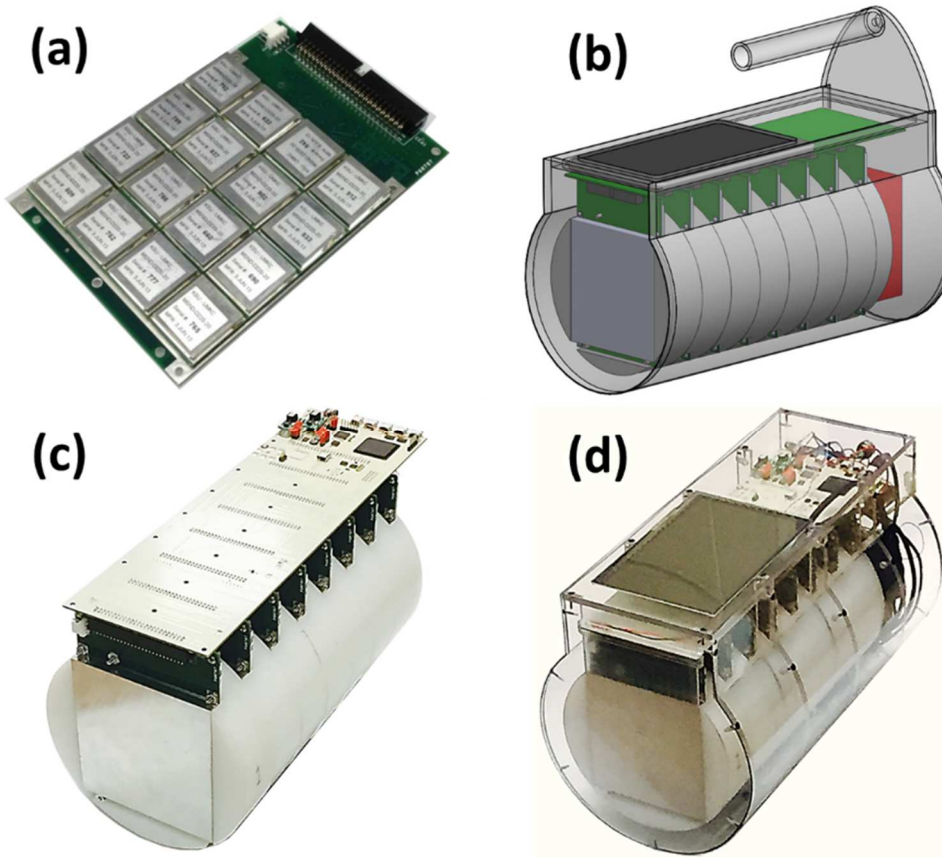


Figure 3.3.2. Photographs and renderings of the 6C spectrometer, showing (a) an individual printed circuit board with mounted microstructured neutron detectors, (b) assembly view showing the eight boards with recessed moderator slabs, motherboard, touchscreen display, battery pack, and case (transparent), (c) assembled instrument with the case, touchscreen display, CPU, and battery packs removed, and (d) fully assembled 6C neutron spectrometer.

In the 6C and 4RP designs, cable connections were removed and the power conditioning, battery, and computer were moved internal to the case. The detector daughter boards are composed of a 4×4 array of 4-cm^2 detectors, shown in Fig. 3.3.2a, with a connector that plugs directly into a motherboard above the moderator volume (Fig. 3.3.2c). Both the 6C and the 4RP designs contain eight daughter boards for a total of 128 individual detector channels per instrument, each channel being read into a single Xilinx Spartan 3AN field-programmable gate array (FPGA). A Nexus 7 tablet (shown in Fig. 3.3.4d) initially served as the user's touchscreen display, the information processor, and the control center of

the motherboard. In subsequent instrument builds, the tablet was replaced by a more powerful CPU and a separate capacitive touch screen display (shown in Fig. 3.3.2d).

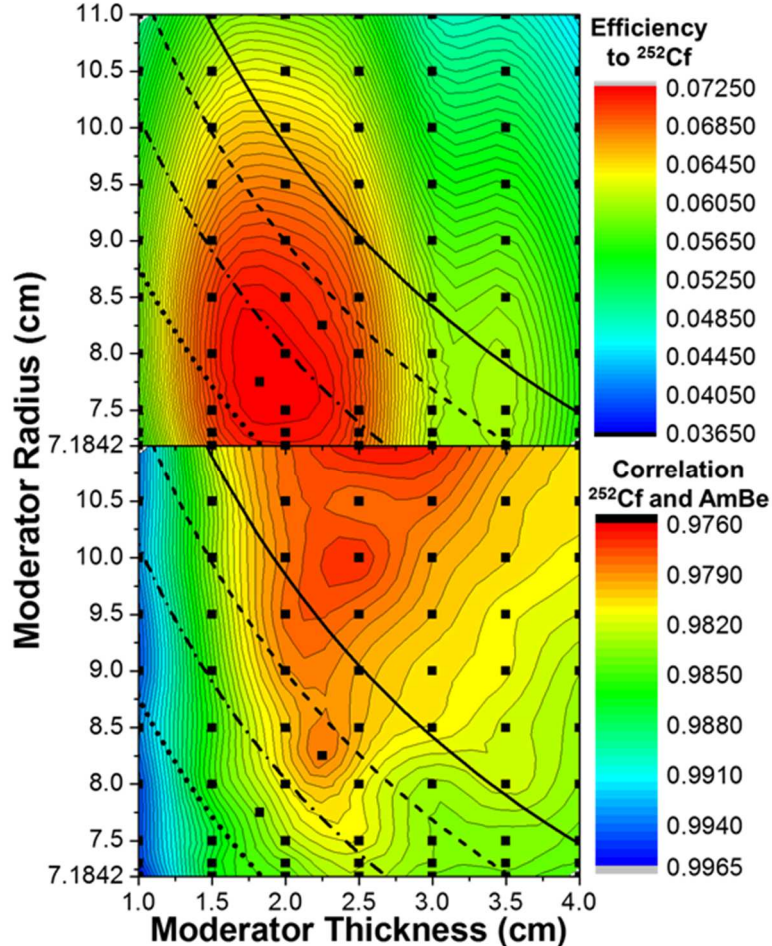


Figure 3.3.3. 6C spectrometer intrinsic efficiency to ^{252}Cf (TOP) and Pearson Cross-Correlation between ^{252}Cf and AmBe 6C spectrometer responses (BOTTOM) as a function of HDPE moderator radius and thickness, with iso-mass curves indicating the radius and thickness combinations that yield a total moderator + detector board weight of 6-lbs. (···), 8-lbs. (— · —), 10-lbs. (— — —), and 12-lbs. (—). Black squares, ▀, show the initially simulated course grid of data points, as well as the optimal data points for each metric (< 10 lbs.).

Using the optimization procedures described in section 3.2.3.1, and restricting the total weight of the moderator and detector boards to be less than 10 lbs. as a design

constraint, the optimal thickness and radius of the 6C moderator slabs (as defined in Fig. 3.2.5 LEFT) was found to be 2.29 cm and 7.62 cm respectively, as represented in Fig. 3.3.3. This radius and thickness combination is a compromise between the optimal intrinsic detection efficiency, at $T = 1.825$ cm and $R = 7.75$ cm, the optimal spectral difference, at $T = 2.25$ cm and $R = 8.25$ cm, and practical availability, with more emphasis given to the intrinsic detection efficiency metric. It should be noted that the 6C moderator slabs envelope the detector boards, instead of simply separating them as portrayed in Fig. 3.2.5. This seemingly minor improvement was found to significantly decrease neutron leakage from the system with a nearly negligible increase in mass. Therefore, with the detector board recess accounted for, the total moderator slab thickness used was 3.6 cm (1.31-cm deep detector board recess, 2.29 cm between detector boards, as shown in Fig. 3.3.2b and 3.3.2c).

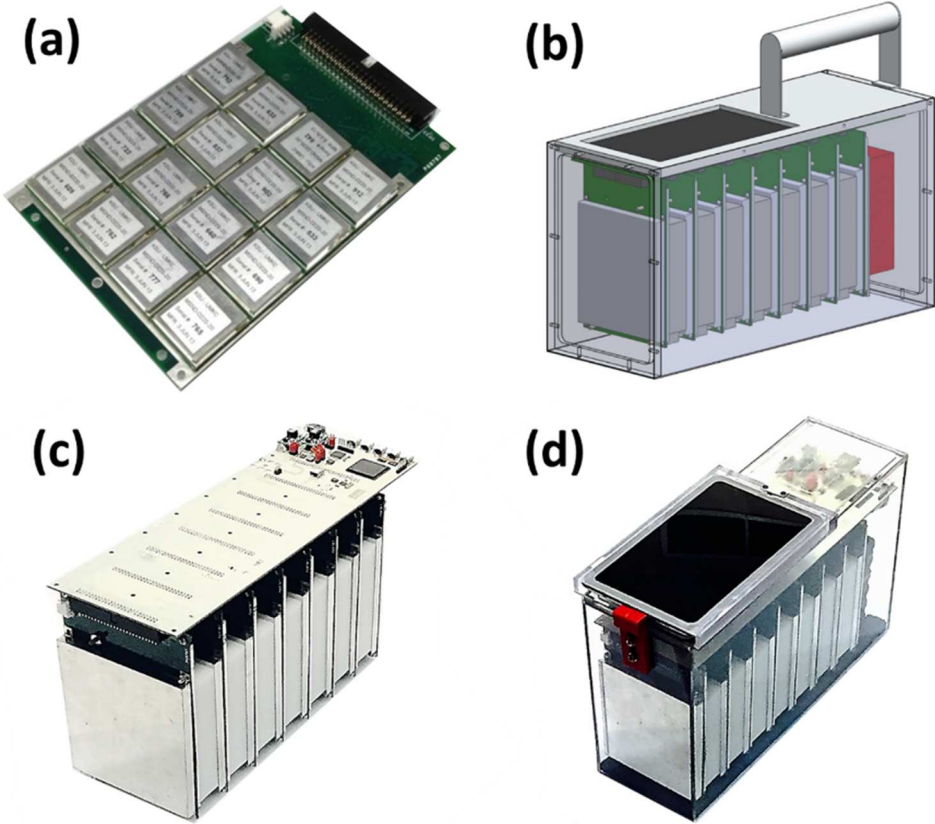


Figure 3.3.4. Photographs and Renderings of the 4RP spectrometer, showing (a) an individual printed circuit board with mounted microstructured neutron detector die, (b) assembly view showing the eight alternating detector-moderator pairs, motherboard, Nexus 7 tablet, battery pack, and case (transparent), (c) assembled instrument with the case, Nexus 7 tablet, and battery packs removed, and (d) fully assembled 4RP neutron spectrometer.

For the 4RP spectrometer, the goal was to utilize the same motherboard as the 6C but reduce the HDPE mass (from that of the 6C) by keeping only the portion separating the detector layers, resulting in a rectangular prism geometry. In doing so, the total instrument weight dropped from 18.5 lbs., for the 6C, to 13.8 lbs. for the 4RP; the moderator portion of the 4RP weight was 3.4 lbs. Using the same moderator radius/thickness optimization procedure, but with the definition given in section 3.2.3.1 (Fig. 3.2.5 RIGHT) for the rectangular-prism radius, the optimal thickness of the HDPE for the 4RP instrument was found to be approximately 2.75 cm to 3.0 cm. Therefore, the same moderator thickness as the

6C design, 2.29 cm, could be used for the 4RP design without significant detriment to either operational performance metric. Since reducing mass while retaining high intrinsic efficiency and spectral sensitivity is critical to the commercial adoption of this type of instrument, it is necessary to understand the tradeoffs between the 6C and 4RP moderator configurations.

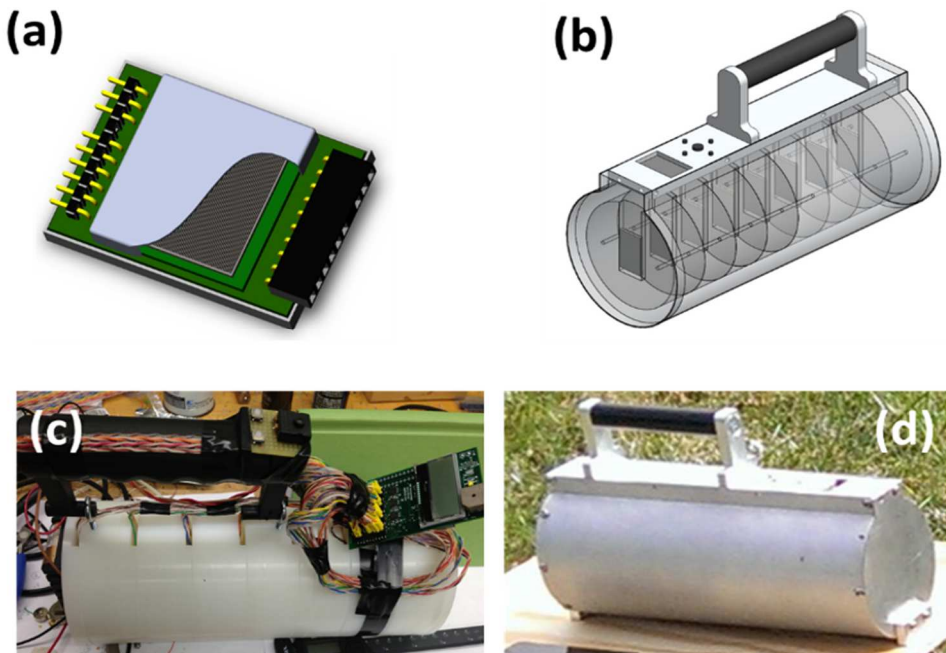


Figure 3.3.5. Photographs and renderings of the 4C spectrometer, showing (a) an individual printed circuit board with single mounted microstructured neutron detector die, (b) assembly view showing the 8-MSNDs with recessed moderator slabs, motherboard, display, and case (transparent), (c) assembled instrument with the case, and battery packs removed, and (d) fully assembled 4C neutron spectrometer.

To consider even more dramatic tradeoffs in cost, mass, and complexity, the 4C moderating-type instrument was designed with a total weight restriction of < 9 lbs. and the use of only one 4-cm² MSND (Fig. 3.3.5a) at each of the eight depths into the moderator volume (Fig. 3.3.5b). The same optimization process illustrated in Fig. 3.3.3 was used to find the optimal radius and thickness combinations for the intrinsic efficiency and spectral

sensitivity. The optimization process yielded a 5-cm radius and 2.25-cm thickness for optimal intrinsic detection efficiency, and a 5-cm radius and 3-cm thickness for optimal spectral sensitivity. A radius of 5.08 cm and thickness of 2.29 cm were used for the actual fabrication of the moderator slabs, based on practical considerations such as the availability of materials, and the total moderator weight was 5.0 lbs. Note that the optimal moderator dimensions for all design models were very similar, due to the predictable probabilistic nature of neutron energy loss and scattering angle via elastic scattering interactions in the common moderator material under consideration (HDPE). While moderator shape and detector board type played minor roles, the small differences in optimal configurations was largely due to the progressively restrictive weight constraints imposed from the 6C to the 4RP and 4C spectrometer designs.

3.3.1 Intrinsic Efficiency¹

The intrinsic neutron detection efficiency, for a particular energy spectrum, was defined in this work as the ratio of the number of neutrons detected to the number of source neutrons incident on the instrument moderator volume (Eq. 3.2.1), represented as a percentage. This definition helps to normalize the results compared between instruments, as it partially accounts for the moderator dimensions. If the intrinsic neutron detection efficiency is reported for two or more faces of each instrument (e.g., front incidence and side incidence), a one-to-one comparison can be made between the detection systems. Further,

¹All empirical intrinsic efficiency results reported here were determined using the shadow shield method, as discussed in section 2.2, with an unshielded ^{252}Cf source. Data was collected until the counting statistics for the overall instrument—propagated through the intrinsic efficiency calculation according to Eq. 2.3.3—yielded less than 2% error. For consistency of results, each empirical test was conducted in the same indoor environment, such that the instruments were positioned 1.2 m above a concrete floor, 2 m below a concrete ceiling, and 5 m from a single concrete wall facing the instrument (to help minimize the asymmetry and overall detection of environmentally scattered neutrons).

one can use the intrinsic neutron detection efficiency to compute the absolute neutron detection efficiency for the source size and distance of interest to their application. This allows for direct comparisons between instruments with respect to the ability to passively detect neutron sources alone. To help put the values reported here in context, with an intrinsic efficiency to bare ^{252}Cf of $\sim 4.5\%$ for neutrons incident on the front face of the 6C instrument (i.e., 182-cm^2 area), a $1\text{E}5\text{-n/s}$ ^{252}Cf source at a standoff distance of 10 m could be detected with 95% certainty (as derived in section 2.3) in 50 seconds.

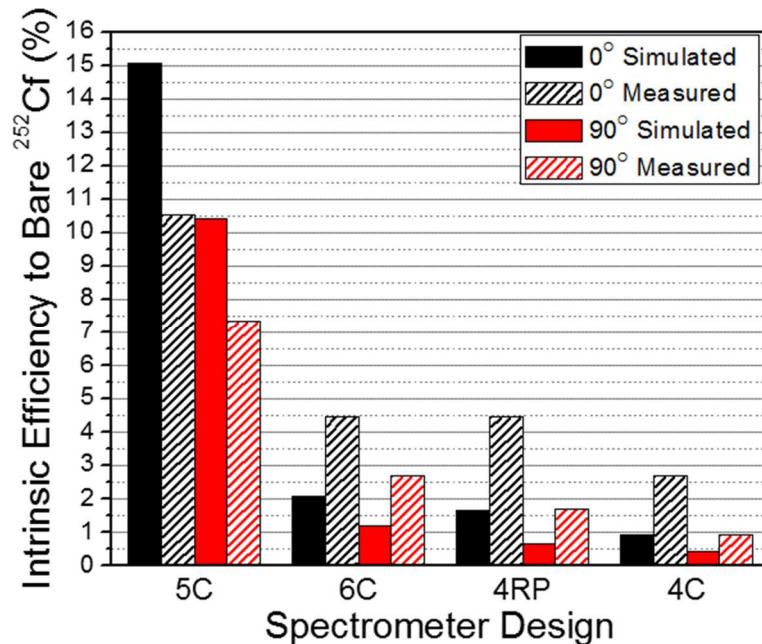


Figure 3.3.6. Simulated and measured intrinsic efficiency to bare ^{252}Cf (in %) for each spectrometer model, from 0° (front face) incidence and 90° (side) incidence.

The simulated and measured intrinsic neutron detection efficiency values to bare ^{252}Cf for each instrument are compared in Fig. 3.3.6 for front and side incidence (0° and 90° , respectively). While the empirically measured intrinsic neutron detection efficiency values to bare ^{252}Cf for the 6C, 4RP, and 4C spectrometers are, on average, 1.7% greater (1.4%

relative) than their simulated values from both the front and side, the measured value of 5C is 4.5% less (30.1% relative) than its simulated value from the front and 3.1% less (29.5% relative) than its simulated value from the side. In the case of the 5C design, the MCNP simulations had to be significantly simplified due to the complexity of the detector electronics boards and did not account for the neutron capture properties of the FR-4 printed circuit board, resulting in a greater efficiency in simulation than experiment. In the case of the 6C, 4RP, and 4C, the detector boards were simpler to model, allowing for the inclusion of the FR-4 PCBs and electronics in simulation, leading to the correct trends for these instruments, as shown in Fig. 3.3.6. The relatively small differences in magnitude between the simulated and measured efficiencies in these cases are mostly due to environmental scattering effects, which were not included in simulation. Environmental neutron scattering leads to an increase in the number of thermalized neutrons impinging on the spectrometer volume and, in turn, a greater intrinsic neutron detection efficiency. The 5C spectrometer achieves the highest overall efficiency values due to having a much larger total active detector area than the other instruments. For a relative comparison, however, the instruments' intrinsic efficiency per cm^2 of total detector area can instead be considered. Viewing the experimental results at 0° (front face) incidence in this detector-area-normalized manner, the efficiency per unit detector area trends in the opposite direction; 0.00277% per cm^2 for the 5C, 0.00876% per cm^2 for the 6C, 0.00874% per cm^2 for the 4RP, and 0.0841% per cm^2 for the 4C. This demonstrates that although intrinsic detection efficiency was sacrificed to some degree with each design simplification (5C → 6C → 4RP → 4C, in order of decreasing complexity) due to decreased moderator volume and/or detector area, the design optimization processes (discussed in previous sections) for each instrument were successful in mitigating

these sacrifices by maximizing efficiency under each increasingly restrictive set of design constraints.

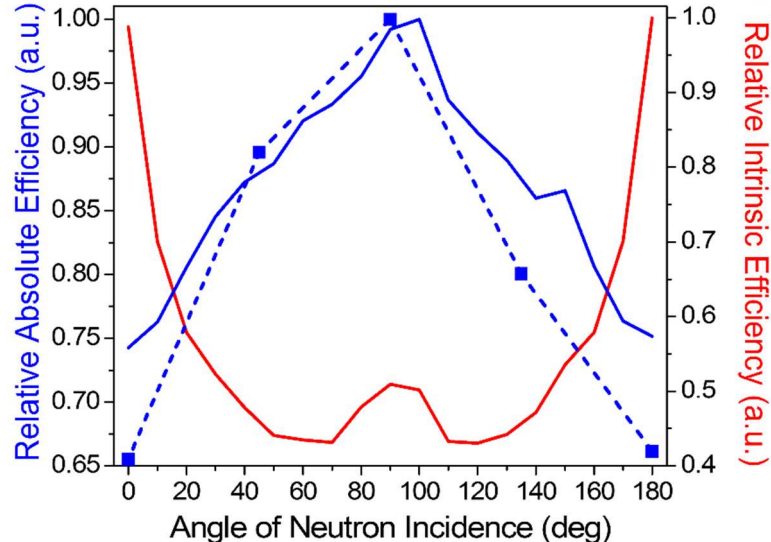


Figure 3.3.7. 5C spectrometer simulated relative intrinsic efficiency (—), Simulated Relative Absolute Efficiency (—), and Experimental Relative Absolute Efficiency (— — —) to bare ^{252}Cf , as a function of neutron incident angle (in degrees). All efficiencies are normalized to allow for direct comparison.

The simulated and measured angular dependence of the absolute neutron detection efficiency, and the simulated angular dependence of the intrinsic neutron detection efficiency, of the 5C design are shown in Fig. 3.3.7, for bare a ^{252}Cf neutron source. In all cases, 0° indicates normal incidence on the front face of the instrument. The reason the intrinsic neutron detection efficiency is highest at 0° and 180° is that, for each of the instruments, much of the latter half of the 30-cm axial depth is used to thermalize incident neutrons from the ^{252}Cf source whose energy is in excess of 5 MeV. In the case of the 5C, the 12.7-cm moderator diameter is not sufficient to thermalize the majority of side-incident neutrons (90°). Absolute detection efficiency is highest for side incidence as the total cross-

sectional area is more than a factor of three greater than the front face of the instrument. The low points in the intrinsic efficiency at $\sim 55^\circ$ and $\sim 125^\circ$ are due to the excess path length of FR4 (intrinsic neutron absorber), and are only specific to the 5C design.

3.3.2 Identification

For this chapter's initial discussion of neutron source type/shielding configuration identification, a one-dimensional template-matching method will be employed, utilizing the previously discussed Pearson product-moment cross-correlation coefficient (Eq. 3.2.2; extensions of, and improvements to, this method will be discussed in chapters 4 and 5 of this work). First, an extensive library of spectrometer responses (summed detector board counts as a function of axial depth, $N(z)$ in cylindrical coordinates, Figs. 3.2.1 and 3.2.2 TOP) must be generated through either MCNP simulation or empirical measurement, and should include as many neutron source types and moderator/absorber configurations as is necessary for a given application. With this library of responses generated and uploaded to the spectrometer's software, live response data collected from an unknown source is then compared to each library response using the Pearson cross-correlation coefficient, r . The library responses are then ranked according to their associated r values, in descending order, and the library source type/shielding configuration corresponding to the largest r value is chosen as the most likely source of the incident neutron radiation (of the libraries uploaded). This process is repeated and displayed to the user in one-second updates as the collected data accumulates.

To test the neutron source identification capabilities of the 6C and 4RP spectrometers under various moderator/absorber configurations as a function of both time and distance from the source, a series of experiments were planned and conducted in a large grass field (Fig.

3.3.8, TOP) at the Naval Surface Warfare Center Carderock Division in West Bethesda, Maryland. The neutron source used for the experiments was a 4.432×10^5 -n/s ($104.77 \mu\text{Ci}$) ^{252}Cf source inside a thin moderating NIST-RG-LL-09-252-D sphere (Fig. 3.3.8A).



Figure 3.3.8. Neutron source identification experimental setup (TOP) with lines indicating radial distances from the neutron source in 0.5-m increments. Neutron source + moderator/absorber configurations tested: (A) 4.432×10^5 n/s ^{252}Cf source inside moderating NIST-RG-LL-09-252-D sphere, (B) 1" HDPE surrounding (A), (C) Four 50-lb sacks of H_3BO_3 tied around (A), and (D) Four 50-lb sacks of H_3BO_3 tied around (B).

As shown in Fig. 3.3.8 (TOP), lines were marked in the grass to indicate radial distances from the NIST sphere-moderated ^{252}Cf source (this will be referred to as source configuration **A**, Fig. 3.3.8A) in 0.5-m increments, from 0.5 m to 5.0 m. Measurements were then taken with both instruments at each distance, with the data collection time adjusted to ensure less than 5% count error. This set of experiments was then repeated three more times with additional moderator/absorber (i.e., shielding) configurations: (**B**) 1" of high density polyethylene surrounding the NIST sphere (Fig. 3.3.8B), (**C**) four 50-lb sacks of H_3BO_3 (boric acid) tied around the NIST sphere (Fig. 3.3.8C), and (**D**) 1" of HDPE plus four 50-lb sacks of H_3BO_3 tied around the NIST sphere (Fig. 3.3.8D). A summary plot of the results of these experiments is shown in Fig. 3.3.9. Neutron source libraries included simulated approximations of configurations **A-D** as well as bare and moderated variants of americium-beryllium (AmBe), plutonium-beryllium (PuBe), and americium-lithium (AmLi).

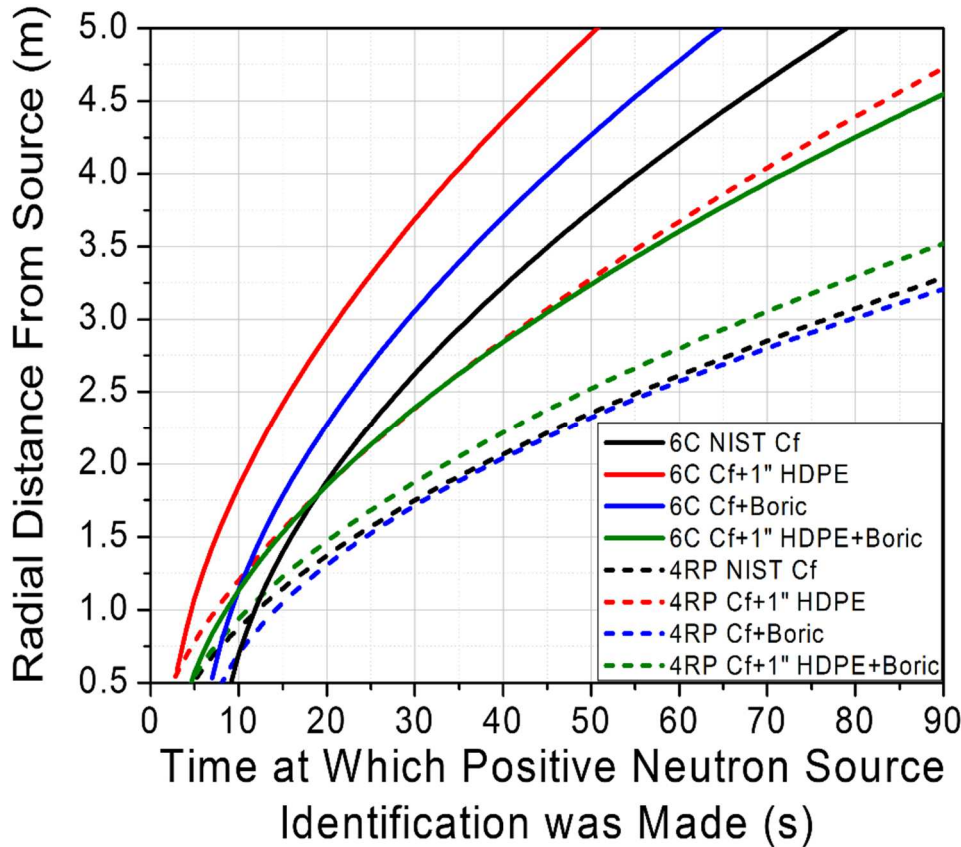


Figure 3.3.9. Neutron source identification experiment summary plot, showing the time at which a positive neutron source + moderator/absorber identification was made (in seconds) vs. radial distance from the neutron source (in meters).

As shown in the summarized empirical results of Fig. 3.3.9, the 6C spectrometer consistently outperforms the 4RP spectrometer in positively identifying neutron sources in less time. In the case of the 6C spectrometer (solid lines in Fig. 3.3.9), the experimental results may seem surprising upon initial inspection, as two of the source configurations with additional moderator/absorber (configurations **B** and **C** in Fig. 3.3.8, solid red and blue lines in Fig. 3.3.9, respectively) were positively identified in less time than the lightly moderated configuration with the NIST sphere alone (configuration **A**, Fig. 3.3.8A, solid black line in Fig. 3.3.9). This result is informative in that it highlights the pragmatically significant relationship between the instrument's intrinsic efficiency and the correlation coefficient

method of neutron source identification. In order to achieve a positive neutron source ID in the shortest amount of time with the correlation coefficient method, a high count rate is needed to provide sufficient counting statistical accuracy in the shortest amount of time. Since the 6C spectrometer is most efficient to neutrons at the bottom end of the fast neutron energy range, the instrument achieved the highest count rate from the source configuration with an additional 1" of HDPE (higher amount of neutron moderation, configuration **B**, Fig. 3.3.8B), and identified this configuration in the shortest amount of time for all distances tested. The **6C** achieved the next highest count rate from the configuration with H₃BO₃ (boric acid) surrounding the NIST sphere (configuration **C**, Fig. 3.3.8C) and yielded the next best identification results. This relatively high count rate is due to the additional moderation via elastic scattering with hydrogen atoms in the boric acid. However, this effect is partially counteracted by moderately high energy neutron absorptions by ¹⁰B atoms (also present in boric acid) at these energies, despite the reduced cross-section. Configuration **D**, with both 1" of HDPE and boric acid surrounding the NIST sphere (Fig. 3.3.8D), yielded the lowest count rate in the **6C** spectrometer. This relatively low count rate is due to the fact that many of the high energy neutrons exiting the NIST sphere are sufficiently moderated by the 1" of HDPE surrounding the sphere to have a high probability of subsequent absorption in the boric acid surrounding the HDPE. However, despite this heavy moderation and absorption, the 6C instrument was still able to positively identify the neutron source in less than 90 seconds at a distance of 4.5 m. Although similar trends can be seen in the 4RP spectrometer results, the aforementioned effects are skewed due to this spectrometer's greater sensitivity to environmental scattering effects. In other words, neutrons scattered off the ground are detected after entering the instrument from the bottom, decreasing the statistical

predictability of the axial count distribution ($N_A(z)$ in Eq. 3.2.2) on which the correlation coefficient method of neutron source identification is based.

Although the identification studies were primarily designed to test the correlation coefficient template-matching method—for the 6C and 4RP spectrometers—against challenges inherent to non-proliferation (e.g., scattering from operational environments), high certainty identification of neutron sources in real time (as shown in Fig. 3.3.9) also has an impact on an instrument’s ability to more accurately measure neutron dose. Specifically, determining the identity of a neutron source and its flux allows for convolution of the exact energy spectrum and fluence with the ICRP 74 standard (International Commission on Radiological Protection publication 74, [30]) to yield an accurate measure of the ambient neutron dose equivalent. This method overcomes the deficiencies of the ‘linear combination of responses’ method presented by Oakes et al. [8]. Alternatively, given the unique and numerous response functions provided by these moderating type neutron spectrometers, the absolute neutron energy and its fluence can also be determined indirectly using unfolding techniques. Application of two unfolding techniques to the instruments introduced in this chapter will be discussed in chapter 6 of this work, and the author recommends future investigation into the methods mentioned here for determining the neutron dose equivalent.

3.4 Conclusions

Four solid-state, moderating-type neutron spectrometers were designed, fabricated, and tested in an effort to improve on the neutron source detection and identification capabilities of long counters and Bonner-sphere-based instruments while making them portable. Through moderator geometry optimization, it was found that an instrument with a cylindrical moderator geometry can achieve a greater intrinsic neutron detection efficiency

and greater energy sensitivity than an instrument with a rectangular prism geometry of the same weight. In studying the effects of individual MSND thermal neutron detection efficiency on overall instrument performance, it was shown that increasing the MSND thermal neutron detection efficiency above 22% provides diminishing returns to an instrument's intrinsic efficiency to bare ^{252}Cf . Through theoretical examination of the ratio between an instrument's outer moderator radius and outer detector radius , an outer detector radius of 3.8 cm and outer moderator radius of 7.8 cm (to reflect outbound neutrons) was found to be optimal for a cylindrical instrument of approximately 15 lbs. After investigation of various moderator materials' effects on operational performance metrics, it was shown that increasing the hydrogen concentration of the moderator material drastically increases an instrument's intrinsic neutron detection efficiency and energy sensitivity. In this materials study, high density polyethylene was found to be more optimal for a wider range of applications than the other materials tested. Of the four fabricated spectrometers, the 5C design exceeds the others in every category of operation, but is the most complex, the most costly to build, and the most physically cumbersome to operate. The 6C, 4RP, and 4C designs were optimized and built to address the deficiencies of the 5C design while simultaneously maximizing their individual operational performance, under increasingly restrictive cost and weight constraints, in order to mitigate the unavoidable tradeoffs associated with decreases in moderator volume and/or active detector area. These four instruments are the first representatives of a new class of hand-held, semiconductor-based, moderating-type neutron spectrometers of varying cost, weight, and design complexity, that provide a means to high intrinsic detection efficiency and neutron source identification

through real-time energy-sensitive measurements of free neutron fields, ranging from thermal energies to the high end of the evaporation spectrum.

CHAPTER 4

METHODS FOR REAL-TIME SOURCE LOCALIZATION AND IDENTIFICATION WITH A MODERATING-TYPE NEUTRON SPECTROMETER

4.1 Introduction

4.1.1 Background and Motivation

In chapter 3 [31], the first representatives of a new class of solid-state moderating-type neutron spectrometer were iteratively designed to improve on multi-sphere- [9, 27] and long-counter-based [11] moderating-type neutron spectrometers. Improvements include reduced instrument mass, greater detection efficiency than the present art, and real-time analysis of energy-sensitive neutron thermalization measurements in three spatial dimensions. This chapter will introduce novel analysis techniques for determining the location and identity of neutron radiation sources with this new class of moderating-type instrument in real time.

4.1.2 The 6C Volumetrically Sensitive Moderating-Type Neutron Spectrometer

Although the general methodologies introduced in this work could be applied to a wide variety of similar instrument designs, the discussion herein will primarily focus on the research team's most successful instrument to date, the 6C (6-inch Cylindrical) moderating-type neutron spectrometer, introduced in chapter 3 (Fig. 3.3.2). The fundamental novelty of the 6C spectrometer's design is that the internal array of 128 thin ($\approx 525 \mu\text{m}$), semiconductor-based, thermal neutron detectors (MSNDs) provides high neutron detection efficiency and volumetric resolution of the average neutron thermalization along three coordinate axes within the moderator-detector assembly, with minimal displacement of the moderating medium. Again, the primary goal of this chapter is to introduce, real-time, algorithmic

methodologies that utilize this highly-efficient, statistically-predictable, three-dimensional neutron thermalization information (see Fig. 4.1.1) to determine the relative location and the identity of neutron radiation sources. To this end, sections 4.2 and 4.3 of this chapter will introduce and discuss the “core” methods (currently implemented in the 6C spectrometer software) for determining the relative location and the identity of neutron sources. Sections 4.4 and 4.5 will then explore extensions of—and potential improvements to—these core methodologies.

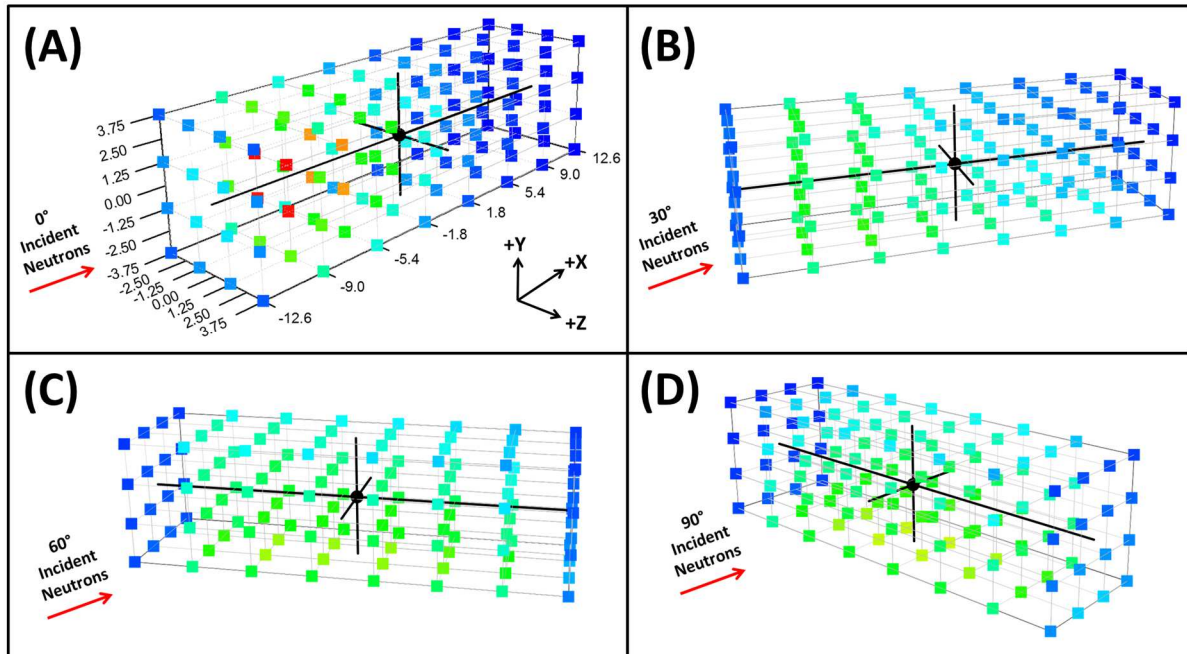


Figure 4.1.1. Simulated examples of 6C spectrometer responses—relative MSND detection intensities (color scale) as a function of (x,y,z) position (in cm, coordinate system shown in Figure A) within the cylindrical moderator volume—to a bare ^{252}Cf spontaneous fission neutron source [7, 8] at a standoff distance of 2 m, showing relative source-to-spectrometer angular orientations of (A) 0°, (B) 30°, (C) 60°, and (D) 90°. Common color scale: **highest detection intensity = Red → lowest detection intensity = Dark Blue**, normalized to Figure A.

4.2 Neutron Response Vectorization (NRV) Method for Determining Neutron Source Location

4.2.1 NRV Method Description

The simulations represented in Fig. 4.1.1 illustrate the statistically-predictable dependence of the 6C spectrometer response (i.e., MSND detection intensities as a function of location within the moderating medium) with respect to the relative angular position of a neutron source of interest in the horizontal plane. Utilizing this dependence, the currently implemented algorithm for determining the location of a neutron source (relative to the 6C spectrometer) employs a 3-dimensional vector-summing method called the neutron response vectorization (NRV) method. Note: the discussion in this section will be in terms of the common coordinate system defined in Figs. 4.1.1A and 4.2.1A unless otherwise specified.

In the first step of this method, each neutron detector in the instrument is assigned a vector, \mathbf{r}_l , describing its physical location relative to the midpoint of the moderating medium's central axis (Fig. 4.2.1B),

$$\mathbf{r}_l = \begin{bmatrix} x_l \\ y_l \\ z_l \end{bmatrix}, \quad \text{for } l = 1, \dots, Q, \quad (4.2.1)$$

where Q is the total number of detectors in the system (for the 6C spectrometer, $Q = 128$). Next, geometric corrections are made to account for instrument asymmetries. By way of example, in the case of the 6C spectrometer, since the internal MSND arrays form a rectangular-prism-shaped grid within the moderator volume (as shown in Fig. 4.1.1), the currently-implemented NRV algorithm for this instrument employs a vector of Cartesian geometric expansion coefficients, $\boldsymbol{\Lambda} = [\lambda_x, \lambda_y, \lambda_z]^T$, to multiplicatively transform the

position vectors, $\mathbf{r}_l = [x_l, y_l, z_l]^T$, from their original rectangular prism orientation, to an expanded cubic form (Fig. 4.2.1C). This transformation is given by

$$\mathbf{c}_l \equiv \mathbf{r}_l \circ \boldsymbol{\Lambda} = \begin{bmatrix} x_l \cdot \lambda_x \\ y_l \cdot \lambda_y \\ z_l \cdot \lambda_z \end{bmatrix}, \text{ where} \quad (4.2.2)$$

$$\lambda_x = 1, \quad \lambda_y = \frac{\max(x_l) - \min(x_l)}{\max(y_l) - \min(y_l)}, \quad \text{and} \quad \lambda_z = \frac{\max(z_l) - \min(z_l)}{\max(z_l) - \min(z_l)}$$

(the operator “ \circ ” represents the Hadamard product, i.e., element-wise multiplication). These cubic-oriented position vectors are then normalized to form spherically-oriented unit vectors (Fig. 4.2.1D),

$$\mathbf{u}_l \equiv \frac{\mathbf{c}_l}{|\mathbf{c}_l|} = \frac{\mathbf{r}_l \circ \boldsymbol{\Lambda}}{|\mathbf{r}_l \circ \boldsymbol{\Lambda}|} = \frac{1}{\sqrt{(x_l \cdot \lambda_x)^2 + (y_l \cdot \lambda_y)^2 + (z_l \cdot \lambda_z)^2}} \cdot \begin{bmatrix} x_l \cdot \lambda_x \\ y_l \cdot \lambda_y \\ z_l \cdot \lambda_z \end{bmatrix}. \quad (4.2.3)$$

Since these vectors are oriented spherically, they possess the highest degree of rotational symmetry achievable for the discrete system (i.e., Q discrete unit vectors, \mathbf{u}_l , $l = 1, \dots, Q$). With geometric asymmetries aptly accounted for and each position vector normalized, the number of neutron counts registered by each detector, N_l , is then multiplied by its associated unit vector, \mathbf{u}_l , resulting in a set of detector response vectors (Fig. 4.2.1E)

$$\mathbf{d}_l \equiv N_l \cdot \mathbf{u}_l = N_l \cdot \frac{\mathbf{r}_l \circ \boldsymbol{\Lambda}}{|\mathbf{r}_l \circ \boldsymbol{\Lambda}|} = \frac{N_l}{\sqrt{(x_l \cdot \lambda_x)^2 + (y_l \cdot \lambda_y)^2 + (z_l \cdot \lambda_z)^2}} \cdot \begin{bmatrix} x_l \cdot \lambda_x \\ y_l \cdot \lambda_y \\ z_l \cdot \lambda_z \end{bmatrix}. \quad (4.2.4)$$

All Q detector response vectors are then summed, yielding a single resultant vector (Fig. 4.2.1F),

$$\mathbf{v}^{(R)} \equiv \sum_{l=1}^Q \mathbf{d}_l = \sum_{l=1}^Q N_l \cdot \frac{\mathbf{r}_l \circ \boldsymbol{\Lambda}}{|\mathbf{r}_l \circ \boldsymbol{\Lambda}|}$$

$$= \sum_{l=1}^Q \frac{N_l}{\sqrt{(x_l \cdot \lambda_x)^2 + (y_l \cdot \lambda_y)^2 + (z_l \cdot \lambda_z)^2}} \cdot \begin{bmatrix} x_l \cdot \lambda_x \\ y_l \cdot \lambda_y \\ z_l \cdot \lambda_z \end{bmatrix}. \quad (4.2.5)$$

Since this equation is expressed in terms of each detector's physical position, $\mathbf{r}_l = [x_l, y_l, z_l]^T$ (predetermined/constant), and number of counts registered, N_l (measured/variable), with geometric expansion coefficients, $\Lambda = [\lambda_x, \lambda_y, \lambda_z]^T$ (predetermined/constant), as defined in Eq. 4.2.2, this resultant vector can be calculated from Eq. 4.2.5, alone, as the measured data accumulates (i.e., in real time). The direction of the resultant vector, $\mathbf{v}^{(R)}$, indicates the region of the instrument with the highest average detection intensity, and its magnitude is proportional to the degree of spatial localization (or dispersion) of this high intensity region. Note: both the direction and magnitude of $\mathbf{v}^{(R)}$ are altered, to some degree, with the introduction of any geometric asymmetry corrections, and this must be carefully considered in light of an instrument's design; however, in the case of the 6C spectrometer, the correction step described in Eq. 4.2.2 has been shown to improve the accuracy of this method—in comparison to skipping this step—regardless of source-to-spectrometer relative angular orientation, and has thus been incorporated into the “core” NRV methodology described here, by way of example. This vector, $\mathbf{v}^{(R)}$, is then normalized to produce a resultant unit vector, $\mathbf{u}^{(R)}$, in the expected direction of the neutron source of interest (Fig. 4.2.1G),

$$\mathbf{u}^{(R)} \equiv \frac{\mathbf{v}^{(R)}}{|\mathbf{v}^{(R)}|} = \frac{1}{\sqrt{(v_x^{(R)})^2 + (v_y^{(R)})^2 + (v_z^{(R)})^2}} \cdot \begin{bmatrix} v_x^{(R)} \\ v_y^{(R)} \\ v_z^{(R)} \end{bmatrix}. \quad (4.2.6)$$

Fig. 4.2.1B-D provides a step-by-step visualization of the six major steps of the NRV method. For the example shown in Fig. 4.2.1, the NRV method was applied to a simulated

6C spectrometer response to a bare ^{252}Cf point source 2 meters from what will be defined here as the moderating cylinder's circular "front face", located at $x = -12.6$ cm in Figs. 4.1.1A and 4.2.1A (i.e., the leftmost circular face in Fig. 3.3.2B-D). Notes: (1) Figs. 4.1.1A and 4.2.1A depict the same simulated response data, (2) the ^{252}Cf energy spectrum used in this simulation is a measured spectrum (specifically, an unfolded spectrum from Bonner sphere spectrometer measurements, in which the shadow shield method, as discussed in section 2.2, was employed to correct for environmental scatter contributions; [18, 32]), (3) in the common coordinate system shown in these figures, the position of the ^{252}Cf point source was [-212.6 cm, 0 cm, 0 cm], (4) no environmental factors, other than the presence of air, were included in this simulation (i.e., no floor/ground, ceiling, walls, objects, etc. were simulated), (5) in total, 90,594 neutrons were detected by the instrument in this simulation.

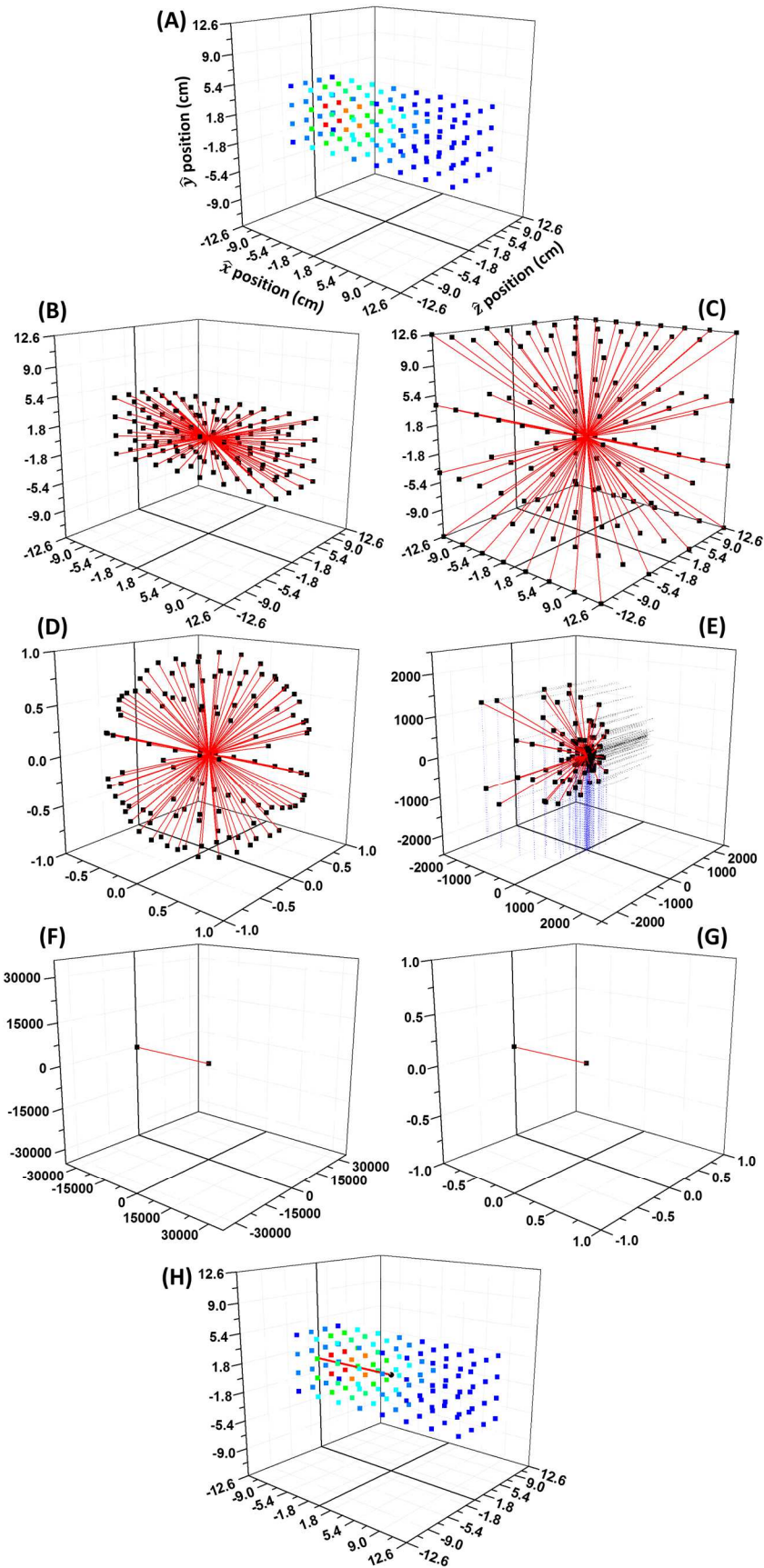


Figure 4.2.1. Neutron response vectorization (NRV) method illustrations. **(A)** Simulated 6C spectrometer response to a bare ^{252}Cf point source located at (-212.6, 0, 0) in the defined coordinate system (axis labels common in Figs. A-H). **(B-G)** Step-by-step visualization of the NRV method, applied to (A); showing **(B)** initial detector position vectors \mathbf{r}_l (Eq. 4.2.1), **(C)** post-asymmetry-correction cubic-oriented position vectors \mathbf{c}_l (Eq. 4.2.2), **(D)** post-normalization spherically-oriented unit vectors \mathbf{u}_l (Eq. 4.2.3), **(E)** detector response vectors \mathbf{d}_l (Eq. 4.2.4; dotted projection lines added for visual clarity), **(F)** summed resultant vector $\mathbf{v}^{(R)}$ (Eq. 4.2.5) with magnitude proportional to the response asymmetry, and **(G)** post-normalization resultant unit vector $\mathbf{u}^{(R)}$ (Eq. 4.2.6) in the suspected direction of the neutron source. **(H)** NRV method result shown in context of Fig. A.

The resultant unit vector (Eq. 4.2.6) obtained through application of the NRV method to this simulated 6C spectrometer response (shown in Fig. 4.2.1G) is $\mathbf{u}^{(R)} \cong [-0.999994, -0.001653, -0.003025]^T$, extremely close to the true (normalized) source direction, $[-1, 0, 0]^T$, in this idealized case (i.e., no environment simulated). However, in most real-world environments, when an empirical measurement is taken in this source-to-spectrometer angular orientation, a small but non-negligible portion of the detected neutrons will undergo scattering interactions (and resultant energy loss) from the ground before entering the instrument volume (note: other sources of room return are discussed below), creating a vertical asymmetry in the instrument response. This response asymmetry results in a false and non-negligible $\mathbf{u}^{(R)}$ vector component in the $-\hat{z}$ direction (i.e., downward; typically between -1° and -10° from the horizontal plane, depending upon environmental conditions). The fact that this \hat{z} component is not indicative of the true source position highlights the primary shortcoming of the NRV method (see [33] for additional information and examples, including the ways in which this effect is exacerbated in active interrogation operational scenarios). From the measurements amassed on the 6C spectrometer, the instrument's response in the vertical dimension has empirically proven to be much more sensitive to variations in environmental scattering conditions than its horizontal-planar

response components (i.e., the instrument's response is more sensitive to ground scatter than other sources of room return, e.g., walls, ceilings, common objects, etc.). Hence, predicting the relative location of a neutron source in the vertical dimension from 6C spectrometer measurements represents a particularly challenging problem, and is outside the scope of this first work regarding the NRV method; it is the author's recommendation that solutions be addressed in future work.

In light of these inherent difficulties regarding vertical angular resolution, the remainder of this chapter regarding neutron source localization will primarily focus on determining the angular location in the horizontal plane. To do so using the NRV method, consider the projection of the vector $\mathbf{v}^{(R)}$ (as defined previously, Eq. 4.2.5) onto the horizontal x-z-plane. Formally, this projection is given by

$$\mathbf{v}^{(H)} \equiv \mathbf{v}^{(R)} - (\mathbf{v}^{(R)} \cdot \mathbf{n})\mathbf{n},$$

where $\mathbf{v}^{(R)} = \begin{bmatrix} v_x^{(R)} \\ v_y^{(R)} \\ v_z^{(R)} \end{bmatrix}$ (as defined in Eq. 4.2.5), and $\mathbf{n} = \begin{bmatrix} 0 \\ 1 \\ 0 \end{bmatrix}$ (unit vector normal to the x-z-

plane), such that

$$\begin{aligned} \mathbf{v}^{(H)} &\equiv \begin{bmatrix} v_x^{(R)} \\ v_y^{(R)} \\ v_z^{(R)} \end{bmatrix} - \left(\begin{bmatrix} v_x^{(R)} & v_y^{(R)} & v_z^{(R)} \end{bmatrix} \begin{bmatrix} 0 \\ 1 \\ 0 \end{bmatrix} \right) \begin{bmatrix} 0 \\ 1 \\ 0 \end{bmatrix} \\ &= \begin{bmatrix} v_x^{(R)} \\ v_y^{(R)} \\ v_z^{(R)} \end{bmatrix} - v_y^{(R)} \cdot \begin{bmatrix} 0 \\ 1 \\ 0 \end{bmatrix} \\ \Rightarrow \mathbf{v}^{(H)} &\equiv \begin{bmatrix} v_x^{(R)} \\ 0 \\ v_z^{(R)} \end{bmatrix}. \end{aligned} \quad (4.2.7)$$

Thus, normalization of $\boldsymbol{v}^{(H)}$ yields the resultant unit vector,

$$\boldsymbol{u}^{(H)} \equiv \frac{\boldsymbol{v}^{(H)}}{|\boldsymbol{v}^{(H)}|} = \frac{1}{\sqrt{(v_x^{(R)})^2 + 0^2 + (v_z^{(R)})^2}} \cdot \begin{bmatrix} v_x^{(R)} \\ 0 \\ v_z^{(R)} \end{bmatrix}, \quad (4.2.8)$$

in the expected direction of the neutron source in the horizontal plane. Note: due to this choice of coordinate system, the horizontal-planar projection is equivalent to ignoring the vertical component.

With $\boldsymbol{u}^{(H)}$ determined, providing a vector description of the expected neutron source location in the horizontal plane, it is now possible to provide a corresponding angular description. The relative source-to-spectrometer angular orientation in the horizontal x-z-plane, θ , will be defined in this work as the angle (measured counterclockwise) between a unit vector in the $-\hat{x}$ direction, $[-1, 0, 0]^T$ (toward the front face of the instrument), and the vector position of the neutron source of interest, projected onto the horizontal plane, $[x_{source}, 0, z_{source}]^T$. Following this definition, the relative source-to-spectrometer angular orientation in the horizontal x-z-plane, as predicted by the NRV method, θ_{NRV} , may then be calculated as the angle (measured counterclockwise) between $[-1, 0, 0]^T$ and $\boldsymbol{u}^{(H)} = [u_x^{(H)}, u_y^{(H)}, u_z^{(H)}]^T$. Eq. 4.2.9 shows how θ_{NRV} (in radians) is calculated in the 6C spectrometer software, conditional upon the values of the x- and z-axial components of $\boldsymbol{u}^{(H)}$ obtained from Eq. 4.2.8 (recall that $u_y^{(H)} = 0$).

$$\theta_{NRV} = \begin{cases} \tan^{-1} \left| \frac{u_z^{(H)}}{u_x^{(H)}} \right| & ; \quad u_x^{(H)} < 0, \quad u_z^{(H)} \geq 0 \\ \pi - \tan^{-1} \left| \frac{u_z^{(H)}}{u_x^{(H)}} \right| & ; \quad u_x^{(H)} > 0, \quad u_z^{(H)} \geq 0 \\ \pi + \tan^{-1} \left| \frac{u_z^{(H)}}{u_x^{(H)}} \right| & ; \quad u_x^{(H)} > 0, \quad u_z^{(H)} < 0 \\ 2\pi - \tan^{-1} \left| \frac{u_z^{(H)}}{u_x^{(H)}} \right| & ; \quad u_x^{(H)} < 0, \quad u_z^{(H)} < 0 \\ \frac{\pi}{4} & ; \quad u_x^{(H)} = 0, \quad u_z^{(H)} < 0 \\ \frac{3\pi}{4} & ; \quad u_x^{(H)} = 0, \quad u_z^{(H)} > 0 \\ undefined & ; \quad u_x^{(H)} = 0, \quad u_z^{(H)} = 0 \end{cases} \quad (4.2.9)$$

4.2.2 6C Software Implementation

As currently implemented in the 6C spectrometer software, the resultant unit vector, $\mathbf{u}^{(H)}$, is displayed graphically—as an arrow indicating the suspected direction of the neutron source of interest—and the angular orientation, θ_{NRV} , is displayed numerically on the source location screen of the instrument’s graphical user interface (GUI) for both static (stationary source and stationary instrument) and dynamic (moving source and/or moving instrument) modes of operation, updating in real time.

4.2.3 Empirical Analysis of the NRV Method

4.2.3.1 Experimental Setup

To empirically test the efficacy of the NRV method with the 6C spectrometer, a series of experiments were conducted indoors, in a 20-ft. x 30-ft. x 11-ft. (height) room with concrete walls and floor (i.e., a high neutron scattering environment, chosen to represent challenging conditions for the NRV method), in which spectrometer measurements were taken at a 2-m standoff distance from a bare 1.5×10^5 -n/s ^{252}Cf source, at relative angular orientations ranging from 0° to 180° in $+10^\circ$ increments (19 empirical measurements total).

Each measurement was terminated once a cumulative count total of 3000 was exceeded for counting-statistical certainty (see section 2.3) and consistency of results (3000 total counts corresponds to a 95% confidence interval of approximately $\pm 0.05^\circ$ using standard error propagation). Measurements were also taken from 180° to 360° , but these are not shown in the figure because the results from 360° to 180° in -10° increments were nearly identical to the results from 0° to 180° in $+10^\circ$ increments due to instrument symmetry.

4.2.3.2 Empirical Results

The results of these empirical tests (Fig. 4.2.2) show that the NRV method, applied to 6C spectrometer measurements (labeled “measured angle” in Fig. 4.2.2), provided an accurate determination of the relative horizontal-planar angular location of the neutron source (labeled “true angle” in Fig. 4.2.2), in a high-scattering environment, with an average angular error of $\pm 7^\circ$ (i.e., $(1/n) \cdot \sum_{i=1}^n |\theta^{(i)} - \theta_{NRV}^{(i)}| = 7^\circ$, with $i = 1, \dots, n$ enumerating the empirical tests conducted). Although this average angular error may be acceptable for many applications, a major goal for this current chapter (and an author-recommended major goal for future methodological developments) is to reduce the average error as much as possible, while also improving error consistency for all source-spectrometer angular orientations (e.g., “measured angles”, using the NRV method, are *consistently* less accurate for “true angles” of 20° - 30° and 100° - 110° than those for true angles of 70° - 80° and 160° - 170° , which is not desirable).

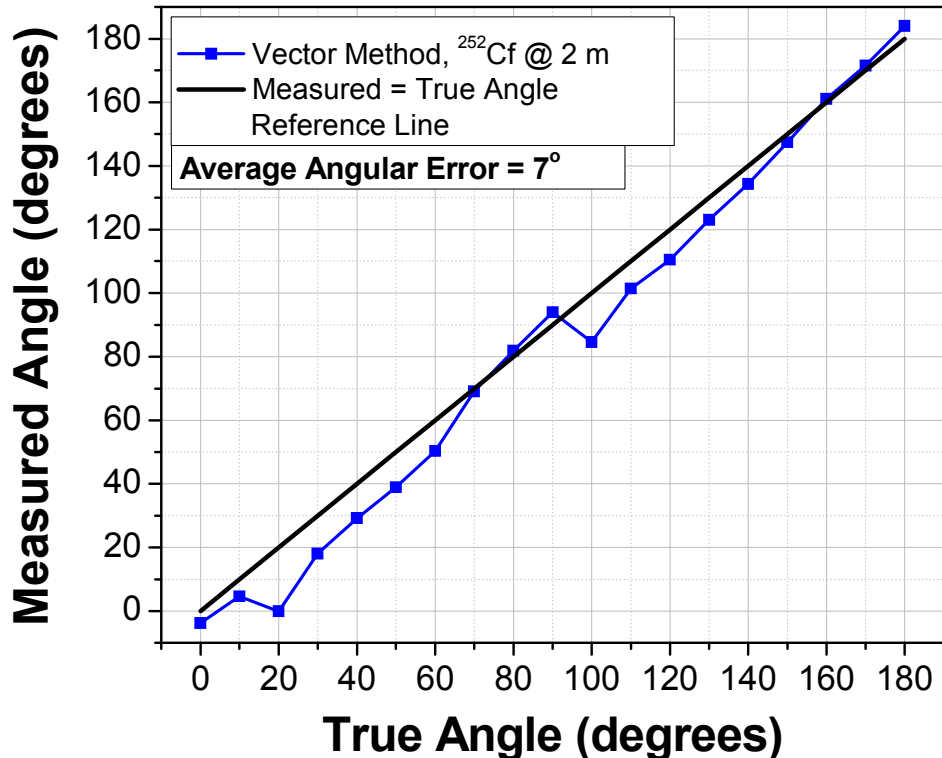


Figure 4.2.2. Summery plot of 6C empirical test results for determining source-to-spectrometer angular orientation in the horizontal plane using the NRV method, showing instrument measurements from a bare 1.5×10^5 -n/s ^{252}Cf spontaneous fission neutron source at a 2-m standoff distance. Measured angle = true angle line (solid black line) included for reference.

It is important to note here, that the apparent trend in the results of Fig. 4.2.2 (from 0° - 90° and repeating from 90° - 180°) is not simply a statistical anomaly, nor is it due to systematic measurement error; this general trend is a direct consequence of the 6C spectrometer's cylindrical geometry (which is asymmetric in the horizontal x-z-plane) in combination with the applied NRV method. The consistency of this observed trend indicates that further geometric-asymmetry corrections can be applied to the NRV method, which could potentially decrease the average angular error for the 6C spectrometer. One such potential algorithmic improvement will be discussed in section 4.5. Having now introduced the core methodology used for determining source location based on 6C spectrometer

measurements; the next section will discuss the core methodologies utilized to determine the identity of a neutron source, and the way in which these methods are algorithmically implemented.

4.3 Pearson Product-Moment Cross-Correlation Spatial Response Analysis

Techniques for Neutron Source Identification

4.3.1 Pearson Cross-Correlation Method Description

The primary goal of the Pearson product-moment cross-correlation methodologies discussed in this section is to determine the most probable identity of a neutron source (i.e., source type and shielding configuration), based upon moderating-type spectrometer measurements, by exploiting the probabilistic—and therefore statistically predictable—nature of neutron scattering and thermalization in a hydrogenous moderating medium. To this end, these methods employ correlation-based template-matching procedures to analyze the response of a volumetrically-sensitive spectrometer in one 1, 2, and/or 3 spatial dimensions (1-dimensional analysis was discussed briefly in chapter 3, but will be detailed in this current section as well for completeness and for comparison purposes), in relationship to a “library” of a priori information (i.e., a database of pertinent information that is knowable prior to measurement). Although this underlying concept could be applied to volumetrically-sensitive moderating-type instruments of nearly any conceivable design, many aspects of such algorithms can potentially be (and, in most cases, *should* be) specifically catered to the geometry of a particular instrument. The remainder of this section will focus on the methods developed specifically for the 6C spectrometer.

For a moderating-type instrument that is inherently invariant to source-to-instrument relative angular orientation (e.g., an idealized Bonner sphere spectrometer, BSS; [9, 27]),

techniques such as those described in this section may be applied in a direct manner; however, for angular-orientation-dependent instruments (e.g., the 6C spectrometer), a reference orientation must be defined prior to application of the spatial response analysis methodologies described herein. For the 6C spectrometer, this reference orientation was chosen such that the instrument’s front circular face (as previously defined in section 4.2.1) is directed toward the neutron source of interest (i.e., 0° angular orientation); and operationally, the user is required—while in “source identification mode”—to reorient the instrument to this reference orientation prior to beginning a source identification data collection. If the user is unaware of the location of a neutron source, the instrument software currently provides a separate “source search mode”, in which the NRV method (discussed in section 4.2) is employed to estimate the location of the source (relative to the instrument) and display this information to the user. Additionally, prior to the application of these spatial response analysis methods, a library of expected or known spectrometer responses must be uploaded to the instrument’s software. These responses, referred to here as “library responses”, are generated through either MCNP simulation or empirical measurement—such that the front circular face of the instrument is oriented toward the neutron source—to include as many neutron source types and shielded variants as necessary for a given application (e.g., a reasonably extensive library, pre-generated by the research team, is currently included in the instrument’s software). Alternatively, a priori source information may be uploaded in the form of neutron energy spectra. In this case, the energy spectra must be normalized, rebinned, and folded into (i.e., multiplied by) the instrument’s response matrix (pre-loaded in the 6C software, for front-face orientation) to generate expected response libraries for the new source type(s). Once all neutron sources of interest are accounted for in the library, the

responses are grouped for 1-, 2-, and/or 3-dimensional analysis (to be discussed in sections 4.3.1.1, 4.3.1.2, and 4.3.1.3, respectively).

With the proper response libraries uploaded and grouped, and the front face of the spectrometer oriented in the suspected direction of the neutron source of interest, the user may start the data collection for neutron source identification. During data collection, the live response data is grouped for 1-, 2-, and/or 3-dimensional real-time comparison to each individual library response using the Pearson product-moment cross-correlation coefficient [19], given by

$$r_{A,B} = \frac{1}{n} \cdot \sum_{i=1}^n \frac{A_i - \bar{A}}{\sigma_A} \cdot \frac{B_i - \bar{B}}{\sigma_B}, \quad (4.3.1)$$

where n is the number of response groupings, $\mathbf{A} = [A_1, A_2, \dots, A_n]^T$ represents the live collection response data set, $\mathbf{B} = [B_1, B_2, \dots, B_n]^T$ represents one library response data set, and \bar{A} , \bar{B} , σ_A , and σ_B represent the averages and standard deviations of response data sets \mathbf{A} and \mathbf{B} . This coefficient results in a value in the range [-1, 1] which is a measure of linear correlation (similarity) between the live instrument response, \mathbf{A} , and a particular library response, \mathbf{B} , where $r_{A,B} = 1$ indicates a total positive correlation (the responses are exactly the same), $r_{A,B} = 0$ indicates no correlation (the responses are entirely different), and $r_{A,B} = -1$ indicates a total negative correlation (the responses are exactly opposite). The square of this correlation coefficient, $r_{A,B}^2$, called the coefficient of determination, results in a value in the range [0, 1] which represents the magnitude of linear correlation (similarity) between the two responses. The single library response that is most positively correlated to the live response, according to the value of $r_{A,B}^2$, is then chosen as the most likely source of the incident neutron radiation (of the libraries uploaded). Notes: (1) the occurrence of a negative

correlation is extremely rare in this application; however, if a correlation, $r_{A,B}$, happens to be negative, the magnitude of correlation is calculated as $-(r_{A,B}^2)$, in order to avoid the misidentification of a negatively correlated response data set. (2) In chapter 3, the Pearson correlation coefficient itself, $r_{A,B}$, was used for the 1-D source identification analysis instead of the coefficient of determination, $r_{A,B}^2$, because that was the way the algorithm was implemented in the instruments' software at the time of the experiments discussed in section 3.3.2. Subsequently, it was determined that the coefficient of determination was the proper metric for this application, and the algorithm was updated in the software according to this section's description.

4.3.1.1 1-Dimensional Spectrometer Response Analysis

For the 1-dimensional response analysis, the counts from all 16 MSNDs are summed for each of the 8 detector daughter boards, providing the spectrometer response as a function of axial depth (Fig. 4.3.1), with each of the 8 data points given by

$$N(x_i) = \sum_{k=1}^{n_z} \sum_{j=1}^{n_y} N(x_i, y_j, z_k) , \quad \text{for } i = 1, \dots, n_x , \quad (4.3.2)$$

where n_x , n_y , and n_z are the number of unique x- y- and z-axial detector positions, respectively (for the 6C spectrometer, $n_x = 8$ and $n_y = n_z = 4$).

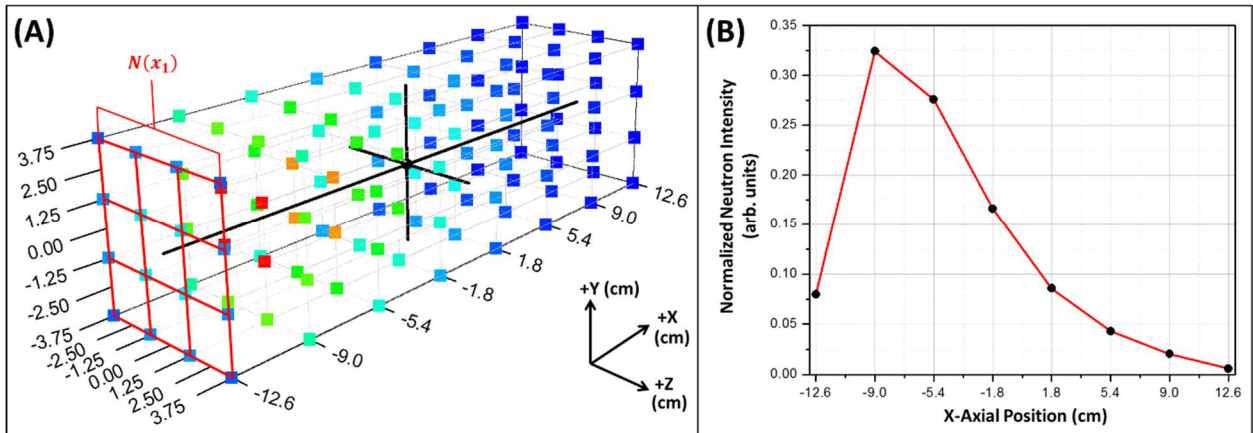


Figure 4.3.1. (A) Example of a 1-dimensional cross-correlation data grouping applied to a simulated 6C spectrometer response to a bare ^{252}Cf neutron source, showing the x-axial grouping for MSNDs located at $x_1 = -12.6$ cm in the defined 3-dimensional coordinate system. **(B)** Linear plot of the grouped 1-dimensional spectrometer response, showing normalized neutron detection intensity (arbitrary units) as a function of x-axial position (in cm) in the coordinate system defined in (A), resulting from application of Eq. 4.3.2 (black circles with red linear interpolation lines).

In this case, the Pearson product-moment cross-correlation coefficient takes the form

$$r_{C,L} = \frac{1}{n_x} \cdot \sum_{i=1}^{n_x} \frac{N_C(x_i) - \overline{N_C(x)}}{\sigma_{N_C(x)}} \cdot \frac{N_L(x_i) - \overline{N_L(x)}}{\sigma_{N_L(x)}}, \quad (4.3.3)$$

where $\mathbf{N}_C(x) = \begin{bmatrix} N_C(x_1) \\ \vdots \\ N_C(x_{n_x}) \end{bmatrix}$ = Collection Response

and $\mathbf{N}_L(x) = \begin{bmatrix} N_L(x_1) \\ \vdots \\ N_L(x_{n_x}) \end{bmatrix}$ = Library Response.

4.3.1.2 2-Dimensional Spectrometer Response Analysis

Noting that the spectrometer responses appear to be radially symmetric about the central x-axis (see Fig. 4.3.1A), it may be beneficial to extend the analysis to include the response's radial dependence. For this 2-dimensional response analysis, the MSND counts are summed according to both their axial position and radial distance from the cylindrical

moderating medium's central axis (three possible radii, Fig. 4.3.2A) in cylindrical coordinates. This data grouping provides the spectrometer response as a function of both radius and axial depth, with each of the 24 data points ($n_\theta = 12$, $n_r = 3$, and $n_x = 8 \Rightarrow n_r \cdot n_x = 3 \cdot 8$) given by

$$N(r_i, x_j) = \sum_{k=1}^{n_\theta} N(r_i, x_j, \theta_k), \text{ for } i = 1, \dots, n_r; j = 1, \dots, n_x. \quad (4.3.4)$$

where n_r and n_x are the number of unique radial and x-axial detector positions, respectively (for the 6C spectrometer, $n_r = 3$ and $n_x = 8$).

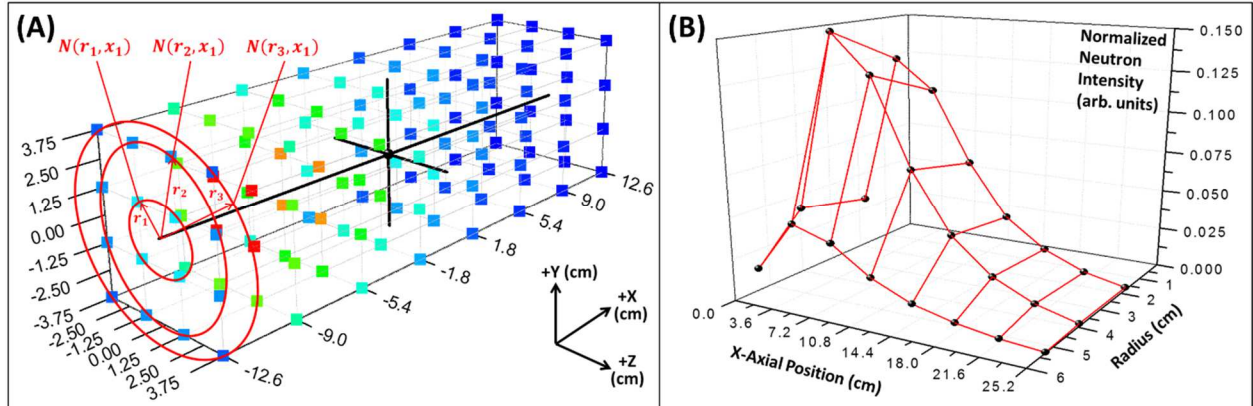


Figure 4.3.2. **(A)** Example of a 2-dimensional cross-correlation data grouping applied to a simulated 6C spectrometer response to a bare ^{252}Cf neutron source, showing the three radial groupings for MSNDs located at $x_1 = -12.6$ cm in the defined 3-dimensional coordinate system. **(B)** Surface plot of the grouped 2-dimensional spectrometer response, showing normalized neutron detection intensity (arbitrary units) as a function of x-axial position (in cm) and radial position (in cm) in the coordinate system defined in (A), resulting from application of Eq. 4.3.4 (black circles with red linear interpolation lines).

In this case, the Pearson Product-Moment Cross-Correlation Coefficient takes the form

$$r_{C,L} = \frac{1}{n_r \cdot n_x} \cdot \sum_{j=1}^{n_x} \sum_{i=1}^{n_r} \frac{N_C(r_i, x_j) - \overline{N_C(r, x)}}{\sigma_{N_C(r, x)}} \cdot \frac{N_L(r_i, x_j) - \overline{N_L(r, x)}}{\sigma_{N_L(r, x)}}, \quad (4.3.5)$$

where $\mathbf{N}_C(r, x) = \begin{bmatrix} N_C(r_1, x_1) \\ \vdots \\ N_C(r_{n_r}, x_{n_x}) \end{bmatrix}$ = Collection Response

and $\mathbf{N}_L(r, x) = \begin{bmatrix} N_L(r_1, x_1) \\ \vdots \\ N_L(r_{n_r}, x_{n_x}) \end{bmatrix}$ = Library Response.

4.3.1.3 3-Dimensional Spectrometer Response Analysis

Although the spectrometer responses appear to possess radial symmetry, small differences between individual detector responses at equal radial and axial positions may actually provide physical insight into the essential scattering physics involved in the process (e.g. preferential scattering angles for neutrons of particular energies, and/or room scatter contributions resulting in response asymmetries). To take full advantage of the response data collected, it may be beneficial to extend our analysis further to include all three physical dimensions of the problem. For this 3-dimensional response analysis, the MSND counts are not summed. Instead, each of the 128 MSNDs is considered as an individual data point on a 3-dimensional grid (shown as squares in Figs. 4.3.1A and 4.3.2A, color-coded according to their relative neutron detection intensities). This method provides the most complete description of the spectrometer response, representing it as a function of x-, y-, and z-axial position within the spectrometer volume, $N(x, y, z)$. In this case, the Pearson product-moment cross-correlation coefficient takes the form

$$r_{C,L} = \frac{1}{n_x \cdot n_y \cdot n_z} \cdot \sum_{k=1}^{n_z} \sum_{j=1}^{n_y} \sum_{i=1}^{n_x} \frac{N_C(x_i, y_j, z_k) - \bar{N}_C(x, y, z)}{\sigma_{N_C(x,y,z)}} \cdot \frac{N_L(x_i, y_j, z_k) - \bar{N}_L(x, y, z)}{\sigma_{N_L(x,y,z)}}, \quad (4.3.6)$$

where $\mathbf{N}_C(x, y, z) = \begin{bmatrix} N_C(x_1, y_1, z_1) \\ \vdots \\ N_C(x_{n_x}, y_{n_y}, z_{n_z}) \end{bmatrix}$ = Collection Response

and $\mathbf{N}_L(x, y, z) = \begin{bmatrix} N_L(x_1, y_1, z_1) \\ \vdots \\ N_L(x_{n_x}, y_{n_y}, z_{n_z}) \end{bmatrix}$ = Library Response.

4.3.2 6C Software Implementation

The library name and 1-, 2-, and 3-dimensional coefficients of determination (r^2) are displayed and updated in real time on the 6C spectrometer's user interface for the top 10 most correlated libraries (10 libraries, 30 r^2 values total shown) in descending order, and may be sorted by 1-D, 2-D, or 3-D coefficient at the operator's discretion (see Fig. 4.3.3 BOTTOM). In addition to this sorted table of values, the operator may also choose to view a real-time-updating coefficient of determination vs. time plot for the top 3 most correlated libraries, providing further insight into the neutron source identification decision as the collected data accumulates (Fig. 4.3.3 TOP).

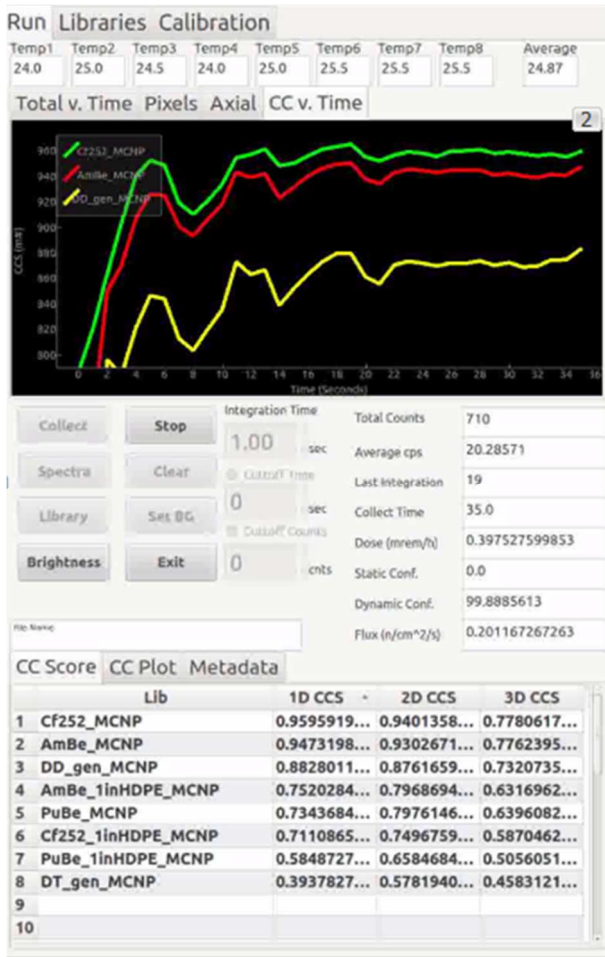


Figure 4.3.3. Screen shot from the 6C spectrometer software taken during an empirical laboratory test at a 5-m standoff distance from a bare 1.5×10^5 -n/s ^{252}Cf neutron source (measurement discussed in section 4.3.3), showing a correct source identification decision 35 seconds into the data collection. **(TOP)** Real-time-updating r^2 value vs. time plot for the top three most correlated source response libraries. **(BOTTOM)** Real-time-updating 1-D, 2-D, and 3-D r^2 value table for the top ten most correlated source response libraries (for illustrative purposes, only eight source libraries shown; sorted according to 1-D r^2 value, in descending order).

4.3.3 Empirical Analysis of Pearson Cross-Correlation Methods

4.3.3.1 Experimental Setup

To test and compare the efficacy of the 1-, 2-, and 3-dimensional Pearson cross-correlation methodologies with the 6C spectrometer, an experiment was conducted in the same 20-ft. x 30-ft. x 11-ft. (height) room described in section 4.2.3.1 (concrete walls and

floor), in which a 5-minute measurement was taken at a 5-m standoff distance from a bare 1.5×10^5 -n/s ^{252}Cf source, at the reference angular orientation, 0° (i.e., such that the instrument's front circular face was directed toward the neutron source). Throughout the 5-minute data collection, the three methods outlined in this section were applied to the accumulated (i.e., time-integrated) measurement data once every second, and the time-dependent results were stored for subsequent analysis. Each time the methods were applied, the accumulated measurement data was compared to the entire pre-generated library of neutron source types and shielded configurations described in the beginning of section 4.3. Only eight of these library responses will be discussed in the following section for illustrative purposes: (1) bare ^{252}Cf (the “true” source type in this experiment) [18, 32], (2) bare AmBe [18, 32], (3) bare PuBe [18, 34], (4) D-D fusion neutron generator (deuterium source – deuterium target, ~ 2.5 MeV), (5) D-T fusion neutron generator (deuterium source – tritium target, ~ 14.1 MeV), (6) ^{252}Cf enclosed in a 1-in. sphere of high density polyethylene (HDPE), (7) AmBe enclosed in a 1-in. sphere of HDPE, and (8) PuBe enclosed in a 1-in. sphere of HDPE. Each of these library responses were generated via MCNP6 simulation, disregarding environmental scattering effects (i.e., no floor/ground, walls, ceiling, etc. were included in the simulations). Note: although results will only be shown for the aforementioned eight library responses, the three most correlated responses in the entire pre-generated library are represented (bare ^{252}Cf , bare AmBe, and D-D generator); the other five library responses were chosen to illustrate additional (α, n) and fusion generator source types, and to compare lightly-shielded variants.

4.3.3.2 Empirical Results

The results obtained from this 5-minute measurement (Fig. 4.3.4A) show that the correct neutron source, bare ^{252}Cf , was identified using each of the three methods discussed in this section. In fact, the screen shot from the instrument's software (Fig. 4.3.3), taken 35 seconds into this measurement (710 total instrument counts), shows that the correct source was already identified at this time using each method.

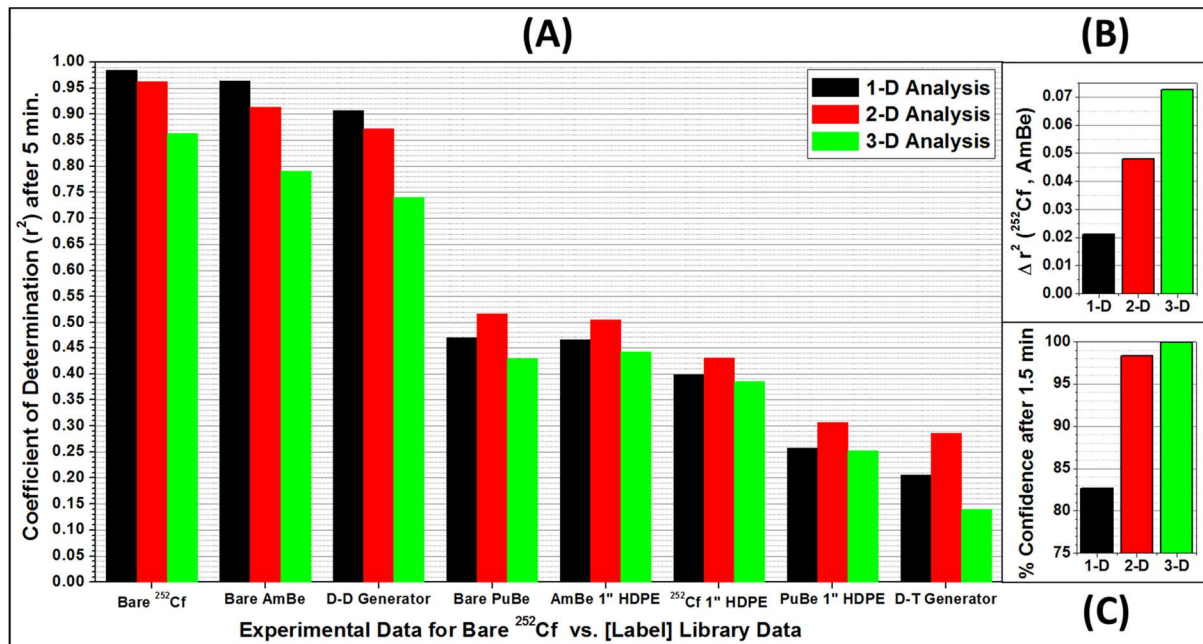


Figure 4.3.4. (A) Summary plot of empirical source identification results from a 5-min 6C spectrometer measurement with a bare 1.5×10^5 -n/s ^{252}Cf spontaneous fission neutron source at a 5-m standoff distance, showing r^2 values obtained from 1-, 2-, and 3-dimensional Pearson correlation analysis techniques applied to experimentally-measured data and 8 library source types. (B) Plot of Δr^2 values (Eq. 4.3.7) for bare ^{252}Cf and bare AmBe vs. method. (C) Plot of % confidence in identification of bare ^{252}Cf after 1.5 minutes vs. method.

When assessing the results in Fig. 4.3.4A, due to the magnitude of the r^2 values, one may incorrectly conclude that the 1-dimensional correlation analysis outperformed the 2-dimensional analysis, and that the 2-dimensional analysis outperformed the 3-dimensional analysis. To more accurately characterize and compare the performance of each method, a

confidence in each identification decision will be defined as the statistical certainty that the highest r^2 value obtained (r^2_1) is truly greater than the second highest r^2 value (r^2_2), or equivalently, the statistical certainty that the difference between the highest r^2 value and the second highest r^2 value (Δr^2) is truly greater than zero (for this test, Δr^2 values for bare ^{252}Cf and bare AmBe are shown in Fig. 4.3.4B for each method).

$$r^2_1 > r^2_2 \Leftrightarrow \Delta r^2 \equiv r^2_1 - r^2_2 > 0 \quad (4.3.7)$$

Basing this confidence upon only the highest two r^2 values can be understood intuitively. If your results show that $r^2_1 > r^2_2 > r^2_3 > \dots > r^2_n$, and you are 98% confident that r^2_1 is truly greater than r^2_2 , then you are more than 98% confident that r^2_1 is truly greater than $r^2_3, r^2_4, \dots, \text{ and } r^2_n$. Since Eqs. 4.3.2-4.3.6, directly depend upon the counts obtained from each thermal neutron detector in the instrument, standard counting statistics (Gaussian for detector measurements with 30 or more total counts, and Poisson for those with less than 30 counts) and propagation of uncertainties (as discussed and employed in section 2.3) can be applied to determine this statistical significance value (the derivation of this confidence metric is straight forward but tedious, and will, thus, not be detailed here; the metric was derived, in part, from concepts outlined in [7, 35, 36]).

Although the ^{252}Cf source was correctly identified 35 seconds into this measurement (Fig. 4.3.3), the confidences in the source identification decision, as defined here, were only 76.75%, 65.55%, and 54.07% for the 1-, 2-, and 3-dimensional methods, respectively, at this time. All three of these confidence values grew steadily as counts accumulated over time, but the confidence for the 3-dimensional analysis grew at the highest rate, the 2-dimensional confidence grew at a moderate rate, and the 1-dimensional confidence grew at the lowest rate. Fig. 4.3.4C shows that the confidence values 1.5 minutes into the measurement were

82.67%, 98.38%, and 99.94% for the 1-, 2-, and 3-dimensional methods, respectively. By the end of the 5-minute measurement, all three methods were successful in correctly identifying the source with >99.9% confidence; however, these results show that increasing the spatial dimensionality of the correlation analysis described in this section allows for a greater source identification confidence in less time.

4.4 Extension of 2-D & 3-D Pearson Cross-Correlation Methods: Simultaneous Neutron Source Localization and Identification

As mentioned in section 4.3, the current implementation of the 1-D, 2-D, and 3-D Pearson correlation methodologies require the user to orient the 6C spectrometer such that its front circular face is directed toward the neutron source of interest prior to starting the source identification data collection. In an effort to eliminate the necessity of this prerequisite, an extension of the 2-D and 3-D Pearson cross-correlation techniques discussed in the previous section was conceived to allow for neutron source identification to be performed at any arbitrary source-to-spectrometer angular orientation. By construction, this methodological extension not only eliminates the instrument reorientation prerequisite for neutron source identification, it also may provide a means to determine the location and identity of a neutron source simultaneously. Prior to discussing this extension in detail, it is necessary to introduce an alternative 2-dimensional spectrometer response data grouping.

4.4.1 Alternative 2-Dimensional Spectrometer Response Analysis

While the 3-dimensional method extension is consistent with the data grouping discussed in section 4.3.1.3 above, the 2-dimensional method extension requires an alternative data grouping to the one introduced in section 4.3.1.2. As discussed in section 4.2.1, the 6C spectrometer's response in the vertical dimension is much more sensitive to

variations in environmental scattering conditions than its horizontal-planar components. To accommodate this known shortcoming, the counts from each vertical column of MSNDs in the instrument are summed for the alternative 2-D response analysis, providing the spectrometer response as a function of x-axial and z-axial position in the horizontal plane (Fig. 4.4.1, below), with each of the 32 data points given by

$$N(x_i, z_k) = \sum_{j=1}^{n_y} N(x_i, y_j, z_k). \quad (4.4.1)$$

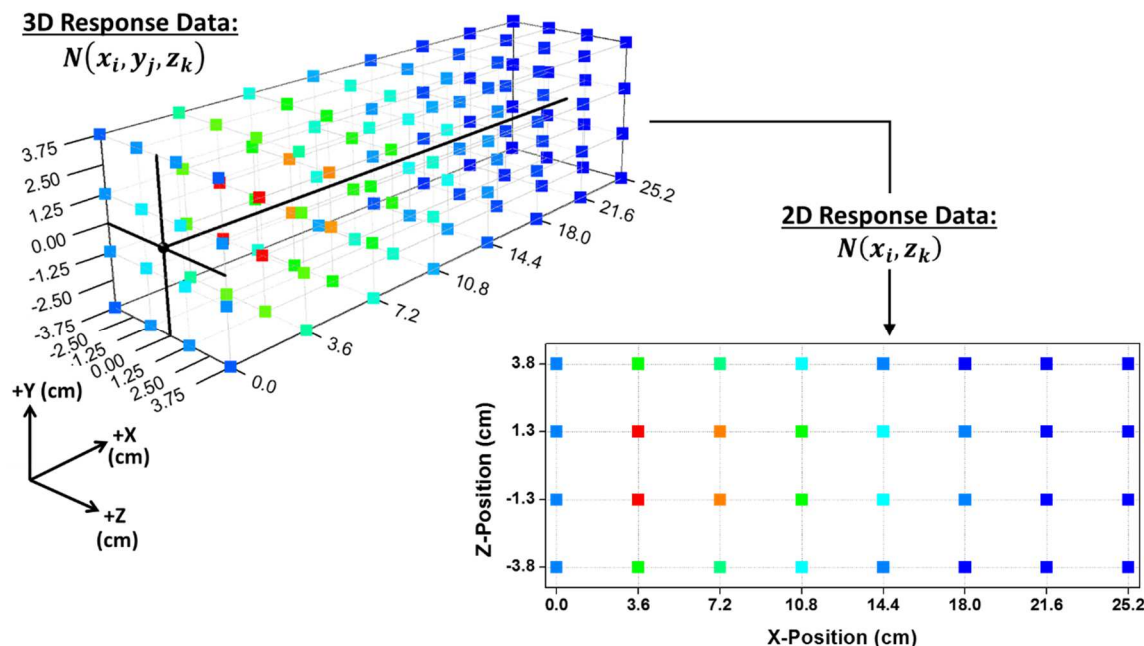


Figure 4.4.1. Example of the alternative 2-dimensional cross-correlation data grouping applied to a simulated 6C spectrometer response to a bare ^{252}Cf neutron source.

4.4.2 2-D and 3-D Pearson Cross-Correlation Method Extension

Recall, from section 4.3.1, that the currently-implemented method for neutron source identification allows for a priori source information to be uploaded in the form of neutron

energy spectra, which are subsequently normalized, rebinned, and “folded into” (i.e., multiplied by) the instrument’s response matrix (pre-loaded in the 6C software, for front-face orientation) to generate expected response libraries for the new source type(s). This functionality serves as the basis for the methodological extension discussed here, in which response matrices are, instead, preloaded in the instrument’s software for source-to-spectrometer angular orientations of $\theta = 0^\circ$ to 355° in 5° increments in the horizontal x-z-plane (72 response matrices total, although the 5° angular increment chosen for this study is relatively arbitrary). For each of these 72 angular orientations, the angular response matrix is generated through a set of MCNP simulations for 128 discretely-binned neutron energy ranges, E_l , which span the range [1.0E-9 MeV, 100 MeV] in even logarithmic decrements (i.e., the quantity $\log_{10}(\max(E_l)/\min(E_l))$ is equal for all 128 binned ranges, E_l , and $\cup_l E_l = [\min(E_1), \max(E_{128})] = [1.0E-9 \text{ MeV}, 100 \text{ MeV}]$). The 128×128 response matrix (one row for each MSND in the instrument, one column for each discretely-binned energy range) for each angular orientation, θ , is then calculated as

$$\begin{aligned} \mathbf{R}_{128 \times 128}^{\theta}(x, y, z, E) \\ = \begin{bmatrix} P(N(x_1, y_1, z_1) | E_1, \theta) & \cdots & P(N(x_1, y_1, z_1) | E_{128}, \theta) \\ \vdots & \ddots & \vdots \\ P(N(x_8, y_4, z_4) | E_1, \theta) & \cdots & P(N(x_8, y_4, z_4) | E_{128}, \theta) \end{bmatrix} \cdot A(\theta), \quad (4.4.2) \\ A(\theta) = D \cdot L \cdot \sin \theta + \frac{\pi}{4} \cdot D^2 \cdot \cos \theta, \quad \theta = 0^\circ, 5^\circ, 10^\circ, \dots, 355^\circ, \end{aligned}$$

where D and L are the diameter and length (in cm), respectively, of the active portion of the instrument (i.e., the cylindrical HDPE moderating volume), $A(\theta)$ is the cross-sectional area (in cm^2) of the active portion of the instrument for which the normal vector is at angular orientation θ (examples shown in Fig. 4.4.2 for the 6C spectrometer: $L \cong 30.48 \text{ cm}$ and $D = 15.24 \text{ cm}$), and each $P(N(x_i, y_j, z_k) | E_l, \theta)$ represents the conditional probability that a

neutron—incident upon the active portion of the instrument—will be detected by the MSND located at (x_i, y_j, z_k) , given that the incident energy of the neutron is in the discrete range E_l , and that the neutron was emitted from a source located at angular orientation θ relative to the instrument.

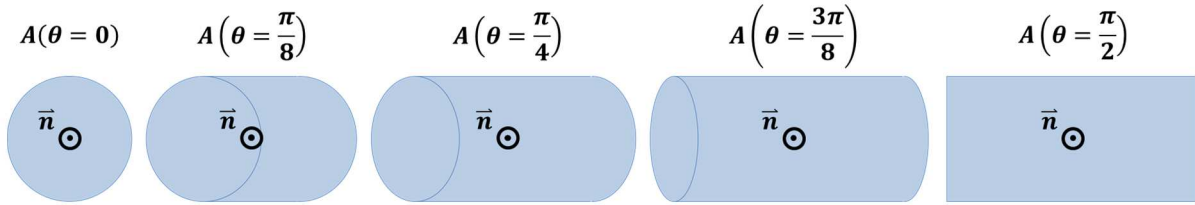


Figure 4.4.2. Illustration of 6C spectrometer cross-sectional areas, $A(\theta)$ in Eq. 4.4.2, (all blue area) for source-to-spectrometer angular orientations of $\theta = 0$ to $\pi/2$ radians (0° to 90°) in $\pi/8$ -radian (22.5°) increments (left to right). For each angular orientation shown, the vector normal to the surface, \vec{n} , is in the direction of the neutron source (directly out of the page in each illustration). Darker blue edge lines added to aid visualization of each moderating cylinder orientation.

With the response matrices calculated according to Eq. 4.4.2, and preloaded in the instrument's software, 3-dimensional library responses can be generated for each angular orientation ($\theta = 0^\circ$ to 355° in 5° increments) for any neutron source of interest by rebinning its neutron energy spectrum to match the response matrix binning structure, and multiplying it by each angular response matrix. This can be shown using the following linear model for the expected 3-dimensional library response to neutron source L at source-to-spectrometer angular orientation θ :

$$N_L^\theta(x, y, z) = R^\theta(x, y, z, E) \cdot \Phi_L(E)$$

$$\Rightarrow \mathbf{N}_L^\theta(x, y, z) = \left(\begin{bmatrix} P(N(x_1, y_1, z_1)|E_1, \theta) & \cdots & P(N(x_1, y_1, z_1)|E_{128}, \theta) \\ \vdots & \ddots & \vdots \\ P(N(x_8, y_4, z_4)|E_1, \theta) & \cdots & P(N(x_8, y_4, z_4)|E_{128}, \theta) \end{bmatrix} \cdot A(\theta) \right) \cdot \left(\begin{bmatrix} P_L(E_1) \\ \vdots \\ P_L(E_{128}) \end{bmatrix} \cdot |\Phi_L(E)| \right), \quad (4.4.3)$$

where $\Phi_L(E)$ is the local (i.e., incident upon the active portion of the instrument), discretized, energy-dependent neutron fluence from source L (in ${}^1_0 n/cm^2$), $|\Phi_L(E)|$ is its magnitude (in the same units), and $[P_L(E_1) \cdots P_L(E_{128})]^T$ is the rebinned energy spectrum of neutron source L (i.e., each $P_L(E_l)$ represents the probability that the energy of a neutron emitted from source L will be in the discrete range E_l). Since the Pearson product-moment cross-correlation coefficient, which will be utilized for this analysis, is invariant to linear combinations, and both the cross-sectional area, $A(\theta)$, and the magnitude of the local neutron fluence, $|\Phi_L(E)|$ will be constants for any static measurement (i.e., stationary source and stationary instrument), these two terms of Eq. 4.4.3 may be ignored (i.e., set to unity) without losing any information pertinent to the source identification analysis, such that

$$\mathbf{N}_L^\theta(x, y, z) = \begin{bmatrix} P(N(x_1, y_1, z_1)|E_1, \theta) & \cdots & P(N(x_1, y_1, z_1)|E_{128}, \theta) \\ \vdots & \ddots & \vdots \\ P(N(x_8, y_4, z_4)|E_1, \theta) & \cdots & P(N(x_8, y_4, z_4)|E_{128}, \theta) \end{bmatrix} \cdot \begin{bmatrix} P_L(E_1) \\ \vdots \\ P_L(E_{128}) \end{bmatrix}. \quad (4.4.4)$$

Operationally, a large list of source spectra $(\mathbf{P}_{L_1}(E), \dots, \mathbf{P}_{L_M}(E))$ is chosen to include as many neutron source types and/or shielded configurations as necessary for a given application. Each of these source spectra are then multiplied by each of the 72 angular response matrices (Eq. 4.4.4) to yield a set of 3-dimensional library spectrometer responses $\mathbf{N}_L^\theta(x, y, z)$, for $\theta = 0^\circ, 5^\circ, \dots, 355^\circ$, and $L = L_1, L_2, \dots, L_M$ ($72 \cdot M$ libraries total, where M is the number of source types and/or shielded configurations of interest). These library

responses are then grouped according to Eq. 4.4.1 for subsequent use in the 2-dimensional analysis,

$$N_L^\theta(x_i, z_k) = \sum_{j=1}^{n_y} N_L^\theta(x_i, y_j, z_k). \quad (4.4.5)$$

Once the desired 2-D and 3-D response libraries have been selected and generated, the source identification data collection may be initiated (without having to reorient the instrument). During data collection, the live response data is grouped for 2- and 3-dimensional real-time comparison to each individual library response using the Pearson cross-correlation method discussed in section 4.3. In this case, the 3-D correlation coefficient is of the form

$$r_{C,L} = \frac{1}{8 \cdot 4 \cdot 4} \cdot \sum_{k=1}^4 \sum_{j=1}^4 \sum_{i=1}^8 \frac{N_C(x_i, y_j, z_k) - \overline{N_C(x, y, z)}}{\sigma_{N_C(x,y,z)}} \cdot \frac{N_L^\theta(x_i, y_j, z_k) - \overline{N_L^\theta(x, y, z)}}{\sigma_{N_L^\theta(x,y,z)}} \quad (4.4.6)$$

where $\mathbf{N}_C(x, y, z) = \begin{bmatrix} N_C(x_1, y_1, z_1) \\ \vdots \\ N_C(x_8, y_4, z_4) \end{bmatrix}$ = 3-D Collection Response

and $\mathbf{N}_L^\theta(x, y, z) = \begin{bmatrix} N_L^\theta(x_1, y_1, z_1) \\ \vdots \\ N_L^\theta(x_8, y_4, z_4) \end{bmatrix}$ = 3-D Library Response,

and the 2-D correlation coefficient is of the form

$$r_{C,L} = \frac{1}{4 \cdot 8} \cdot \sum_{k=1}^4 \sum_{i=1}^8 \frac{N_C(x_i, z_k) - \overline{N_C(x, z)}}{\sigma_{N_C(x,z)}} \cdot \frac{N_L^\theta(x_i, z_k) - \overline{N_L^\theta(x, z)}}{\sigma_{N_L^\theta(x,z)}} \quad (4.4.7)$$

where $\mathbf{N}_C(x, z) = \begin{bmatrix} N_C(x_1, z_1) \\ \vdots \\ N_C(x_8, z_4) \end{bmatrix}$ = 2-D Collection Response

and $\mathbf{N}_L^\theta(x, z) = \begin{bmatrix} N_L^\theta(x_1, z_1) \\ \vdots \\ N_L^\theta(x_8, z_4) \end{bmatrix}$ = 2-D Library Response.

Similar to the Pearson correlation analysis discussed in section 4.3, the 2-D and/or 3-D library response that is most positively correlated to the live collection response, according to the value of the coefficient of determination, $r_{C,L}^2$ (calculated as $-r_{C,L}^2$ if $r_{C,L}$ is negative), is then chosen as the most likely source of the incident neutron radiation (of the source libraries uploaded). Here, however, the most positively correlated response library N_L^θ corresponds to both a particular source-to-spectrometer relative angular orientation in the horizontal x-z-plane, θ , and a particular source type, L ; hence, without being required to reorient the instrument, the user is provided with neutron source location and identification information simultaneously. Furthermore, since the source libraries are generated and loaded prior to data collection (Eqs. 4.4.2-4.4.5), and the cross-correlation calculations are computationally inexpensive (Eqs. 4.4.6 and 4.4.7), this information can be displayed to the user in real-time updates as data is being collected. In preliminary simulation tests, in which 6 source types were simulated in horizontal-planar angular orientations of 0° to 355° in 5-degree increments ($6 \cdot (360/5) = 432$ simulations total), the correct source type was identified in all simulated trials, with average angular location errors of $\pm 2.5^\circ$ for the 2-dimensional method extension (i.e., a 64.29% improvement to the NRV method results in section 4.2.3.2) and $\pm 5^\circ$ for the 3-dimensional method extension (i.e., a 28.57% improvement to the NRV method results). While these initial theoretical results are very promising, empirical tests of these methodological extensions have yet to be conducted, and will be recommended as a subject for future work.

4.5 Post-Hoc Improvement to the NRV Method: NRV-Poly Method

This algorithmic improvement to the neutron response vectorization (NRV) method (section 4.2), called the NRV-Poly method, is based on thoroughly characterizing the

accuracy of the NRV method as a function of true source-to-spectrometer angular orientation, then making post-hoc adjustments to NRV method results based upon this characterization. Thus, section 4.5.1 will discuss one way in which the accuracy of the NRV method (applied to 6C spectrometer measurements) can be characterized analytically, and section 4.5.2 will discuss how this characterization can be utilized to make post-hoc adjustments to NRV method results, improving the accuracy and consistency of horizontal-planar angular orientation determinations.

4.5.1 NRV-Poly Method: Continuous Polynomial Functional Fit Characterization

To characterize the theoretical accuracy of the existing NRV method as a function of true source-to-spectrometer angular orientation, the “base” method (i.e., skipping the geometric asymmetry correction step, Eq. 4.2.2, in the “core” NRV method described in section 4.2) was applied to simulated 6C spectrometer responses to a bare ^{252}Cf neutron source at angular orientations ranging from 0° to 355° in 5° increments. The difference between the angular orientation obtained through application of the NRV method and the true (simulated) angular orientation (i.e. the “base” NRV method errors) were then plotted as a function of the true angular orientation (red and blue circles in Fig. 4.5.1). These data points were then separated, according to the simulated true angle, into two overlapping data sets—data set *A* from -15° (345°) to 195° and data set *B* from 165° to 375° (15°)—and a 13th-order polynomial curve fit (found to provide the best r^2 value fit to the data without overfitting) was applied to each data set using the NumPy “polyfit” Python routine (least-squares polynomial fit, [37]), providing values for the 28 coefficients a_i and b_i in Eqs. 4.5.1 and 4.5.2 below.

$$\theta_{NRV}^{(A)} - \theta = a_0 + a_1 \cdot \theta + a_2 \cdot \theta^2 + \dots + a_{13} \cdot \theta^{13} \quad \text{and} \quad (4.5.1)$$

$$\theta_{NRV}^{(B)} - \theta = b_0 + b_1 \cdot \theta + b_2 \cdot \theta^2 + \cdots + b_{13} \cdot \theta^{13}, \quad (4.5.2)$$

where θ_{NRV} and θ represent the NRV measured angle and true angle (in degrees), respectively, with Eq. 4.5.1 corresponding to data set *A* and Eq. 4.5.2 corresponding to data set *B*.

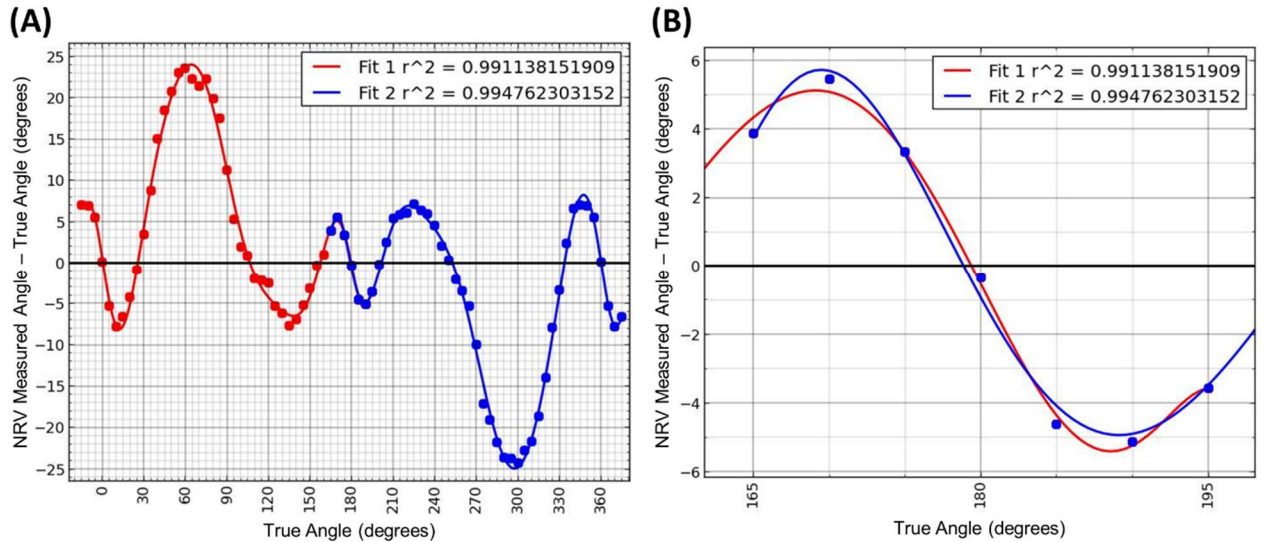


Figure 4.5.1. NRV-Poly method function fitting. **(A)** Plot of simulated results (circles) and 13th-order polynomial curve fits (solid lines) for data sets A (red) and B (blue), showing NRV measured angle – True Angle vs. True Angle with r^2 values for each fit given in the legend. **(B)** Magnified view of the 30-degree overlapping region surrounding True Angle = 180°.

With the coefficients a_i and b_i determined, simple algebraic manipulation of Eqs. 4.5.1 and 4.5.2 yields the desired NRV method characterization: two analytical functions describing the behavior of results obtained through application of the NRV method, θ_{NRV} , as a function true source-to-spectrometer angular orientation, θ , for data sets *A* and *B* (Eqs. 4.5.3 and 4.5.4 below, represented as red and blue lines in Fig. 4.5.2, respectively)

$$\theta_{NRV}^{(A)} = a_0 + (a_1 + 1) \cdot \theta + a_2 \cdot \theta^2 + \cdots + a_{13} \cdot \theta^{13} \quad \text{and} \quad (4.5.3)$$

$$\theta_{NRV}^{(B)} = b_0 + (b_1 + 1) \cdot \theta + b_2 \cdot \theta^2 + \dots + b_{13} \cdot \theta^{13}. \quad (4.5.4)$$

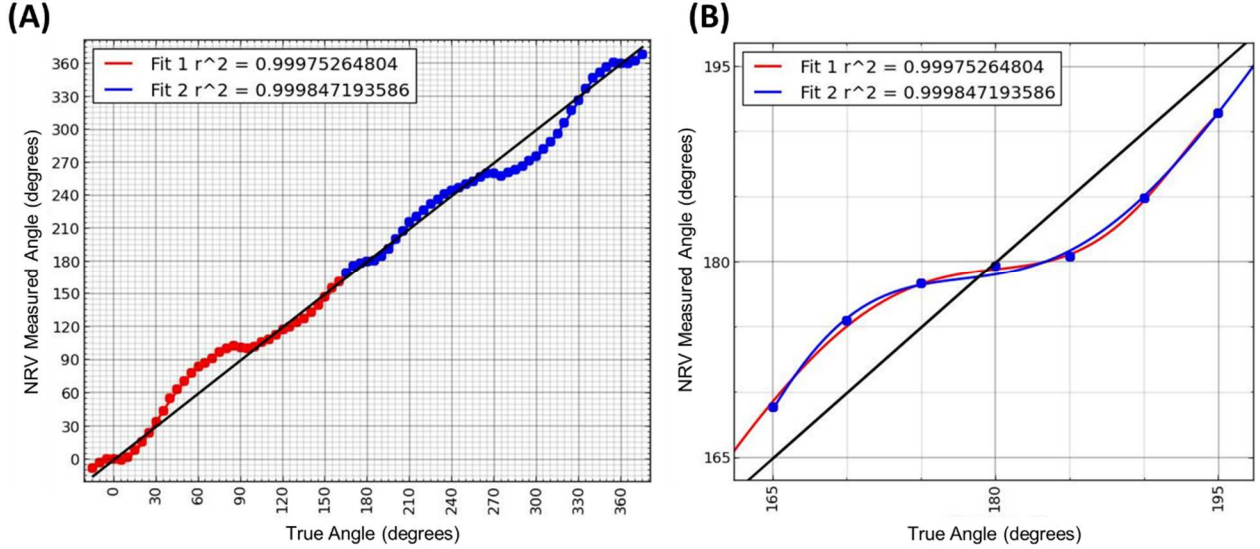


Figure 4.5.2. Desired NRV-Poly method characterization. **(A)** Plot of simulated results (circles) and 13th-order polynomial curve fits (solid lines) for data sets A (red) and B (blue), showing NRV measured angle vs. True Angle with r^2 values for each fit given in the legend. **(B)** Magnified view of the 30-degree overlapping region surrounding True Angle = 180°.

4.5.2 NRV-Poly Method: Post-Hoc Adjustment

When analyzing live measurement data, the NRV-Poly method first uses the “base” NRV method to obtain an initial “NRV measured angle”, θ_{NRV} . If θ_{NRV} is in the range [0°, 180°), it is substituted for $\theta_{NRV}^{(A)}$ in Eq. 4.5.3, and if θ_{NRV} is in the range [180°, 360°), it is substituted for $\theta_{NRV}^{(B)}$ in Eq. 4.5.4. The resulting equation (Eq. 4.5.3 or 4.5.4 with θ_{NRV} substituted) is then solved for θ by finding the roots of the corresponding algebraically manipulated equation,

$$\begin{cases} 0 = (a_0 - \theta_{NRV}) + (a_1 + 1) \cdot \theta + a_2 \cdot \theta^2 + \dots + a_{13} \cdot \theta^{13}, & \theta_{NRV} \in [0^\circ, 180^\circ] \\ 0 = (b_0 - \theta_{NRV}) + (b_1 + 1) \cdot \theta + b_2 \cdot \theta^2 + \dots + b_{13} \cdot \theta^{13}, & \theta_{NRV} \in [180^\circ, 360^\circ] \end{cases} \quad (4.5.5) \quad (4.5.6)$$

using the NumPy “roots” Python routine [37, 38]. Since Eqs. 4.5.5 and 4.5.6 are both 13th-order polynomials, the NumPy roots routine will always return a list of exactly 13 possible solutions for θ (including possible repeated roots). Recognizing that the desired solution should always be real-valued (in this case), the list of possible solutions is then narrowed down by eliminating any solutions with non-zero (or non-negligibly small) imaginary components. From this smaller list of possible real-valued solutions, the solution that is closest to the NRV measured angle, θ_{NRV} , (modulo 360) is chosen as the new “NRV-Poly measured angle”, $\theta_{NRV-Poly}$. Both θ_{NRV} and $\theta_{NRV-Poly}$ are calculated and updated once every software iteration (i.e. every user-defined time step, in seconds) and the results are saved for further analysis. Additionally, two method comparison summary plots are created and saved at the completion of each experiment. Fig. 4.5.3, below, shows example output plots from a simulation in which 5809 total neutrons were detected from a bare ^{252}Cf source at a 300° source-to-spectrometer (true) angular orientation (i.e., $\theta = 300^\circ$).

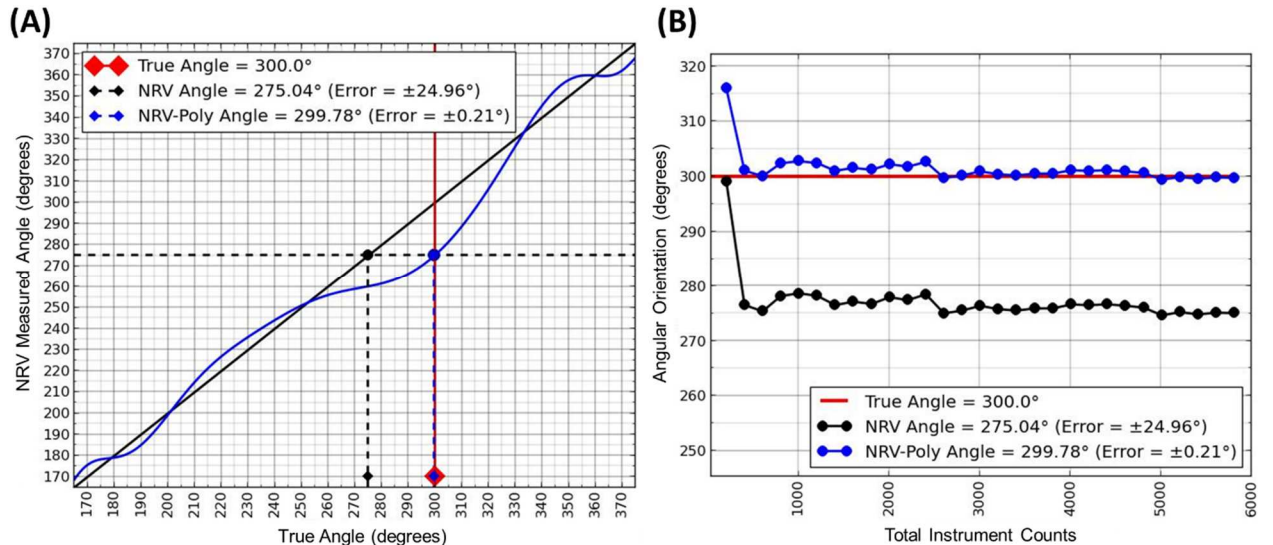


Figure 4.5.3. Example NRV-Poly method output plots from a simulation in which 5809 total neutrons were detected from a bare ^{252}Cf source at a 300° source-to-spectrometer

angular orientation. **(A)** Plot of NRV measured angle vs. true angle, showing final resultant angles (small diamonds and dotted lines) obtained from application of the NRV method (black) and the NRV-poly method (blue), with the polynomial curve fit (solid blue line), true angle (large red diamond and solid red line), and NRV measured angle = true angle line (solid black line) shown for reference. **(B)** Plot of resultant measured angular orientations using the NRV method (black) and the NRV-Poly method (blue) vs. total instrument counts for even time intervals throughout the example simulation (circles and solid linear interpolation lines), with the true simulated angle (solid red line) shown for reference.

As can be seen from the simulated test results in Fig. 4.5.3, the NRV-Poly method appears to be a very promising improvement to the existing NRV method, decreasing the angular error from $\pm 24.96^\circ$ to $\pm 0.21^\circ$ (i.e., a 99.16% improvement) in this case. However, like the Pearson correlation method extensions discussed in section 4.4, empirical analysis will be necessary to determine the true efficacy of the NRV-poly method, and is recommended to be the subject of future work.

4.6 Conclusions and Recommendations for Future Work

Two “core” algorithmic methodologies were presented for determining the relative location and the identity of sources of neutron radiation with a volumetrically-sensitive moderating-type neutron spectrometer. Two extensions of—and potential improvements to—these core methodologies were then proposed. The Neutron Response Vectorization (NRV) Method was introduced as the core methodology for determining the location of a neutron source relative to an instrument. It was shown that the NRV method, when applied to empirical 6C spectrometer measurements, provided an accurate determination of the relative horizontal-planar angular location of a bare ^{252}Cf neutron source, in a high-scattering environment, with an average angular error of $\pm 7^\circ$. Pearson product-moment cross-correlation spatial response analysis techniques (in 1, 2, and 3 spatial dimensions) were then introduced as the core methodologies for determining the most probable identity of a neutron

source. It was shown that each of these spatial response analysis techniques, when applied to empirical 6C spectrometer measurements, were capable of correctly identifying a bare ^{252}Cf neutron source in less than one minute, and that increasing the spatial dimensionality of the correlation analysis allows for a greater source identification confidence in less time. A methodological extension of the 2- and 3-dimensional Pearson cross-correlation techniques was then proposed to simultaneously determine the identity of a neutron source and its relative angular location in the horizontal plane. In a set of 432 simulation tests, the correct source type was identified in all trials, with average angular location errors of $\pm 2.5^\circ$ for the 2-dimensional method extension (i.e., a 64.29% improvement to the NRV method results) and $\pm 5^\circ$ for the 3-dimensional method extension (i.e., a 28.57% improvement to the NRV method results). Lastly, a post-hoc improvement to the NRV method, employing a continuous polynomial fit characterization, was proposed (the NRV-Poly method). In preliminary simulation testing, the NRV-Poly method was shown to be a very promising algorithmic improvement, decreasing the angular error from $\pm 24.96^\circ$ to $\pm 0.21^\circ$ (i.e., a 99.16% improvement) in the example discussed in section 4.5.

Through extensive empirical testing on multiple volumetrically-sensitive moderating-type instruments, the core methodologies introduced in this work (i.e., the Pearson correlation spatial analysis techniques and the NRV method) have proven to be accurate and reliable for determining the identity and horizontal-planar location of sources of neutron radiation in a variety of operational environments; however, the methodological extensions introduced in this chapter could provide improved accuracy and reliability, as well as ease of instrument use. While the initial theoretical results are very promising, thorough empirical tests of the two methodological extensions discussed in sections 4.4 and 4.5 have yet to be

conducted, and are recommended to be the subject of future work. The author recommends that additional future works focus on extending the angular location methodologies discussed here to include the vertical dimension, providing a means to real-time neutron-based source imaging with a portable moderating-type instrument.

CHAPTER 5

ENHANCED KERNEL HILBERT SPACE TEMPLATE-MATCHING TECHNIQUES FOR SIMULTANEOUS NEUTRON SOURCE LOCALIZATION AND IDENTIFICATION

5.1 Introduction

5.1.1 Background and motivation

Template-matching techniques are fundamental to applications requiring pattern recognition in multispectral digital images, such as detecting potential threats in medical images (MRI, CAT, X-ray, etc., [39]), military target detection in forward-looking infrared (FLIR) imaging systems [40], and facial or text recognition [41]. The subject of analysis in such applications is typically a two- or three-dimensional discretized image, for which the information (i.e., orthogonal data) provided by each element is described by its coordinate positions and an intensity value. The discrete coordinate positions are then enumerated, such that the data is described by a single vector. E.g., for a three-dimensional discretized image in Cartesian coordinates, $r_l = (x_i, y_j, z_k)$, where $l = 1, \dots, n_r$ ($n_r = n_x \cdot n_y \cdot n_z$), would represent the enumerated coordinate positions, $I(r_l)$ would represent their associated intensity values, and the image data would be described by the single vector $\mathbf{I} = [I(r_1), \dots, I(r_{n_r})]^T$, in an n_r -dimensional “data space”, or Hilbert space [42]. In this context, the goal of template-matching is to determine whether the subject image, or subsections thereof, “match” one or more known reference images of interest to the application (i.e., templates, described in the same data space), according to an applicable measure of similarity (i.e., correlation coefficient, chi-squared test statistic, etc.). However, template-matching suffers high rates of failure due to template misidentification or false positive template detection, if: (a) the number of templates of interest is large, (b) the templates are very

similar to one another, and/or (c) the data is susceptible to variations in scaling or environmental conditions (e.g., lighting, ambient temperature, etc.).

In the previous chapter (section 4.4), template-matching techniques in two and three spatial dimensions were introduced as methods for simultaneously determining the horizontal-planar location and the identity (i.e., type/isotope and local surrounding/shielding) of neutron radiation sources with a volumetrically-sensitive moderating-type neutron spectrometer. Analogous to the digital imaging applications discussed above, the subject data in this application is a 3-dimensional discretized instrument response, for which the information (i.e., orthogonal data) provided by each element (neutron detector) is described by its coordinate positions within the instrument and an intensity value (the number of neutrons it detects during a measurement). In this context, template-matching is used to compare new measurement data to an extensive template “library” of expected instrument responses to various known neutron source types/radioisotopes, located at various horizontal-planar angular orientations relative to the instrument (e.g., library responses could include the expected instrument response to an unshielded ^{252}Cf spontaneous fission source located at 225° relative to the spectrometer, a lead-shielded AmBe (α, n) source at 30° , etc.), and determine which of these source type and angular position combinations is most likely responsible for the newly measured data. Although the method appeared to be very promising, subsequent simulation testing has revealed that this template-matching application faces similar obstacles to those encountered in the aforementioned digital imaging applications. In the context of neutron measurement analysis: (a), there are a large number of templates of interest (number of templates = number of source types of interest \times number of discretized angular orientations), (b) many of the templates are very similar, and (c) the data

is sensitive to room/environment neutron scatter and counting-statistical fluctuations. In light of these apparent similarities, solutions that have been proposed for digital image processing applications were explored for repurposing, in an effort to overcome the analogous difficulties encountered when analyzing spectroscopic neutron radiation measurements via template-matching techniques.

One potential solution [39, 40, 43], which will be the central focus of this chapter, is to transform both the subject data and the template data from the original data space to an alternate Hilbert space, in which one or more (or even all) of the cited complications are alleviated (or altogether eliminated), prior to applying template-matching techniques. The “feature spaces” of kernel principle component analysis (KPCA) are particularly well-suited candidate Hilbert spaces for this task, since these spaces are specifically constructed to maximize the “distance” between template data sets (commonly referred to as “training” data sets within the KPCA framework) in terms of a distance function (i.e., an inner product) that is defined by the choice of kernel function. Thus, templates that are very similar to one another in the original data space are more easily discernable upon transformation to the KPCA feature space. The primary goal of this chapter is to employ kernel PCA Hilbert space transformations to improve upon the template-matching methods introduced in section 4.4, providing a means to more-accurately determine the location and identity of neutron radiation sources, simultaneously, from hand-held moderating-type neutron spectrometer measurements.

5.1.2 The 6C volumetrically-sensitive moderating-type neutron spectrometer

As was the case for the techniques discussed in chapter 4, although the general methodologies introduced in this chapter could be applied to a wide variety of similar

instrument designs, the discussion herein will primarily focus on the 6C (6-inch Cylindrical) moderating-type neutron spectrometer, introduced in chapter 3 (Fig. 3.3.2). Before detailing the techniques of interest in this current chapter, it is necessary recall a few basic neutron transport principles that are fundamental to the 6C spectrometer’s theory of operation, and briefly review the template-matching method extension introduced in section 4.4.

The central operational principle of the 6C spectrometer is that free neutrons, impinging on the instrument’s active volume (i.e., the cylindrical HDPE, $(C_2H_4)_n$, moderating medium, Fig. 3.3.2), undergo elastic scattering interactions, and subsequent kinetic energy loss, with hydrogen and/or carbon nuclei in the HDPE (i.e., neutron moderation) until their energy is sufficiently reduced (i.e., thermalized) to be detected by one of the instrument’s internal thermal neutron detectors (MSNDs). Thus, on average, the higher an incident neutron’s initial kinetic energy, the further it will penetrate into the instrument volume before being detected. Furthermore, due to inherent asymmetries in the moderating medium’s cylindrical geometry, the physical location (within the active volume) in which a neutron is sufficiently thermalized for detection depends heavily upon its initial angle and position of incidence (see Fig. 4.1.1). Exploiting the probabilistic—and therefore statistically predictable—nature of neutron scattering and thermalization in hydrogenous moderating media, the methods introduced in section 4.4 sought to thoroughly characterize the energy- and angular-dependence of the 6C spectrometer’s response, i.e., intrinsic neutron detection efficiency as a function of physical detector position, source neutron kinetic energy, and source-to-instrument angular orientation, $R^\theta(x, y, z, E)$ (Eq. 4.4.2). This characterization was then used to create an extensive library of instrument response templates for various neutron source types (and shielded variants) located at various horizontal-planar angular orientations

relative to the instrument (Eqs. 4.4.3-4.4.5), to be compared to live measurement data via Pearson correlation-based template-matching procedures (Eqs. 4.4.6 and 4.4.7). Addressing the known shortcomings of such procedures (as discussed in the previous section, 5.1.1), the remainder of this chapter will focus on applying improved template-matching methodologies, based upon kernel principle component analysis (KPCA) transformations, to simultaneously determine the location and identity of neutron sources with the 6C spectrometer. The following section, 5.2, provides a derivation of the KPCA concepts that are central to these methodologies (5.2.1), as well as a description of the KPCA template-matching algorithm to be employed herein (5.2.2). Four variants of this algorithm will then be tested and compared in section 5.3.

5.2 Kernel principle component analysis (KPCA)

5.2.1 Derivation of the KPCA framework

Since the primary shortcoming in applying traditional template-matching techniques to this neutron source location/identification problem is that the library instrument response vectors are very similar (i.e., highly correlated), the goal of KPCA, in this context, is to define a transformation of the library dataset to a new higher-dimensional feature space, and to apply principle component analysis (PCA) techniques in that space to produce uncorrelated “features” in the transformed library vectors. Upon transformation into this less-correlated feature space, the aforementioned shortcoming is sufficiently alleviated, such that traditional template-matching techniques can be applied with a substantially higher degree of accuracy.

As discussed in the previous section, each of the library instrument responses can be defined by a single real-valued vector in an n -dimensional data space, \mathbb{R}^n , which will be denoted

$$\boldsymbol{x}_j \equiv [x_{1j}, \dots, x_{nj}]^T, \quad j = 1, \dots, m, \quad (5.2.1)$$

where $i = 1, \dots, n$ enumerates the detector positions, $j = 1, \dots, m$ enumerates the library source types/angular orientations ($m =$ the number of source types of interest \times the number of discretized angular orientations), and each x_{ij} ($\in \mathbb{R}$) is the expected relative neutron detection intensity of detector i from library source type/angular orientation j . Thus, the entire library of instrument responses is represented by the $n \times m$ “library matrix”

$$\boldsymbol{X}_{n \times m} \equiv [\boldsymbol{x}_1, \dots, \boldsymbol{x}_m] = \begin{bmatrix} x_{11} & \cdots & x_{1m} \\ \vdots & \ddots & \vdots \\ x_{n1} & \cdots & x_{nm} \end{bmatrix}. \quad (5.2.2)$$

To begin, let us consider a generalized unknown functional mapping

$$\phi: \mathbb{R}^n \rightarrow \mathbb{F} \quad (5.2.3)$$

from the original n -dimensional data space, \mathbb{R}^n , to a new D -dimensional ($D > n$) Hilbert space, \mathbb{F} , called a “feature space”, such that each library vector $\boldsymbol{x}_j \in \mathbb{R}^n$ is mapped to $\phi(\boldsymbol{x}_j) \in \mathbb{F}$, and

$$\boldsymbol{X}_{n \times m} \equiv [\boldsymbol{x}_1, \dots, \boldsymbol{x}_m] \rightarrow \boldsymbol{\Phi}_{D \times m} \equiv [\phi(\boldsymbol{x}_1), \dots, \phi(\boldsymbol{x}_m)] \quad (5.2.4)$$

maps the $n \times m$ library matrix, \boldsymbol{X} , in the original data space to a $D \times m$ library matrix, $\boldsymbol{\Phi}$, in the new feature space. Since we desire a Hilbert space transformation that maximizes the “distance” between our library datasets (making them more easily separable), we will now apply a statistical procedure called principle component analysis (PCA, [44]) to the mapped library data, $\boldsymbol{\Phi}$, in feature space. In this context, the goal of PCA is to project the potentially-correlated feature-space library vectors, $\phi(\boldsymbol{x}_i)$, onto a set of linearly uncorrelated vectors via

an orthogonal transformation. Although the mapping functional, $\phi(\cdot)$, has not been defined explicitly, we will assume, for now, that each feature-space library vector, $\phi(\mathbf{x}_j)$, is “centered” (i.e., has a mean of zero; this strong assumption will be addressed later in this derivation). With this assumption, the feature-space library matrix, Φ , is then “column-centered”, allowing us to define the $m \times m$ sample covariance matrix of Φ as

$$\mathbf{C}_{m \times m} \equiv \frac{1}{m} \Phi^T \Phi = \frac{1}{m} \sum_{j=1}^m \phi(\mathbf{x}_j) \phi(\mathbf{x}_j)^T. \quad (5.2.5)$$

To begin our principle component analysis in feature space, we will now consider the eigen-decomposition of this covariance matrix, given by

$$\mathbf{C}\mathbf{v}_i = \lambda_i \mathbf{v}_i, \quad i = 1, \dots, D, \quad (5.2.6)$$

where the λ_i and \mathbf{v}_i are the eigenvalues and eigenvectors, respectively, of the covariance matrix, \mathbf{C} . The eigenvalues of \mathbf{C} represent the variance in the eigen-directions of the feature space, \mathbb{F} , and the eigenvector corresponding to the largest eigenvalue is the direction in which the feature-space library data has the largest variance. Subsequent eigenvectors, corresponding to the 2nd, 3rd, 4th, etc. largest eigenvalues, are mutually orthogonal and are in the direction of 2nd, 3rd, 4th, etc. largest variance. Thus, if Eq. 5.2.6 can be solved for the λ_i and \mathbf{v}_i , projecting our feature-space library vectors, $\phi(\mathbf{x}_j)$, onto these eigenvectors will maximize the variance between them, making the vectors more easily separable in this new feature eigen-space. The feature-space PCA projection of any data-space vector, \mathbf{x} (i.e., any library data vector or new measurement data vector), onto any eigenvector, \mathbf{v}_i , is given by

$$z_i(\mathbf{x}) = \mathbf{v}_i^T \phi(\mathbf{x}). \quad (5.7)$$

However, since we have no definition for the mapping functional, $\phi(\cdot)$, we cannot analytically solve Eq. 5.2.6, as we could if we were performing PCA in the original data

space. Hence, we will now derive a kernel method, called “kernel principle component analysis” (KPCA), for performing PCA in this ill-defined feature space. We will start by substituting the definition of the covariance matrix, Eq. 5.2.5, into its eigen-decomposition equation, Eq. 5.2.6,

$$\begin{aligned}
& \left[\frac{1}{m} \Phi^T \Phi \right] \mathbf{v}_i = \lambda_i \mathbf{v}_i \\
& \Rightarrow \left[\frac{1}{m} \sum_{j=1}^m \phi(\mathbf{x}_j) \phi(\mathbf{x}_j)^T \right] \mathbf{v}_i = \lambda_i \mathbf{v}_i \\
& \Rightarrow \frac{1}{m} \sum_{j=1}^m [\phi(\mathbf{x}_j)^T \mathbf{v}_i] \phi(\mathbf{x}_j) = \lambda_i \mathbf{v}_i \\
& \Rightarrow \mathbf{v}_i = \sum_{j=1}^m \left[\frac{\phi(\mathbf{x}_j)^T \mathbf{v}_i}{m \lambda_i} \right] \phi(\mathbf{x}_j), \quad i = 1, \dots, D. \tag{5.2.8}
\end{aligned}$$

From Eq. 5.2.8, we see that each eigenvector, \mathbf{v}_i , is a linear combination of the feature-space library vectors, $\phi(\mathbf{x}_j)$. Thus, the eigenvalues of \mathbf{C} can be written as

$$\begin{aligned}
\mathbf{v}_i &= \sum_{j=1}^m \left[\frac{\phi(\mathbf{x}_j)^T \mathbf{v}_i}{m \lambda_i} \right] \phi(\mathbf{x}_j) = \sum_{j=1}^m [\alpha_{ij}] \phi(\mathbf{x}_j) \\
&\Rightarrow \mathbf{v}_i = \Phi \boldsymbol{\alpha}_i, \quad i = 1, \dots, D, \tag{5.2.9}
\end{aligned}$$

$$\text{where } \boldsymbol{\alpha}_i = [\alpha_{i1}, \dots, \alpha_{im}]^T = \left[\frac{\phi(\mathbf{x}_1)^T \mathbf{v}_i}{m \lambda_i}, \dots, \frac{\phi(\mathbf{x}_m)^T \mathbf{v}_i}{m \lambda_i} \right]^T, \quad i = 1, \dots, D.$$

Substituting Eq. 5.2.9 into the eigen-decomposition equation, Eq. 5.2.6, yields

$$\begin{aligned}
\mathbf{C}[\Phi \boldsymbol{\alpha}_i] &= \lambda_i [\Phi \boldsymbol{\alpha}_i] \\
&\Rightarrow \left[\frac{1}{m} \Phi^T \Phi \right] \Phi \boldsymbol{\alpha}_i = \lambda_i \Phi \boldsymbol{\alpha}_i \quad [\text{sub: Eq. 5.2.5}] \\
&\Rightarrow \Phi^T \Phi \boldsymbol{\alpha}_i = m \lambda_i \boldsymbol{\alpha}_i
\end{aligned}$$

$$\Rightarrow \mathbf{K}\boldsymbol{\alpha}_i = \tilde{\lambda}_i \boldsymbol{\alpha}_i, \quad i = 1, \dots, D, \quad (5.2.10)$$

where $\tilde{\lambda}_i = m\lambda_i$, and $\mathbf{K} = \Phi^T \Phi$ is a $m \times m$ Gram matrix, with elements $K_{ij} =$

$\phi(\mathbf{x}_i)^T \phi(\mathbf{x}_j)$, i.e., inner products of feature-space library vectors $\phi(\mathbf{x}_i)$ and $\phi(\mathbf{x}_j)$ (note: a Gram matrix is defined as a matrix whose entries are inner products). Eq. 5.2.10 is now a new eigen-decomposition equation for the Gram matrix \mathbf{K} , that is equivalent to the eigen-decomposition equation for \mathbf{C} , Eq. 5.2.6. Since eigenvectors of the covariance matrix, \mathbf{v}_i , should be orthonormal, we have

$$\begin{aligned} \mathbf{v}_i^T \mathbf{v}_i &= 1 \\ \Rightarrow [\Phi \boldsymbol{\alpha}_i]^T [\Phi \boldsymbol{\alpha}_i] &= 1 \quad [\text{sub: Eq. 5.2.9}] \\ \Rightarrow \boldsymbol{\alpha}_i^T \Phi^T \Phi \boldsymbol{\alpha}_i &= 1 \\ \Rightarrow \boldsymbol{\alpha}_i^T \mathbf{K} \boldsymbol{\alpha}_i &= 1 \quad [\text{sub: } \mathbf{K} = \Phi^T \Phi] \\ \Rightarrow \boldsymbol{\alpha}_i^T (\tilde{\lambda}_i \boldsymbol{\alpha}_i) &= 1 \quad [\text{sub: Eq. 5.2.10}] \\ \Rightarrow m\lambda_i \boldsymbol{\alpha}_i^T \boldsymbol{\alpha}_i &= 1 \quad [\text{sub: } \tilde{\lambda}_i = m\lambda_i] \\ \Rightarrow \|\boldsymbol{\alpha}_i\| &= \frac{1}{\sqrt{m\lambda_i}}, \quad i = 1, \dots, D. \end{aligned} \quad (5.2.11)$$

Thus, the eigenvectors of \mathbf{K} can be normalized by

$$\tilde{\boldsymbol{\alpha}}_i = \frac{1}{\sqrt{m\lambda_i}} \boldsymbol{\alpha}_i = \frac{1}{\sqrt{\tilde{\lambda}_i}} \boldsymbol{\alpha}_i. \quad (5.2.12)$$

As was the case with the eigen-decomposition equation for \mathbf{C} , Eq. 5.2.6, if the eigen-decomposition equation for \mathbf{K} , Eq. 5.2.10, can be solved for the $\tilde{\lambda}_i$ and $\boldsymbol{\alpha}_i$, the feature-space PCA projection of any data-space vector, \mathbf{x} (i.e., any library data vector or new measurement data vector), onto any eigenvector, \mathbf{v}_i , is given by

$$z_i(\mathbf{x}) = \mathbf{v}_i^T \phi(\mathbf{x}) \quad [\text{Eq. 5.2.7}]$$

$$\begin{aligned}
&= [\Phi \alpha_i]^T \phi(\mathbf{x}) \quad [\text{sub: Eq. 5.2.9}] \\
&= \alpha_i^T \Phi^T \phi(\mathbf{x}) \\
\Rightarrow z_i(\mathbf{x}) &= \sum_{j=1}^m \alpha_{ij} \phi(\mathbf{x}_j)^T \phi(\mathbf{x}), \quad i = 1, \dots, D. \quad (5.2.13)
\end{aligned}$$

Hence, we have shown that an eigen-decomposition of a Gram matrix, \mathbf{K} , is all that is necessary to perform transformations from the original data space, to a higher-dimensional ($D > n$) variance-maximized feature space. However, the mapping functional, $\phi(\cdot)$, has still not been explicitly defined. Fortunately, since both the eigen-decomposition equation, Eq. 5.2.10, and the vector projection equation, Eq. 5.2.13, are now expressed in terms of inner products, instead of explicitly defining the mapping functional itself, we can simply define a function that describes inner products in feature space,

$$\phi(\cdot)^T \phi(\cdot) \equiv k(\cdot, \cdot),$$

called a “kernel function”. This is commonly referred to as the “kernel trick”. The Gram matrix, \mathbf{K} , can then be constructed as a “kernel matrix” (or simply, a “kernel”), defining its elements as

$$K_{ij} = \phi(\mathbf{x}_i)^T \phi(\mathbf{x}_j) \equiv k(\mathbf{x}_i, \mathbf{x}_j). \quad (5.2.14)$$

Substituting this definition into Eq. 5.2.13, the Kernel principle component analysis (KPCA) projection of any data-space vector, \mathbf{x} (i.e., any library data vector or new measurement data vector), onto any feature-space eigenvector is given by

$$z_i(\mathbf{x}) = \mathbf{v}_i^T \phi(\mathbf{x}) = \sum_{j=1}^m \alpha_{ij} \phi(\mathbf{x}_j)^T \phi(\mathbf{x}) = \sum_{j=1}^m \alpha_{ij} k(\mathbf{x}_j, \mathbf{x}), \quad i = 1, \dots, D. \quad (5.2.15)$$

In this context, the kernel function must be a continuous function,

$$k : \mathbb{R}^n \times \mathbb{R}^n \rightarrow \mathbb{R}, \quad (5.2.16)$$

that is both symmetric,

$$k(\mathbf{x}_i, \mathbf{x}_j) = k(\mathbf{x}_j, \mathbf{x}_i), \quad \forall \mathbf{x}_i, \mathbf{x}_j \in \mathbb{R}^n, \quad (5.2.17)$$

and positive semidefinite,

$$\sum_{i=1}^N \sum_{j=1}^N k(\mathbf{x}_i, \mathbf{x}_j) \cdot c_i \cdot c_j \geq 0, \quad \forall N \in \mathbb{N}, \quad \forall \mathbf{x}_1, \dots, \mathbf{x}_N \in \mathbb{R}^n, \quad \forall c_1, \dots, c_N \in \mathbb{R}. \quad (5.2.18)$$

Since the template-matching techniques to be employed in this feature space are based on the Pearson product-moment cross-correlation coefficient, the correlation kernel function

$$k(\mathbf{x}_i, \mathbf{x}_j) = \exp \left[-\gamma (1 - r(\mathbf{x}_i, \mathbf{x}_j)) \right], \quad 0 < \gamma \in \mathbb{R}, \quad (5.2.19)$$

$$\text{where } r(\mathbf{x}_i, \mathbf{x}_j) = \frac{(\mathbf{x}_i - \bar{\mathbf{x}}_i)^T (\mathbf{x}_j - \bar{\mathbf{x}}_j)}{\|\mathbf{x}_i - \bar{\mathbf{x}}_i\| \|\mathbf{x}_j - \bar{\mathbf{x}}_j\|}$$

is the Pearson correlation between data-space vectors \mathbf{x}_i and \mathbf{x}_j , was the first kernel function chosen for investigation in this chapter. The second kernel function to be considered here, called the cosine kernel function,

$$k(\mathbf{x}_i, \mathbf{x}_j) = \frac{\mathbf{x}_i^T \mathbf{x}_j}{\|\mathbf{x}_i\| \|\mathbf{x}_j\|}, \quad (5.2.20)$$

is the cosine of the angle between the data-space vectors \mathbf{x}_i and \mathbf{x}_j , and was chosen because the Pearson correlation, $r(\mathbf{x}_i, \mathbf{x}_j)$, is simply the cosine kernel function applied to centered versions of \mathbf{x}_i and \mathbf{x}_j . Thus, although there are notable similarities, there are two interesting differences between the two kernel functions to be investigated in this work.

The first is that the correlation kernel function—due to its centering of the data-space vectors—is invariant to separate changes in vector location and separate positive changes in vector scale (i.e., it is *insensitive* to both positive scale variations and shifts in the data)

$$k(\mathbf{x}_i, \mathbf{x}_j) = k(a\mathbf{x}_i + b, c\mathbf{x}_j + d), \quad \forall b, d \in \mathbb{R}, \quad 0 < a, c \in \mathbb{R}, \quad (5.2.21)$$

while the cosine kernel function has only the scale-invariant property (i.e., it is *insensitive* to positive scale variations, but is *sensitive* to shifts in the data)

$$k(\mathbf{x}_i, \mathbf{x}_j) \neq k(a\mathbf{x}_i + b, c\mathbf{x}_j + d), \quad \forall b, d \in \mathbb{R}, \quad 0 < a, c \in \mathbb{R}$$

$$k(\mathbf{x}_i, \mathbf{x}_j) = k(a\mathbf{x}_i, c\mathbf{x}_j), \quad 0 < a, c \in \mathbb{R}. \quad (5.2.22)$$

The second interesting difference is that, in the case of the correlation kernel function, Eq. 5.2.19, the Pearson correlation, $r(\mathbf{x}_i, \mathbf{x}_j)$, is substituted into an exponential function with a positive, real-valued, adjustable constant, γ , while the cosine function itself, Eq. 5.2.20, is a kernel function. Fig. 5.2.1 shows how the correlation kernel function accentuates the differences between pairs of data-space vectors \mathbf{x}_i and \mathbf{x}_j by exponentially “penalizing” vector pairs (in terms of kernel function value) as the Pearson correlation between them decreases, and how increasing the value of the adjustable parameter, γ , increases the severity of this “penalty”.

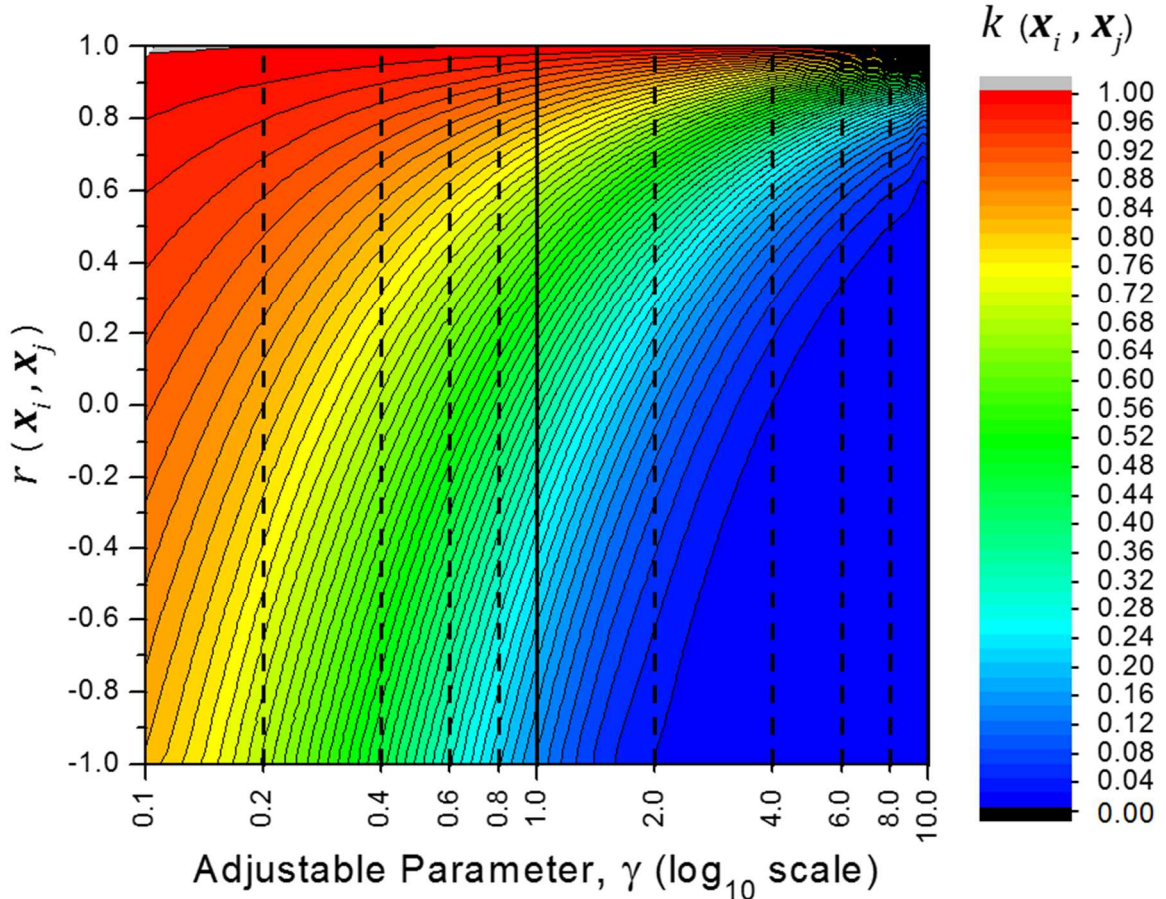


Figure 5.2.1. Contour plot of correlation kernel function values, Eq. 5.2.19, (linear color scale, RIGHT, with contour lines shown in increments of 0.02) as a function of Pearson correlation coefficient between vectors \mathbf{x}_i and \mathbf{x}_j (vertical axis, linear scale) and possible values for the adjustable parameter γ (horizontal axis, shown in \log_{10} scale for visual clarity).

Although the correlation kernel function centers vectors, \mathbf{x}_j , in data space, there is no guarantee (and it is actually extremely unlikely) that the corresponding transformed vectors, $\phi(\mathbf{x}_j)$, will be centered in feature space, regardless of the kernel function used. Recall that the feature-space vectors, $\phi(\mathbf{x}_j)$, were assumed to be centered at the outset of this derivation. Since we now know that this assumption, at best, cannot be guaranteed, let us consider centering the feature space vectors, in light of the KPCA concepts derived thus far, by subtracting the mean

$$\tilde{\phi}(\mathbf{x}_j) = \phi(\mathbf{x}_j) - \frac{1}{m} \sum_{k=1}^m \phi(\mathbf{x}_k) . \quad (5.2.23)$$

Substituting this expression for centered feature-space vectors into the definition of the Kernel matrix elements (i.e., inner products of feature-space vectors), we have

$$\begin{aligned} \tilde{K}_{ij} &= \tilde{\phi}(\mathbf{x}_i)^T \tilde{\phi}(\mathbf{x}_j) = \left[\phi(\mathbf{x}_i) - \frac{1}{m} \sum_{l=1}^m \phi(\mathbf{x}_l) \right]^T \left[\phi(\mathbf{x}_j) - \frac{1}{m} \sum_{k=1}^m \phi(\mathbf{x}_k) \right] \\ &= \phi(\mathbf{x}_i)^T \phi(\mathbf{x}_j) - \frac{1}{m} \sum_{k=1}^m \phi(\mathbf{x}_i)^T \phi(\mathbf{x}_k) - \frac{1}{m} \sum_{k=1}^m \phi(\mathbf{x}_k)^T \phi(\mathbf{x}_j) \\ &\quad + \left(\frac{1}{m} \sum_{l=1}^m \phi(\mathbf{x}_l)^T \right) \left(\frac{1}{m} \sum_{k=1}^m \phi(\mathbf{x}_k) \right) \\ &= \phi(\mathbf{x}_i)^T \phi(\mathbf{x}_j) - \frac{1}{m} \sum_{k=1}^m \phi(\mathbf{x}_i)^T \phi(\mathbf{x}_k) - \frac{1}{m} \sum_{k=1}^m \phi(\mathbf{x}_j)^T \phi(\mathbf{x}_k) + \frac{1}{m^2} \sum_{l=1}^m \sum_{k=1}^m \phi(\mathbf{x}_l)^T \phi(\mathbf{x}_k) \\ &= k(\mathbf{x}_i, \mathbf{x}_j) - \frac{1}{m} \sum_{k=1}^m k(\mathbf{x}_i, \mathbf{x}_k) - \frac{1}{m} \sum_{k=1}^m k(\mathbf{x}_j, \mathbf{x}_k) + \frac{1}{m^2} \sum_{l=1}^m \sum_{k=1}^m k(\mathbf{x}_l, \mathbf{x}_k) \\ \Rightarrow \tilde{K}_{ij} &= K_{ij} - \frac{1}{m} \sum_{k=1}^m K_{ik} - \frac{1}{m} \sum_{k=1}^m K_{jk} + \frac{1}{m^2} \sum_{l=1}^m \sum_{k=1}^m K_{lk} . \end{aligned} \quad (5.2.24)$$

This expression can be written in matrix form as

$$\tilde{\mathbf{K}} = \mathbf{K} - \mathbf{1}_{1/m} \mathbf{K} - \mathbf{K} \mathbf{1}_{1/m} + \mathbf{1}_{1/m} \mathbf{K} \mathbf{1}_{1/m} , \quad (5.2.25)$$

where $\mathbf{1}_{1/m}$ is an $m \times m$ matrix with values of $1/m$ for all elements. Thus, any kernel matrix, \mathbf{K} , constructed using any symmetric positive semidefinite kernel function, $k(\mathbf{x}_i, \mathbf{x}_j)$, can be subsequently centered via application of Eq. 5.2.25, such that our initial assumption is satisfied.

5.2.2 KPCA template-matching algorithm

Having derived the necessary kernel principle component analysis concepts, we are now aptly equipped to introduce the algorithm for performing template-matching in a KPCA feature space. The description of this algorithm will be divided into two major sections: “preprocessing” and “real-time analysis”. As these names suggest, the preprocessing steps include all calculations that can be carried out prior to collecting new measurement data with the 6C spectrometer, and the real-time analysis steps include all calculations that must be carried out in real time as new instrument data is collected.

5.2.2.1 Preprocessing

Step 1: Define the library matrix, X , in the form of Eqs. 5.2.1 and 5.2.2.

In this chapter, we will consider two different library matrix definitions, which will be referred to as the “three-dimensional (3D) library matrix” and the “two-dimensional (2D) library matrix”. For the 3D library matrix, we begin by describing the response of the 6C spectrometer, in general, as a set of 128 (one for each thermal neutron detector in the instrument) 3-dimensional discretized measurements, for which the information provided by each neutron detector is described by its neutron detection intensity as a function of its Cartesian coordinate positions within the instrument (Fig. 5.2.1, LEFT),

$$I(\tilde{x}_a, \tilde{y}_b, \tilde{z}_c), \quad a = 1, \dots, 8, \quad b = 1, \dots, 4, \quad c = 1, \dots, 4. \quad (5.2.26)$$

The discrete coordinate positions are then enumerated,

$$r_i = (\tilde{x}_a, \tilde{y}_b, \tilde{z}_c), \quad i = 1, \dots, 128 (= 8 \cdot 4 \cdot 4), \quad (5.2.27)$$

such that

$$x_i \equiv I(r_i), \quad i = 1, \dots, 128, \quad (5.2.28)$$

represents the neutron detection intensities for each detector position, and the 3D instrument response is described by the single vector

$$\mathbf{x} \equiv [x_1, \dots, x_{128}]^T = [I(r_1), \dots, I(r_{128})]^T \quad (5.2.29)$$

in a 128-dimensional data space, \mathbb{R}^{128} . The example 3D library data set used in this work contains $m = 360$ of these 128-dimensional vectors, representing expected instrument responses to five different unshielded neutron source types (^{252}Cf , AmBe, PuBe, Pu metal, and PuO_2) located at 72 different discretized source-to-instrument angular orientations in the horizontal plane (0° to 355° in 5° increments; $m = 360$ library vectors = 5 source types of interest \times 72 discretized angular orientations, library data sets were generated as described in section 4.4). Then, in the form of Eqs. 5.2.1 and 5.2.2, each 3D data-space library vector is denoted

$$\mathbf{x}_j = [x_{1,j}, \dots, x_{128,j}]^T, \quad j = 1, \dots, 360, \quad (5.2.30)$$

where $i = 1, \dots, 128$ enumerates the detector positions, $j = 1, \dots, 360$ enumerates the library source types/angular orientations, and each x_{ij} ($\in \mathbb{R}$) is the expected relative neutron detection intensity of the detector located at position i from library source type/angular orientation j . Thus, the entire library of instrument responses is represented by the 128×360 “3D library matrix”

$$\mathbf{X}_{128 \times 360} = [\mathbf{x}_1, \dots, \mathbf{x}_{360}] = \begin{bmatrix} x_{1,1} & \cdots & x_{1,360} \\ \vdots & \ddots & \vdots \\ x_{128,1} & \cdots & x_{128,360} \end{bmatrix}. \quad (5.2.31)$$

Since, in this chapter, we are concerned with determining the angular location of neutron sources in the horizontal plane only, for the 2D library matrix, we begin by describing the response of the 6C spectrometer in the two horizontal-planar dimensions only

(i.e., the \tilde{x} and \tilde{z} dimensions in the coordinate system defined in Fig. 5.2.1) by summing the detection intensities of all neutron detectors that are aligned vertically (Fig. 5.2.1, RIGHT),

$$I(\tilde{x}_a, \tilde{z}_c) = \sum_{b=1}^4 I(\tilde{x}_a, \tilde{y}_b, \tilde{z}_c), \quad a = 1, \dots, 8, \quad c = 1, \dots, 4. \quad (5.2.32)$$

Note: Fig. 5.2.1 is the same as Fig. 4.4.1, but it was relabeled and included in this section for notational clarity. Similarly, the discrete coordinate positions are then enumerated

$$r_i = (\tilde{x}_a, \tilde{z}_c), \quad i = 1, \dots, 32 (= 8 \cdot 4), \quad (5.2.33)$$

such that

$$x_i \equiv I(r_i), \quad i = 1, \dots, 32, \quad (5.2.34)$$

represents the neutron detection intensities for each horizontal-planar detector position, and the 2D instrument response is described by the single vector

$$\mathbf{x} \equiv [x_1, \dots, x_{32}]^T = [I(r_1), \dots, I(r_{32})]^T \quad (5.2.35)$$

in a 32-dimensional data space, \mathbb{R}^{32} . The 2D library data set used in this chapter also contains $m = 360$ of these 32-dimensional vectors, representing expected 2D instrument responses to the same five neutron source types, located at the same 72 discretized source-to-instrument angular orientations in the horizontal plane. Then, in the form of Eqs. 5.2.1 and 5.2.2, each 2D data-space library vector is denoted

$$\mathbf{x}_j = [x_{1,j}, \dots, x_{32,j}]^T, \quad j = 1, \dots, 360, \quad (5.2.36)$$

where $i = 1, \dots, 32$ enumerates the unique horizontal-planar detector positions, $j = 1, \dots, 360$ enumerates the library source types/angular orientations, and each x_{ij} ($\in \mathbb{R}$) is the sum of the expected neutron detection intensities of detectors located at horizontal-planar position i , from library source type/angular orientation j . Thus, the entire library of instrument responses is represented by the 32×360 “2D library matrix”

$$\mathbf{X}_{32 \times 360} = [\mathbf{x}_1, \dots, \mathbf{x}_{360}] = \begin{bmatrix} x_{1,1} & \cdots & x_{1,360} \\ \vdots & \ddots & \vdots \\ x_{32,1} & \cdots & x_{32,360} \end{bmatrix}. \quad (5.2.37)$$

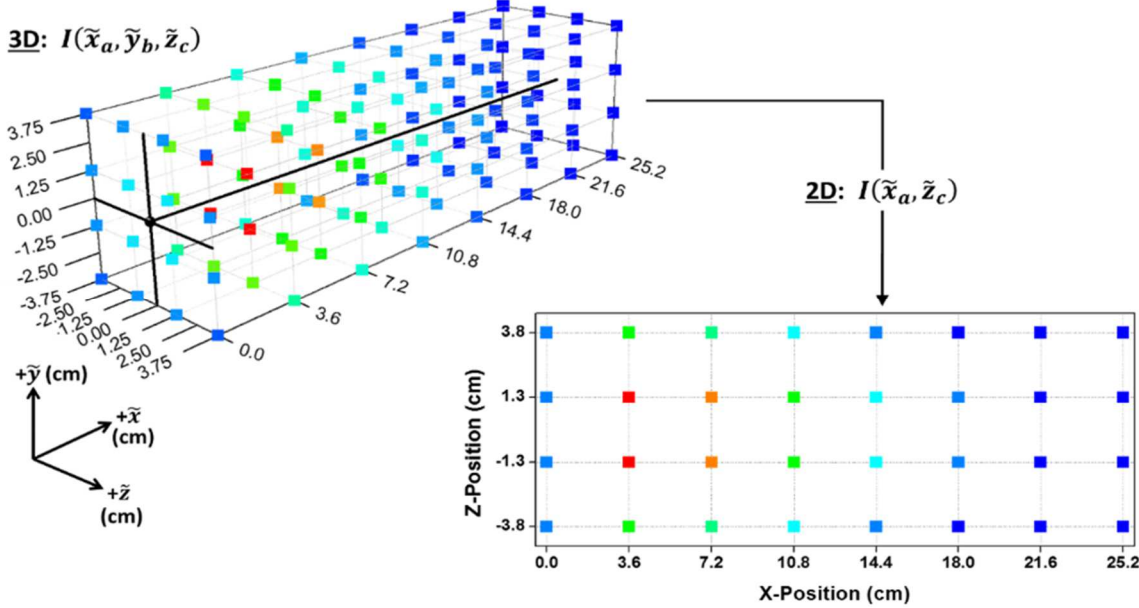


Figure 5.2.2. Example illustration of 3D (LEFT) and 2D (RIGHT) descriptions of a typical 6C spectrometer response, showing the 3D and 2D library instrument responses to an unshielded ^{252}Cf neutron source at a source-to-instrument angular orientation of 0° in the horizontal plane (i.e., source located at $[-100 \text{ cm}, 0 \text{ cm}, 0 \text{ cm}]$ in the coordinate system defined in the figure).

The remaining steps of the KPCA template-matching algorithm are applicable using either the 3D or 2D definition of the library matrix. The number of data-space library vectors, $m = 360$, is same for the 3D and 2D definitions, but the number of data-space coordinate positions is $n = 128$ for the 3D definition and $n = 32$ for the 2D definition.

Step 2: Choose a kernel function, $k(\mathbf{x}_i, \mathbf{x}_j)$, and construct the kernel matrix, \mathbf{K} , by applying Eq. 5.2.14 to the library matrix, $\mathbf{X} = [\mathbf{x}_1, \dots, \mathbf{x}_m]$ (for $i = 1, \dots, m$ and $j = 1, \dots, m$).

In this chapter, we will test and compare the efficacy of four different kernel matrices, constructed through application of both the correlation kernel function, Eq. 5.2.19, and the cosine kernel function, Eq. 5.2.20, to both the 3D and 2D library matrices, as defined in Step 1. These kernel matrices will be referred to as the 3D-Correlation kernel matrix, 3D-Cosine kernel matrix, 2D-Correlation kernel matrix, and 2D-Cosine kernel matrix. The KPCA template-matching algorithm, as defined in this section, employing each of these kernel matrices will be referred to as the 3D-Correlation KPCA algorithm, 3D-Cosine KPCA algorithm, 2D-Correlation KPCA algorithm, and 2D-Cosine KPCA algorithm.

Step 3: Apply Eq. 5.2.25 to center the kernel matrix.

Step 4: Solve the feature-space eigen-decomposition equation, Eq. 5.2.10, for the centered kernel matrix to find the feature-space eigenvectors, α_i , and their corresponding eigenvalues, $\tilde{\lambda}_i$.

$$\tilde{K}\alpha_i = \tilde{\lambda}_i\alpha_i, \quad i = 1, \dots, m, \quad (5.2.38)$$

where \tilde{K} represents the centered kernel matrix obtained from step 3.

Note: for all four cases tested herein, the Python routine “eigh” from the Numpy linear algebra package “linalg” [37, 45] was used to perform this eigen-decomposition step.

Step 5: Find and remove any feature-space eigenvectors that correspond to zero (or negligibly small) eigenvalues (i.e., if $\tilde{\lambda}_i = 0$, or $\tilde{\lambda}_i \cong 0$, for any i , remove the corresponding α_i).

Although this is an important step in kernel principle component analysis in general, and is thus included in this algorithm description, there did not happen to be any zero (or negligibly small) eigenvalues for any of the four kernel matrices tested in this chapter. Hence, all m eigenvectors were included in the analysis for each case.

Step 6: Normalize all remaining feature-space eigenvectors using Eq. 5.2.12,

$$\tilde{\alpha}_i = \frac{1}{\sqrt{\lambda_i}} \alpha_i, \quad i = 1, \dots, m. \quad (5.2.39)$$

Here, D (the dimension of the KPCA feature space) in Eq. 5.2.12 has been replaced by m , since all m eigenvectors were included in the analysis for each case tested in this work. However, if any zero (or negligibly small) eigenvalues had been found in Step 5, the corresponding eigenvectors would have been removed, such that the feature space dimension, $D (< m)$, would have been the number of eigenvectors remaining after Step 5.

Step 7: Sort the normalized feature-space eigenvectors, according to their corresponding eigenvalues, in descending order.

Step 8 (projection of library data into feature space): Employ Eq. 5.2.15, to project each of the data-space library vectors, \mathbf{x}_k , onto each of the sorted, normalized, feature-space eigenvectors, $\tilde{\alpha}_i$.

$$z_i(\mathbf{x}_k) = \sum_{j=1}^m \tilde{\alpha}_{ij} k(\mathbf{x}_j, \mathbf{x}_k), \quad i = 1, \dots, m, \quad k = 1, \dots, m \quad (5.2.40)$$

Here, the eigenvector elements, α_{ij} , in Eq. 5.2.15 have been replaced by the normalized elements, $\tilde{\alpha}_{ij}$, obtained from Step 6, $k(\cdot, \cdot)$ is the kernel function chosen in Step 2, and the single generalized data-space vector, \mathbf{x} , in Eq. 5.2.15 has been replaced by \mathbf{x}_k (for $k = 1, \dots, m$), because we desire a projection of each of the m data-space library vectors onto each of the m feature-space eigenvectors. The vectors

$$\mathbf{z}_k \equiv [z_1(\mathbf{x}_k), \dots, z_m(\mathbf{x}_k)]^T, \quad k = 1, \dots, m, \quad (5.2.41)$$

obtained from Eq. 5.2.40, are the new m -dimensional feature-space library vectors, and

$$\mathbf{Z}_{m \times m} \equiv [\mathbf{z}_1, \dots, \mathbf{z}_m] = \begin{bmatrix} z_1(\mathbf{x}_1) & \cdots & z_1(\mathbf{x}_m) \\ \vdots & \ddots & \vdots \\ z_m(\mathbf{x}_1) & \cdots & z_m(\mathbf{x}_m) \end{bmatrix} \quad (5.2.42)$$

is the new $m \times m$ feature-space library matrix, to be used in our feature-space template-matching analysis. Again, if any zero (or negligibly small) eigenvalues were found in Step 5, the feature space would be D -dimensional instead of m -dimensional ($D < m$), such that Eq. 5.2.40 would be applied for $i = 1, \dots, D$, each \mathbf{z}_k would have D entries, and \mathbf{Z} would be a $D \times m$ matrix. Recall that each (m - or D -dimensional) feature-space library vector, \mathbf{z}_k , corresponds to a particular neutron source type that is located at a particular horizontal-planar angular orientation relative to the instrument, and m is the total number of source type/angular orientation combinations represented in the feature-space library matrix, \mathbf{Z} . Thus, for this template-matching application, it is critical to keep track of which template source types/angular orientations correspond to which library vector indices throughout the algorithm's implementation. Note: Although there are many different methods for recording and tracking this information, since the algorithm was implemented in Python for this work, the built-in "dictionary" data structure was an obvious and convenient choice for this bookkeeping task.

5.2.2.2 Real-time analysis

Step 0: Apply Eqs. 5.2.26-5.2.29 to live 6C spectrometer measurement data to generate a 3D data-space measurement vector, and/or apply Eqs. 5.2.32-5.2.35 to generate a 2D data-space measurement vector.

Step 1 (projection of measurement data into feature space): Employ Eq. 5.2.15, to project the data-space measurement vector, \mathbf{x} , onto each of the sorted, normalized, feature-space eigenvectors, $\tilde{\alpha}_i$.

$$z_i(\mathbf{x}) = \sum_{j=1}^m \tilde{\alpha}_{ij} k(\mathbf{x}_j, \mathbf{x}), \quad i = 1, \dots, m \quad (5.2.43)$$

Here, the feature-space eigenvector elements, α_{ij} , in Eq. 5.2.15 have been replaced by the normalized elements, $\tilde{\alpha}_{ij}$, obtained from Preprocessing Step 6, $k(\cdot, \cdot)$ is the kernel function chosen in Preprocessing Step 2, and \mathbf{x} , which represented any general data-space vector in Eq. 5.2.15, now represents the data-space measurement vector obtained from Step 0. The vector

$$\mathbf{z} \equiv [z_1(\mathbf{x}), \dots, z_m(\mathbf{x})]^T \quad (5.2.44)$$

obtained from Eq. 5.2.43, is the new m -dimensional (D -dimensional if any zero, or negligibly small, eigenvalues are found in Preprocessing Step 5) feature-space measurement vector to be used in our feature-space template-matching analysis.

Step 2 (template-matching in feature space): Calculate the normalized Pearson product-moment cross-correlation coefficient, r_k , between the feature-space measurement vector, \mathbf{z} , and each feature-space library vector, \mathbf{z}_k .

$$r_k = \frac{1}{m} \sum_{i=1}^m \frac{z_i(\mathbf{x}) - \bar{z}}{\sigma_z} \cdot \frac{z_i(\mathbf{x}_k) - \bar{z}_k}{\sigma_{z_k}}, \quad k = 1, \dots, m, \quad (5.2.45)$$

where \bar{z} and σ_z are the average and standard deviation, respectively, of the elements of \mathbf{z} , and \bar{z}_k and σ_{z_k} are the average and standard deviation, respectively, of the elements of \mathbf{z}_k .

Step 3 (template-matching in feature space): Calculate the coefficient of determination, d_k , between the feature-space measurement vector, \mathbf{z} , and each feature-space library vector, \mathbf{z}_k .

If $r_k \geq 0$, calculate the coefficient of determination as

$$d_k \equiv r_k^2, \quad k = 1, \dots, m, \quad (5.2.46)$$

and if $r_k < 0$, calculate the coefficient of determination as

$$d_k \equiv -(r_k^2), \quad k = 1, \dots, m. \quad (5.2.47)$$

Step 4 (template-matching in feature space): Identify the source type/angular orientation that corresponds to the largest d_k value calculated in Step 3.

The source type/horizontal-planar angular orientation corresponding to the largest coefficient of determination is chosen as the most likely origin of the neutron radiation incident on the 6C spectrometer (of those represented in the library). Since the “preprocessing” steps, Eqs. 5.2.26-5.2.42, are performed before any measurements are taken, and the “real-time analysis steps” in this section, Eqs. 5.2.43-5.2.47, are few and computationally inexpensive, the neutron source location and identity information provided by this analysis can be deduced and displayed to the instrument’s user in real-time updates as new measurement data is accumulated.

5.3 Simulation testing and comparison of KPCA template-matching algorithms

5.3.1 Description of simulation tests

To assess the theoretical efficacy of the kernel PCA template-matching algorithms detailed in section 5.2, a set of MCNP6 simulations were conducted, in which a detailed model of the 6C spectrometer (Fig. 5.3.1A) was exposed to neutron radiation from five different unshielded source types— ^{252}Cf , AmBe, PuBe, Pu metal, and PuO₂ (each neutron energy spectrum was obtained from [18])—located at 72 different horizontal-planar angular orientations—0° to 355° in 5° increments (as defined in Fig. 5.3.1B)—relative to the instrument model (5 source types × 72 angular orientations = 360 MCNP6 simulations total). The 3D-Correlation, 3D-Cosine, 2D-Correlation, and 2D-Cosine KPCA template-matching algorithms were each applied to all simulated instrument measurements to determine both the angular location and identity of the neutron source in each case.

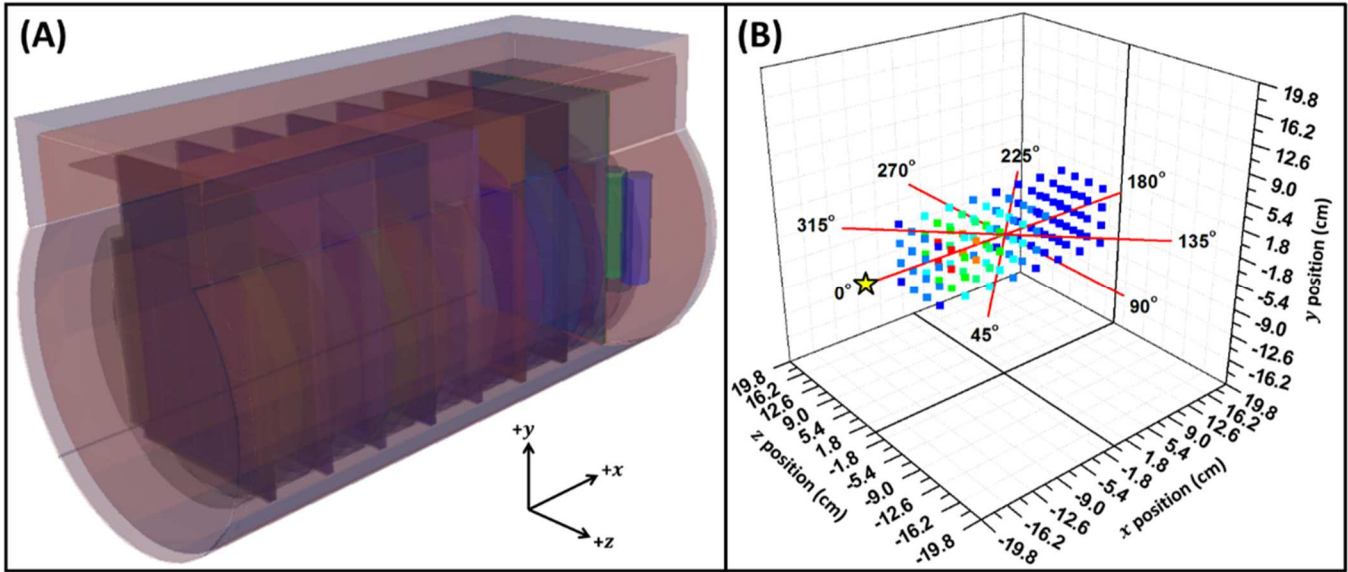


Figure 5.3.1. Simulation test illustrations. **(A)** Detailed MCNP model of the 6C neutron spectrometer. **(B)** Example of a simulated 6C spectrometer response—neutron detector count intensity (color code, red = highest intensity → dark blue = lowest intensity) as a function of physical position within the cylindrical moderator volume—to a bare ^{252}Cf spontaneous fission neutron source located at an angular orientation of 0° in the horizontal x - z -plane (indicated by a yellow star). Angular orientations of 0° to 315° in 45° increments are shown to illustrate the way in which neutron source horizontal-planar angular locations are defined in this chapter, relative to midpoint of the 6C spectrometer’s central axis.

5.3.2 Simulation test results and analysis

Figs. 5.3.2, 5.3.3, 5.3.4, and 5.3.5 show the test results for the 3D-Correlation, 3D-Cosine, 2D-Correlation, and 2D-Cosine KPCA template-matching algorithms, respectively. In each plot, the neutron source type simulated is indicated by the plot title (in blue), the source-to-spectrometer horizontal-planar angular orientation simulated is labeled “True Angle” (horizontal axis), the angular orientation determined by the KPCA template-matching algorithm is labeled “Measured Angle” (vertical axis), correct source type identifications are represented by blue data points, and incorrect source identifications are represented by red data points, with red data labels indicating the misidentified source type. Two additional

quantities are given in the legend of each figure, the average angular error and the average ID error. The average angular error (absolute) for each plot is calculated as

$$\frac{1}{72} \sum_{i=1}^{72} \min \left(\theta_i^T - \theta_i^M + 360 \pmod{360}, \theta_i^M - \theta_i^T + 360 \pmod{360} \right), \quad (5.3.1)$$

where $i = 1, \dots, 72$ enumerates the simulation results represented in each plot, each θ_i^T is the “true angle” (in degrees) in simulation i , and each θ_i^M is the “measured angle” (in degrees) from applying the KPCA template-matching algorithm to the instrument count data obtained from simulation i . The average ID (source type identification) error is calculated as

$$\frac{1}{72} \sum_{i=1}^{72} \varepsilon_i, \quad (5.3.2)$$

where each ε_i is equal to zero if the neutron source type was correctly identified by the KPCA template-matching algorithm for simulation i , and is equal to one if the neutron source type was not correctly identified for simulation i .

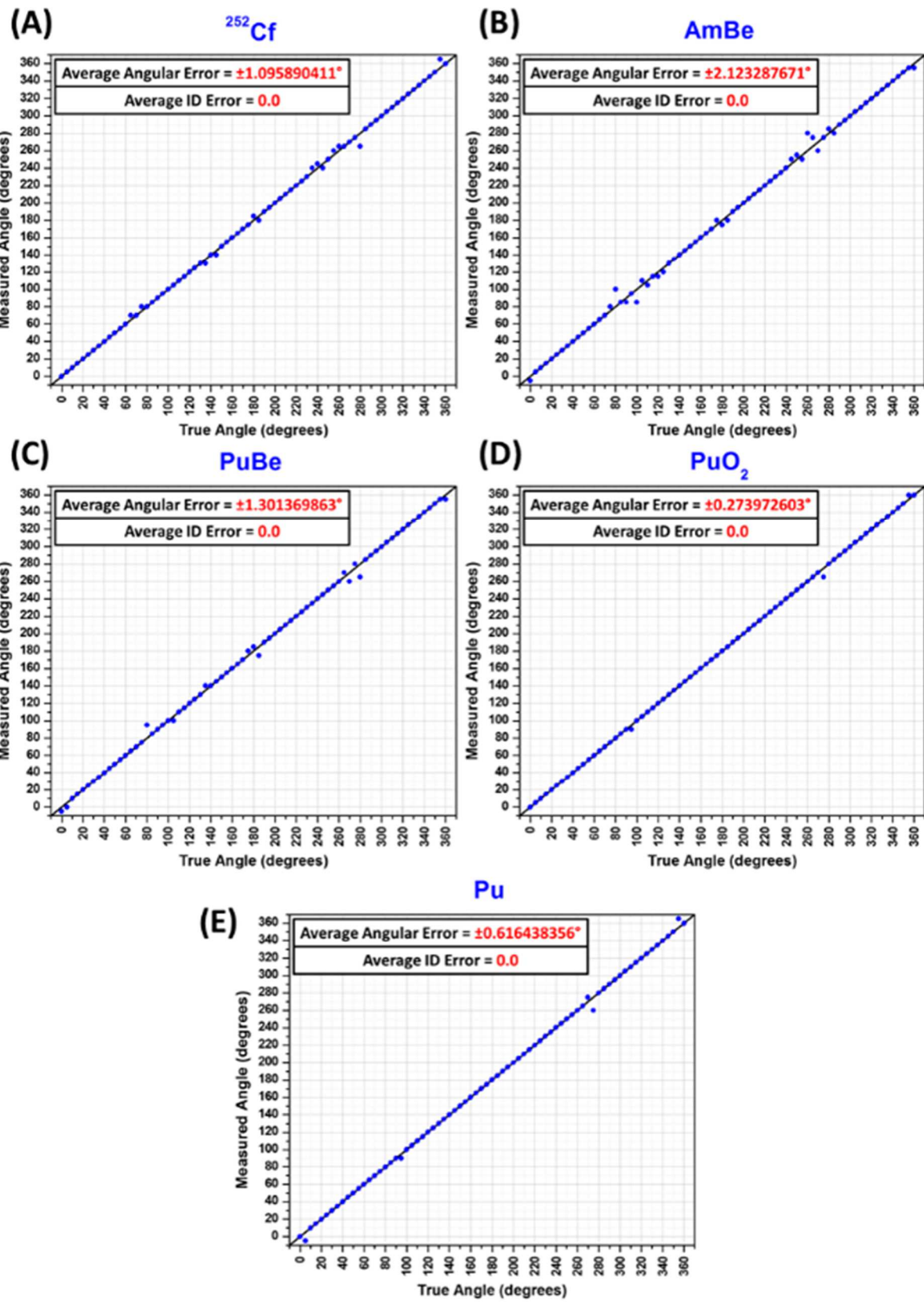


Figure 5.3.2. 3D Correlation KPCA template-matching algorithm simulation test results for five unshielded source types: (A) ^{252}Cf , (B) AmBe, (C) PuBe, (D) PuO₂, and (E) Pu metal (each neutron energy spectrum simulated was obtained from [18]).

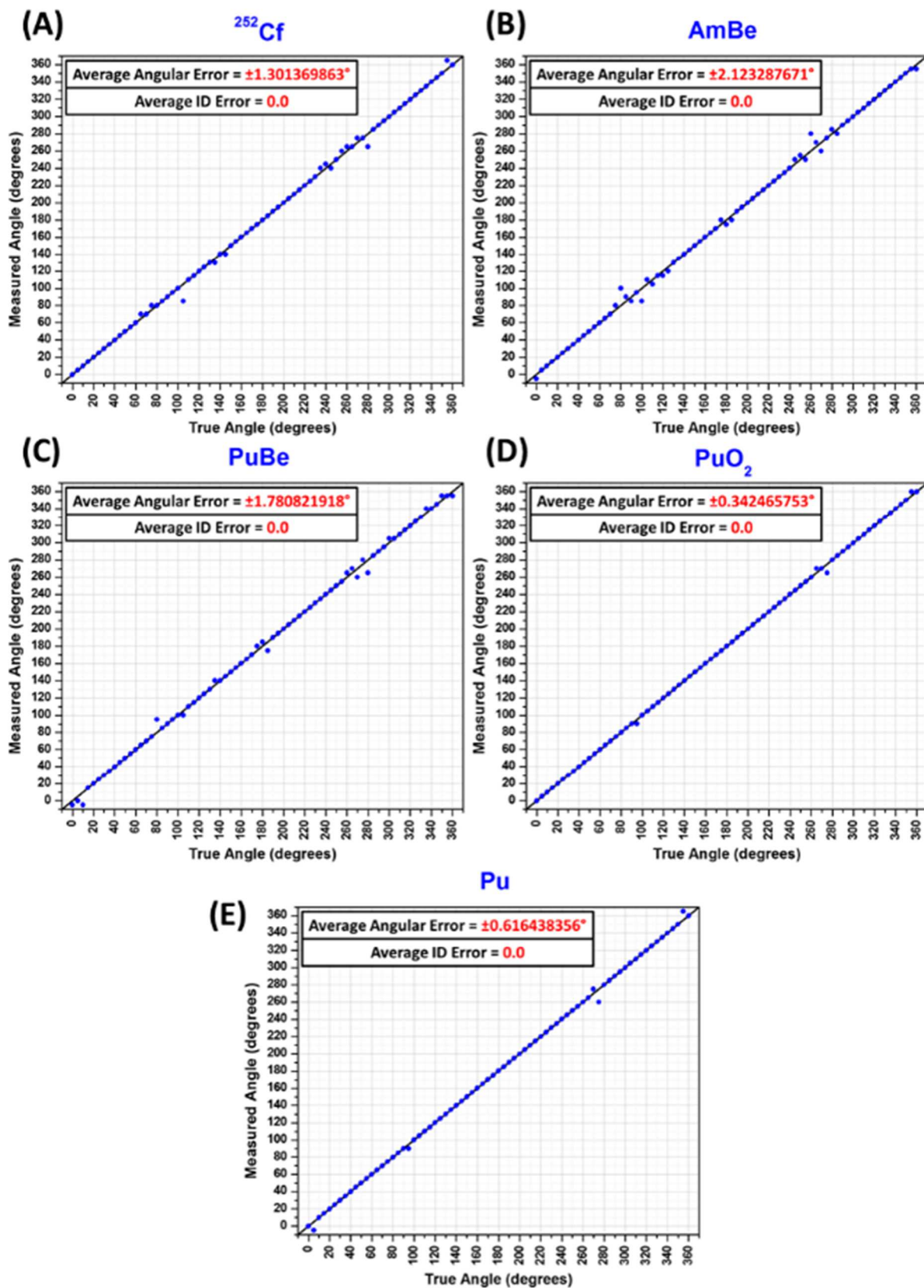


Figure 5.3.3. 3D Cosine KPCA template-matching algorithm simulation test results for five unshielded source types: (A) ^{252}Cf , (B) AmBe, (C) PuBe, (D) PuO₂, and (E) Pu metal.

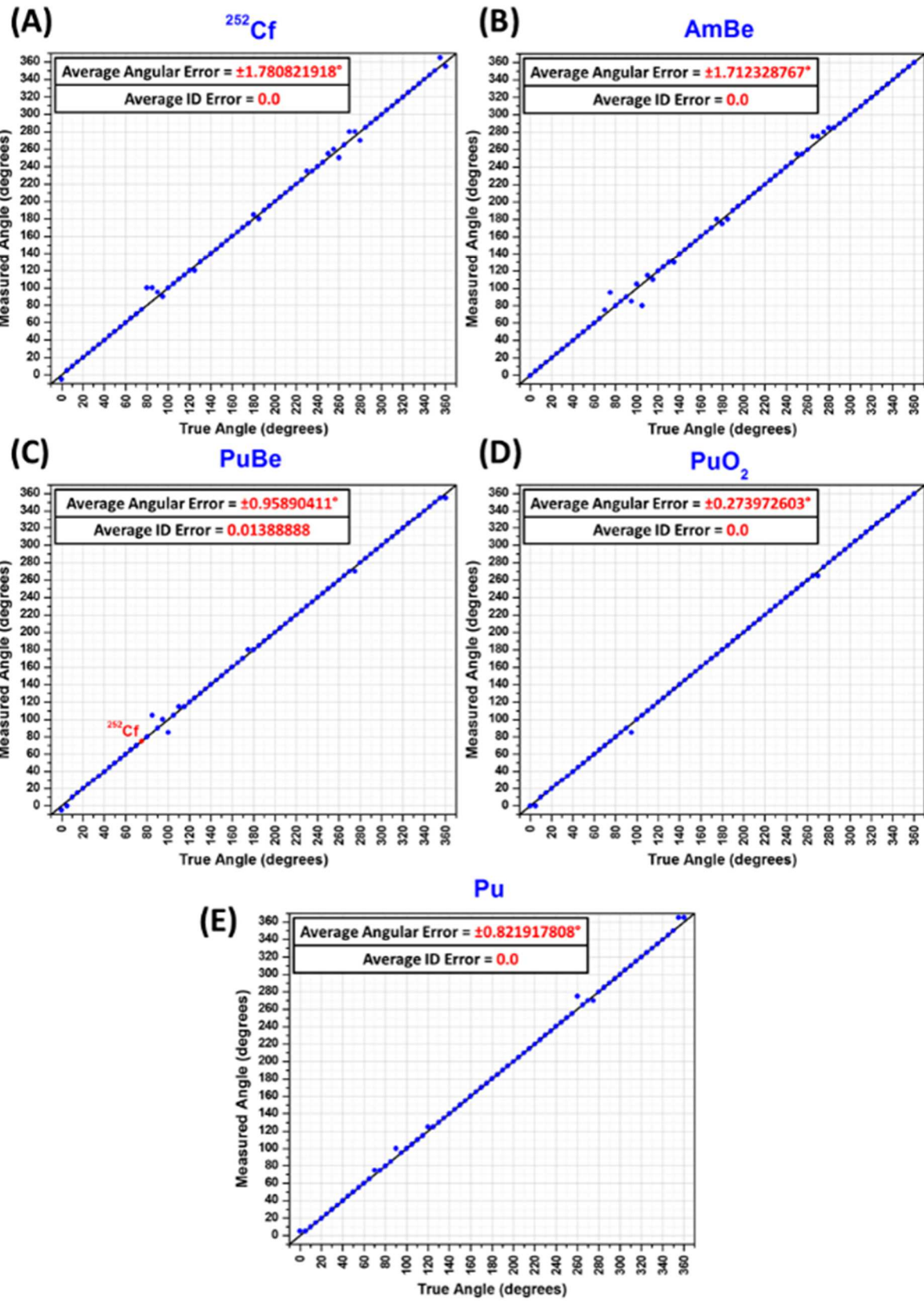


Figure 5.3.4. 2D Correlation KPCA template-matching algorithm simulation test results for five unshielded source types: (A) ^{252}Cf , (B) AmBe, (C) PuBe, (D) PuO₂, and (E) Pu metal.

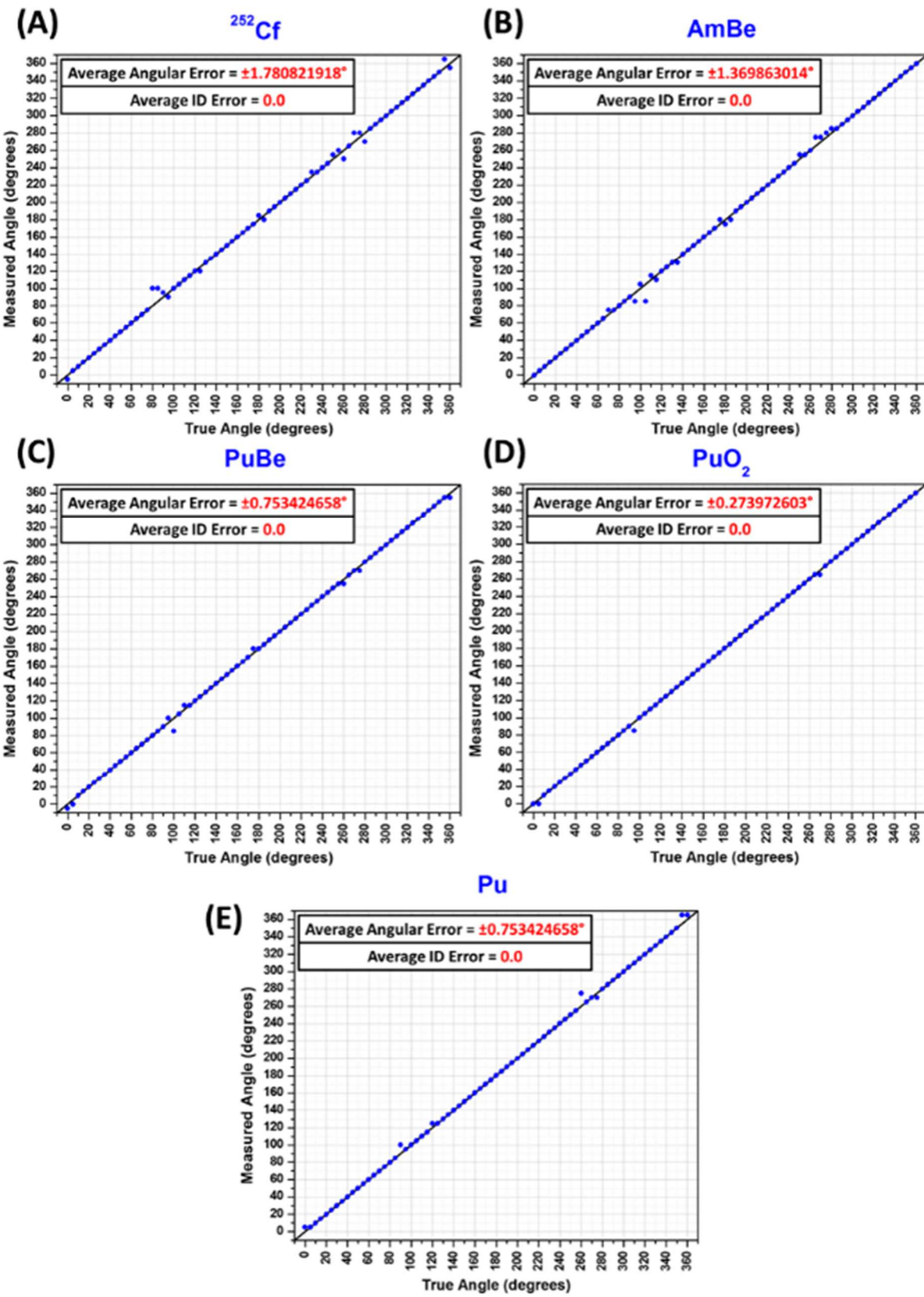


Figure 5.3.5. 2D Cosine KPCA template-matching algorithm simulation test results for five unshielded source types: (A) ^{252}Cf , (B) AmBe, (C) PuBe, (D) PuO₂, and (E) Pu metal.

The simulation test results shown in Figs. 5.3.2-5.3.5 show that each of the KPCA template-matching algorithm variants performed quite well. For each method variant and each neutron source type tested, the average error in determining the angular source location in the horizontal plane was less than $\pm 2.2^\circ$, and the true neutron source was correctly identified in all but one of the 1440 method tests (72 angular orientations \times 5 source types \times 4 algorithm variants = 1440 tests total); using the 2D Correlation KPCA template-matching algorithm, a PuBe source simulated at a 75° angular orientation was misidentified as a ^{252}Cf source at a 75° angular orientation. Further inspection of the angular orientation results reveals that individual angular errors most frequently occur near true angles of 0° , 90° , 180° , and 270° . These angular source positions each lie on symmetry axes of the instrument's cylindrical moderator volume (i.e., 0° and 180° lie on the x axis and 90° and 180° lie on z axis, Fig. 5.3.1), and many of the thermal neutron detectors within this volume share common coordinate positions with respect to these symmetry axes (i.e., in the coordinate system defined in Fig. 5.3.1, there are 8 unique x-axial coordinate positions, each shared by 16 detectors, and there are 4 unique z-axial positions, each shared by 32 detectors). When a neutron source is aligned with one of these axes, several of the detectors that share common coordinate positions along this axis have similar moderator penetration depths (on average), and thus provide very similar neutron thermalization information. Since the instrument's detectors provide less unique information near these orientations, 6C measurements (as well as response libraries) are more similar to one another near these angles, making them the most difficult to distinguish regardless of the method applied.

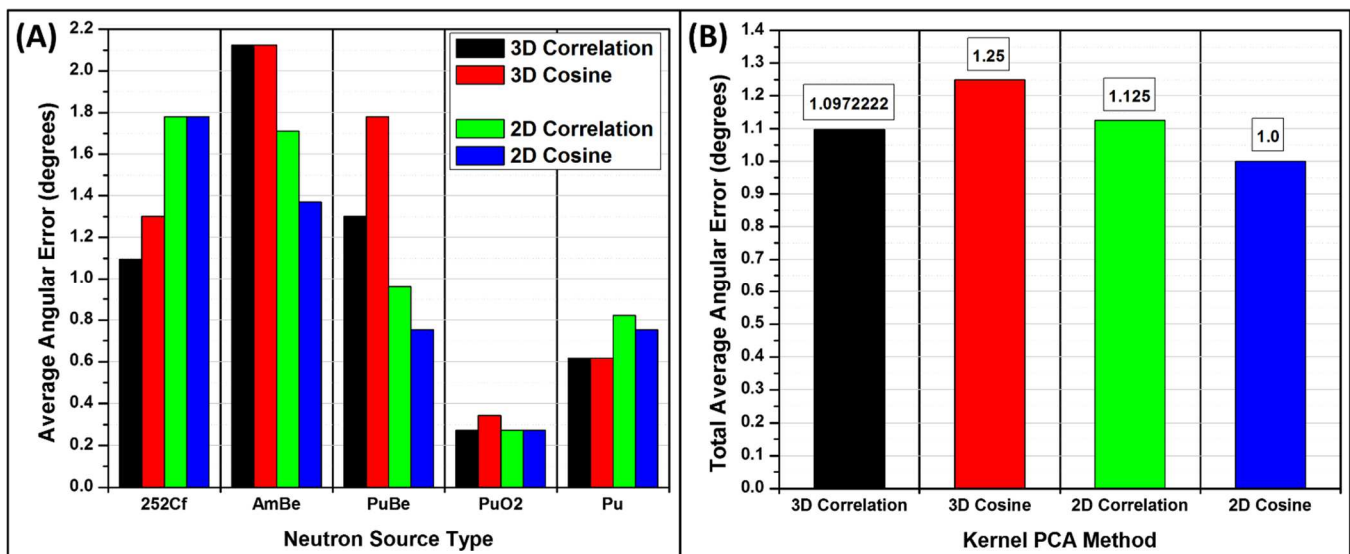


Figure 5.3.6. Summary plots of KPCA template-matching algorithm simulation test results, showing **(A)** average angular error, Eq. 5.3.1, as a function of both neutron source type simulated and method variant applied, and **(B)** total average angular error, Eq. 5.3.3, as a function of applied method variant.

The two plots in Fig. 5.3.6 provide a summary of the simulation test results detailed in Figs. 5.3.2-5.3.5. Fig. 5.3.6A is a visual representation of the average angular errors, Eq. 5.3.1, that were given numerically in the legend of each plot of Figs. 5.3.2-5.3.5. From this figure, we can immediately see that each of the method variants were able to determine the horizontal-planar angular location of the PuO₂ neutron source with the highest degree of accuracy (i.e., lowest average angular error). This is because the discretized PuO₂ neutron energy spectrum used in these simulations has the lowest peak neutron kinetic energy range (i.e., bin), 0.501 – 0.630 MeV (Fig. 5.3.7, [18]), of the five source types tested; thus, neutrons from this source have the smallest average moderator penetration depth for sufficient thermalization, such that they are most likely to be detected by the instrument's thermal neutron detectors that are located closest to surface of the moderating cylinder. This property of the 6C spectrometer's response to lower-energy neutron radiation results in angular-

orientation-dependent library responses that are more easily separable for PuO₂ than the other source types tested. This effect is also seen, to a lesser extent, in the Pu metal, 1.00 – 1.25 MeV peak energy (Fig. 5.3.7, [18]), angular-orientation-dependent library responses; however, free neutrons emitted from the other three higher-energy source types—the discretized ²⁵²Cf, PuBe, and AmBe neutron spectra have peak energy ranges of 1.99 – 2.51 MeV, 3.16 – 3.98 MeV, and 3.98 – 5.01 MeV respectively (Fig. 5.3.7, [18])—are most likely to be detected by thermal neutron detectors that are closer to the central axis (i.e., further from the surface) of the moderating cylinder, making their angular-orientation-dependent library responses more difficult to discern.

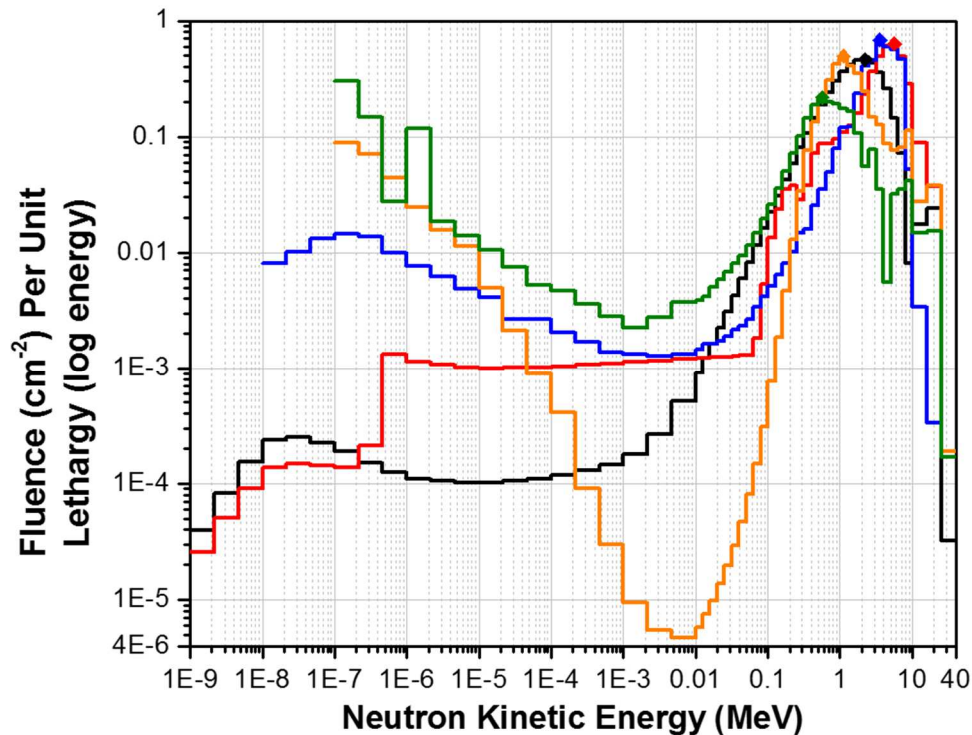


Figure 5.3.7. Plot of the simulated neutron energy spectra [18] for ²⁵²Cf (black), AmBe (red), PuBe (blue), Pu Metal (orange), and PuO₂ (green), showing fluence (cm^{-2}) per unit lethargy (\log_{10} energy) vs. neutron kinetic energy (MeV). The peak energy range for each spectrum is indicated by a diamond, filled with the spectrum's associated color.

Another noteworthy observation from Fig. 5.3.6A is that, while the four method variants performed comparably well for determining horizontal-planar angular orientations of the PuO₂ neutron source, the 3D methods outperformed the 2D methods for the other two spontaneous fission neutron sources (the 3D-Correlation method performed best for ²⁵²Cf, and the 3D-Correlation and 3D-Cosine methods tied for best performance for Pu metal) and the 2D methods outperformed the 3D methods for the two (α, n) neutron sources (the 2D-Cosine method performed best for both AmBe and PuBe). The “total average angular error”, shown Fig. 5.3.6B for each method variant, is a measure of angular orientation determination performance over all sources tested; this metric is given by

$$\frac{1}{360} \sum_{i=1}^{360} \min \left(\theta_i^T - \theta_i^M + 360 \pmod{360}, \theta_i^M - \theta_i^T + 360 \pmod{360} \right), \quad (5.3.3)$$

where $i = 1, \dots, 360$ enumerates the simulation test results for each method variant (72 angular orientations \times 5 source types = 360 simulation tests). This figure shows that the 2D-Cosine KPCA template-matching method had the best overall performance in accurately determining the horizontal-planar angular orientation of these five neutron source types; however, it is clear from Fig. 5.3.6A that the performance of any variant of the KPCA template-matching method is significantly dependent upon the neutron source type of interest.

5.4 Conclusions and Recommendations for Future Work

Building on the methods discussed in section 4.4, an enhanced template-matching technique—employing kernel principle component analysis (KPCA) Hilbert space transformations—has been presented, providing an accurate means to simultaneously determine the identity (source type/radioisotope) and horizontal-planar angular location of

neutron radiation sources from hand-held moderating-type neutron spectrometer measurements. The kernel PCA concepts central to this technique were rigorously derived, in the context of such spectrometer measurements, to ensure mathematical consistency, and the general KPCA template-matching algorithm was then systematically outlined in terms of preprocessing and real-time analysis steps. Four kernel functions—the two-dimensional (2D) cosine, two-dimensional correlation, three-dimensional (3D) cosine, and three-dimensional correlation—were defined in this work, and their implementation in the general KPCA template-matching algorithm yields four unique method variants. These method variants were then subjected to extensive simulation tests, to compare their efficacy in distinguishing five unshielded source types— ^{252}Cf , AmBe, PuBe, PuO₂, and Pu metal—located at 72 discrete horizontal-planar angular orientations—0° to 355° in 5° increments—relative to the 6C neutron spectrometer (4 method variants × 5 source types × 72 angular orientations = 1440 tests total). For each method variant and each neutron source type tested, the average error in determining the angular source location in the horizontal plane was less than ±2.2°, and the true neutron source was correctly identified in all but one of the 1440 method tests. While all 4 method variants were shown to perform exceptionally well, the 2D-Cosine KPCA template-matching method was most accurate overall. Additionally, although trends in the test results revealed particular strengths and weaknesses of each technique, the performance of all method variants were shown to be significantly dependent upon the neutron source types of interest.

While the simulation tests conducted in this chapter were fairly extensive, the author recommends that future works focus on (1) testing these methods empirically, and (2) drastically increasing the number of source types/radioisotopes and shielded variants

represented in the library dataset. Such an increase would multiplicatively increase the size of the library data set, which would, in turn, yield larger kernel matrices and increase the number of Pearson correlation calculations to perform in the algorithm's real-time analysis steps. It is recommended that these future studies seek an understanding of how such increases in computational complexity, and problem complexity, effect the algorithm's performance in analyzing 6C spectrometer measurements in real time.

CHAPTER 6

METHODS FOR NEUTRON ENERGY SPECTRUM UNFOLDING

6.1 Motivation and Conceptual Introduction

In chapter 3, the empirically measured and/or simulated responses of the instruments discussed therein were introduced as signatures proportional to the kinetic energy of neutrons impinging on their active volumes. A 1-dimensional Pearson correlation-based template-matching technique, which compares these instrument signatures, was then employed to provide both a method for identifying neutron source types/shielding configurations, and an instrument optimization metric, proportional to neutron energy resolution (*vide supra*). While direct analysis of signatures proportional to neutron kinetic energy is beneficial to applications requiring real-time-updating information about radiative neutron sources that pose potential threats (e.g., the majority of non-proliferation operational scenarios, such as vessel visit boarding search and seizure (VBSS) and boarder/port monitoring operations), determination of the local energy-dependent neutron fluence (i.e., the neutron energy spectrum) is ideal and/or necessary for many applications without such time-dependent requirements (e.g., a wide variety of pure nuclear physics, radiation protection/shielding design, nuclear power plant monitoring, and health physics applications; accurate determination of the human neutron dose equivalent was mentioned as an important application at the end of section 3.2.2). Determination of the absolute neutron energy spectrum (an intrinsic property of radiative neutron emissions) from higher-order measurements that are only indirectly proportional to neutron energy requires the solution of an ill-conditioned inverse problem; methods of solution to this problem are known as spectrum “deconvolution” or “unfolding” techniques. To meet the needs of a wider range of

potential applications, numerous spectrum-unfolding techniques were surveyed and tested for potential efficacy in determining neutron fluences from 6C spectrometer measurements. Of the many methods investigated, the maximum entropy method (MEM) was determined to be most logically and mathematically consistent technique for making energy-dependent neutron fluence determinations, based on the information provided by the moderating-type instruments introduced in this work. Thus, following a description of the unfolding problem (section 6.2), section 6.3 will discuss the maximum entropy method, and empirically test its efficacy, in the context of 6C spectrometer measurement analysis. Section 6.4 will then briefly discuss some initial results from an alternative machine-learning approach, employing artificial neural networks (ANNs), and the potential benefits of such methods for future work.

6.2 Neutron Spectrum Unfolding Problem

For instruments capable of multiple independent measurements, such as those introduced in this work, the generalized mathematical representation of the indirect (convoluted) neutron measurement process takes the form of a system of Fredholm integral equations of the first kind

$$N_i + \varepsilon_i = \int_{E_{min}}^{E_{max}} R_i(E) \cdot \Phi(E) dE , \quad i = 1, \dots, n , \quad (6.2.1)$$

where $\Phi(E)$ is the true energy-dependent neutron fluence (which is continuous over the free neutron kinetic energy, E , and assumed here to be unknown; in units of cm^{-2}), $[E_{min}, E_{max}]$ is the energy range of interest, and $R_i(E)$ is a continuous energy-dependent kernel function that describes the convolution process for measurement i (often referred to as the response function for measurement i , and assumed here to be known), resulting in an observed indirect

neutron detection intensity measurement, N_i , with unknown (but possible to estimate) measurement error, ε_i . Solving this system of integral equations for the unknown neutron fluence, in the field of radiation detection and measurement, is referred to as neutron spectrum deconvolution/unfolding.

Since neutron detection intensity measurements are intrinsically discrete (the intensity is simply the number of neutron detections observed in measurement i), even if the measurement errors could be accurately estimated, it is still impossible to obtain a unique and continuous solution for the unknown neutron fluence from only a finite number of such measurements (n in Eq. 6.2.1, $n = 128$ for the 6C spectrometer), regardless of their quantity or the uniqueness and/or variety of their characteristic measurement response functions. It is therefore practical to discretize Eq. 6.2.1, by dividing the energy range of interest into m discretely-binned non-overlapping energy ranges (or subintervals) that cover the entire range $[E_{min}, E_{max}]$. Hence, the neutron fluence and all n measurement response functions are approximated as discrete vector quantities of length m , such that Eq. 6.2.1 becomes

$$N_i + \varepsilon_i = \sum_{j=1}^m R_{ij} \cdot \Phi_j , \quad i = 1, \dots, n. \quad (6.2.2)$$

This expression can also be written in matrix form to include all n available measurements

$$\mathbf{N}_{n \times 1} + \boldsymbol{\varepsilon}_{n \times 1} = \mathbf{R}_{n \times m} \boldsymbol{\Phi}_{m \times 1}. \quad (6.2.3)$$

In this discretized form, the n (the number of available measurements) unsolvable Fredholm integral equations of the first kind (equation 1) are now reduced to a system of n linear equations with m (the number of discretely-binned energy subintervals, chosen at the outset) unknowns. Recalling that any solution, $\boldsymbol{\Phi}_{m \times 1}$, of Eq. 6.2.3 is only a discretized approximation of the true continuous neutron fluence, $\Phi(E)$, this approximation improves as

m increases (i.e., $\Phi_{m \times 1}$ contains more information about $\Phi(E)$ as the energy range of interest is divided into a larger number of smaller subintervals); thus, a large value for m is desired for good energy resolution ($m = 60$ is one industry standard). However, the majority of current-art instruments suffer from a limited number of available measurements ($n \approx 10$ to 20 for some advanced multi-sphere designs, [27]), i.e. equations; far fewer than the desired number of energy subintervals, i.e. unknowns, making Eq. 6.2.3 an underdetermined system of equations ($n \ll m$) for which there are infinitely many solutions. In addition to having an underdetermined system of equations, the measurement response functions for most current-art instruments ($R_{1,j}, \dots, R_{n,j}$ in Eq. 6.2.2) overlap over many orders of magnitude in energy, causing the system of equations to also be ill-conditioned (or ill-posed). That is, for most current-art (and even state-of-the-art) instruments, Eq. 6.3.3 represents an underdetermined and ill-posed system of linear equations for which there are infinitely many solutions, $\Phi_{m \times 1}$, for any given set of observed intensity measurements, $N_{n \times 1}$.

The 6C spectrometer, introduced in chapter 3, offers $n = 128$ simultaneous indirect neutron intensity measurements, allowing for a fully determined system of equations (Eq. 6.2.3) with up to $m = 128$ energy subintervals, and therefore, the theoretical potential for over 2x the energy resolution of current state-of-the-art instrumentation. Note: while these instruments will not be the central focus of this chapter, the 4RP spectrometer also offers 128 neutron intensity measurements, and the 5C offers 3240; however, the 6C spectrometer's highly-optimized moderator-detector design provides most relevant neutron energy information (via its detector response functions) of the instruments introduced in chapter 3. Although the problems associated with underdeterminedness are a non-issue for this novel instrument, the measurement response functions ($R_{1,j}, \dots, R_{128,j}$ in Eq. 6.2.2) are still broadly

overlapping over the energy range of interest, and the system of equations is still severely ill-conditioned (i.e., ill-posed). In the context of this neutron spectrum unfolding problem, the condition number of the response matrix, \mathbf{R} , given by

$$\kappa(\mathbf{R}) = \|\mathbf{R}^+\| \cdot \|\mathbf{R}\|, \quad (6.2.4)$$

$$\text{where } \mathbf{R}^+ = (\mathbf{R}^T \mathbf{R})^{-1} \mathbf{R}^T$$

is the Moore-Penrose pseudoinverse of \mathbf{R} (as obtained from linear least squares; i.e., the LLS solution to Eq. 6.2.3 is $\Phi = (\mathbf{R}^T \mathbf{R})^{-1} \mathbf{R}^T (\mathbf{N} + \boldsymbol{\varepsilon}) = \mathbf{R}^+ (\mathbf{N} + \boldsymbol{\varepsilon})$), is a measure of how sensitive neutron fluence solutions can potentially be to small changes in instrument measurements (i.e., a measure of “conditionedness”). If $\kappa(\mathbf{R}) = 1$, the response matrix is invertible, such that $\Phi = \mathbf{R}^{-1} (\mathbf{N} + \boldsymbol{\varepsilon})$ and unfolding techniques aren’t necessary. If $\kappa(\mathbf{R})$ is small, Eq. 6.2.3 is considered well-conditioned, and if $\kappa(\mathbf{R})$ is large, Eq. 6.2.3 is considered ill-conditioned. For the 6C spectrometer, $\kappa(\mathbf{R}) = 10,023,194.4279$. By the common rule of thumb for condition numbers, this means that solutions to this unfolding problem with the 6C spectrometer can potentially lose up to $\log_{10}(\kappa(\mathbf{R})) \approx 7$ digits of accuracy due to ill-conditionedness alone (i.e., solutions can potentially be very unstable for this instrument, so great care must be taken when choosing a method of solution). Thus, although there are not infinitely many solutions to Eq. 6.2.3, there are three primary difficulties associated with this problem: (1) for any given 6C spectrometer measurement, $\mathbf{N}_{128 \times 1}$, one unique solution for $\Phi_{128 \times 1}$ does not exist, (2) there are likely a very large number of possible solutions, and (3) solution stability can potentially be very poor. This being the case, accurate estimation of the energy-dependent neutron fluence (i.e., neutron spectrum unfolding) becomes a problem of inference, in which one must infer the correct discretized solution from a lengthy list of possible solutions. To narrow down the list of solutions, some form of a priori information

must be introduced. This information is generally incorporated in the form of an initial guess of the solution fluence. In the following section, the maximum entropy method will be employed to search the set of possible solutions for the single solution that is most probable, given all the information available (i.e., 6C spectrometer measurements, its known response functions, and any additional information that can be known a priori).

6.3 Maximum Entropy Method (MEM) Unfolding with the 6C Spectrometer

This section will discuss the MEM algorithm introduced by Marcel Reginatto for the maximum entropy deconvolution (MAXED, [16]) code. The original “few-channel” version of this code was conceived for unfolding neutron energy spectra from advanced multi-sphere moderating-type spectrometer measurements (specifically, the advanced instruments designed by Paul Goldhagen [27]), which typically offer \sim 10 to 20 independent measurements. A “multi-channel” version of the code was later conceived, for unfolding/deconvolving neutron and/or gamma-ray spectra from scintillation detector measurements (e.g., proton recoil and NE 213 neutron scintillators, NaI, BGO, CsI gamma-ray scintillators, etc.), which use multichannel analyzers (MCAs) to characterize the instrument’s charge deposition response (proportional to energy deposition in the scintillator) in the form of a pulse height spectrum (PHS) over a large number of measurement channels (typically 512, 1024, or 2048). Since the 6C spectrometer provides 128 independent measurements, the few-channel version of the MAXED code, which has a hard-coded upper limit for the number of measurement inputs, could not be used for this work. Although the multi-channel version of the code could be used, some important adjustable parameters of this algorithm (discussed briefly in section 6.3.2) were also hard-coded to values that, while they work quite well for most scintillator-type instrument responses, would need to be

adjusted for moderating-type instruments such as the 6C spectrometer. Thus, a python code was written to apply this MEM algorithm to 6C spectrometer measurements.

6.3.1 The Maximum Entropy Method Description

The maximum entropy method defines the set of possible fluence solutions as those that satisfy the two constraint equations

$$N_i + \varepsilon_i = \sum_{j=1}^m R_{ij} \cdot \Phi_j , \quad i = 1, \dots, n \quad [6.2.2]$$

$$\text{and} \quad \Omega = \sum_{i=1}^n \frac{\varepsilon_i^2}{\sigma_i^2} . \quad (6.3.1)$$

where $\sigma_i = \sqrt{N_i}$ is the estimated counting error for measurement i , and Ω is the chi-square test statistic for the solution fluence, Φ . The second constraint equation, Eq. 6.3.1, is included to bound the unknown measurement errors, ε_i , by setting an acceptable value for the chi-square test statistic, Ω , which is generally set equal to the number of available measurements, n (for the 6C spectrometer, $n = 128$). From the set of solution spectra, Φ , that meet these criteria, the MEM seeks the solution that maximizes the relative information entropy, S , given by

$$S = - \sum_{j=1}^m \left[\Phi_j \ln \left(\frac{\Phi_j}{\Phi_j^D} \right) + \Phi_j^D - \Phi_j \right] , \quad (6.3.2)$$

where Φ_j^D is the default fluence (i.e., an initial guess of the solution fluence, based on any a priori information available). The Lagrangian associated with the maximization of S , under the constraint Eqs. 6.2.2 and 6.3.1, is

$$L = - \sum_{j=1}^m \left[\Phi_j \ln \left(\frac{\Phi_j}{\Phi_j^D} \right) + \Phi_j^D - \Phi_j \right] - \sum_{i=1}^n \lambda_i \left[\sum_{j=1}^m R_{ij} \Phi_j - N_i - \varepsilon_i \right]$$

$$-\mu \left[\sum_{i=1}^n \left(\frac{\varepsilon_i}{\sigma_i} \right)^2 - \Omega \right], \quad (6.3.3)$$

where the λ_i and μ are $n + 1$ Lagrange multipliers. Variation of the Lagrangian, L , with respect to these 129 Lagrange multipliers is equivalent to maximization of the potential function

$$Z = - \sum_{j=1}^m \Phi_j^D \exp \left(- \sum_{i=1}^n \lambda_i R_{ij} \right) - \left[\Omega \sum_{i=1}^n (\lambda_i \sigma_i)^2 \right]^{1/2} - \sum_{i=1}^n N_i \lambda_i, \quad (6.3.4)$$

with respect to the 128 Lagrange multipliers λ_i . Additionally, maximization of the potential function, Z , is equivalent to minimization of the cost function, C , with respect to the λ_i .

$$C = \sum_{j=1}^m \Phi_j^D \exp \left(- \sum_{i=1}^n \lambda_i R_{ij} \right) + \left[\Omega \sum_{i=1}^n (\lambda_i \sigma_i)^2 \right]^{1/2} + \sum_{i=1}^n N_i \lambda_i \quad (6.3.5)$$

Once either the potential function, Z , is maximized, or the cost function, C , is minimized, with respect to the n Lagrange multipliers λ_i , the solution fluence that maximizes the relative information entropy is given by

$$\Phi_j = \Phi_j^D \exp \left(- \sum_{i=1}^n \lambda_i R_{ij} \right), \quad j = 1, \dots, n. \quad (6.3.6)$$

6.3.2 Potential Function Maximization or Cost Function Minimization

The ill-conditioned unfolding problem has now been reduced to a non-linear n -dimensional parameter identification problem (Eq. 6.3.4 or 6.3.5) where, once a globally-optimal solution is obtained, the n Lagrange multipliers, λ_i , are then applied, via Eq. 6.3.6, to determine the maximum entropy solution neutron fluence, Φ . Since maximizing Eq. 6.3.4 and minimizing Eq. 6.3.5 are equivalent, either approach may be chosen to determine optimal values for the Lagrange multipliers. However, regardless of the approach taken, a

global optimum is ultimately desired, and this 128 dimensional problem nearly ensures the presence of many suboptimal *local* extrema, essentially discounting the use of conventional optimization techniques. To overcome this difficulty, the few-channel version of the MAXED code uses a stochastic-based method called simulated annealing (an adaptation of the Metropolis-Hastings algorithm that utilizes the tendency of an intentionally “relaxed” convergence process to escape local extrema, [46]) to maximize Z , and the multi-channel version employs a quasi-Newton method called the L-BFGS-B algorithm (Limited memory Broyden-Fletcher-Goldfarb-Shanno algorithm with Box constraints, [47]) to minimize C . Both of these approaches were tested for use in this work, and although both methods performed quite well, the simulated annealing algorithm is a dramatically slower optimization routine than L-BFGS-B. Additionally, the python MEM code using the L-BFGS-B algorithm was found to slightly outperform the simulated annealing version—in unfolding known neutron spectra from simulated 6C responses—once optimal L-BFGS-B parameters were determined (these parameters included initial values and upper and lower bounds, i.e., box constraints, for each λ_i). Thus, the python MEM code utilized in the following section uses the L-BFGS-B algorithm to minimize the cost function, C (Eq. 6.3.5), with respect to the $n = 128$ Lagrange multipliers, λ_i .

6.3.3 6C Spectrometer A Priori Information

The 6C spectrometer software currently utilizes the template-matching techniques introduced in chapters 4 and 5 to identify neutron sources from a library of known reference neutron source spectra (i.e., energy-dependent fluences that are normalized to discrete probability distributions over the energy, $P(E_j)$). Thus, if an instrument operator encounters one of the neutron source types that is represented in the reference library (and it is correctly

identified), then the normalized spectrum, $P(E_j)$, is known and can simply be multiplied by the estimated total fluence, $\|\Phi\|$ (in units of cm^{-2} , constant), and displayed as the local energy-dependent neutron fluence. That is, the estimated (i.e., assuming the measurement errors, ε_i , are negligibly small) total neutron fluence, $\|\Phi\|$, is given by

$$\begin{aligned} \mathbf{N} &\cong \mathbf{N} + \boldsymbol{\varepsilon} = \mathbf{R}\Phi \\ \Rightarrow N_i &\cong \sum_{j=1}^m R_{ij} \cdot \Phi_j = \sum_{j=1}^m R_{ij} \cdot [P(E_j) \cdot \|\Phi\|] = \|\Phi\| \cdot \sum_{j=1}^m R_{ij} \cdot P(E_j) \\ \Rightarrow \sum_{i=1}^n N_i &\cong \sum_{i=1}^n \left[\|\Phi\| \cdot \sum_{j=1}^m R_{ij} \cdot P(E_j) \right] = \|\Phi\| \cdot \sum_{i=1}^n \sum_{j=1}^m R_{ij} \cdot P(E_j) \\ \Rightarrow \|\Phi\| &\cong \left[\sum_{i=1}^n N_i \right] \left[\sum_{i=1}^n \sum_{j=1}^m R_{ij} \cdot P(E_j) \right]^{-1}, \end{aligned} \quad (6.3.7)$$

such that the solution fluence can be closely approximated by

$$\Phi_j = P(E_j) \cdot \|\Phi\| \cong P(E_j) \cdot \left[\sum_{i=1}^n N_i \right] \left[\sum_{i=1}^n \sum_{j=1}^m R_{ij} \cdot P(E_j) \right]^{-1}, \quad j = 1, \dots, m. \quad (6.3.8)$$

However, if the operator encounters a neutron source that is *not* in the reference library, the template-matching algorithms can be used to determine which library reference spectrum is most similar to the *unknown* neutron source spectrum. This reference spectrum can then be used as the default spectrum (i.e., initial guess fluence, based on any a priori information available) in the MEM unfolding algorithm, as described in the previous section, to determine the unknown neutron fluence. In this case, Eq. 6.3.8 is used to scale the default spectrum prior to application of the MEM algorithm.

6.3.4 Empirical Testing

To test the python MEM code's efficacy in unfolding neutron energy spectra, based on 6C spectrometer measurements and the unique a priori information provided by the enhanced template matching techniques introduced in sections 4 and 5, an experiment was conducted at Kansas State University's research reactor facility (Fig. 6.3.1), in which the instrument was exposed to neutron radiation emitted from an Americium-Beryllium, AmBe, (α, n) -type source (i.e., an oxide of ^{241}Am pressed with ^9Be , such that alpha particles— ^4He nuclei—emitted spontaneously from the α -decay of ^{241}Am nuclei, $^{241}_{95}\text{Am} \rightarrow ^{237}_{93}\text{Np} + ^4_2\alpha + \gamma$, are absorbed by ^9Be nuclei and neutrons are emitted, $^9_4\text{Be} + ^4_2\alpha \rightarrow ^{12}_6\text{C} + ^1_0\text{n} + \gamma$) at a 0° source-to-instrument angular orientation. It is worth noting that this particular angular orientation is not necessary, as long as the true orientation is known, and the instrument's response matrix for the true orientation is used. The AmBe source was encased in a shielding container consisting of lead gamma ray shielding and HDPE neutron shielding (Fig. 6.3.1A). A small cylindrical cap in the container was removed (Fig. 6.3.1B), such that neutrons emitted from the source could escape the container, unimpeded, in small-angle cone of possible directions. The 6C spectrometer was positioned at a 0° source-to-instrument angular orientation, such that the center of the container opening was aligned with the central axis of the 6C's cylindrical moderator volume, and was placed at a distance that was chosen to ensure that the cone of unimpeded source neutron directions would cover the instrument's circular "front face" (Fig. 6.3.1C). The shadow shield method, as discussed in section 2.2, was used to account for room scatter effects, and both 6C spectrometer measurements (i.e., one measurement with the shadow shield, and one measurement without, no shadow shield shown in Fig. 6.3.1) were taken for 10 minutes to ensure high counting statistics.

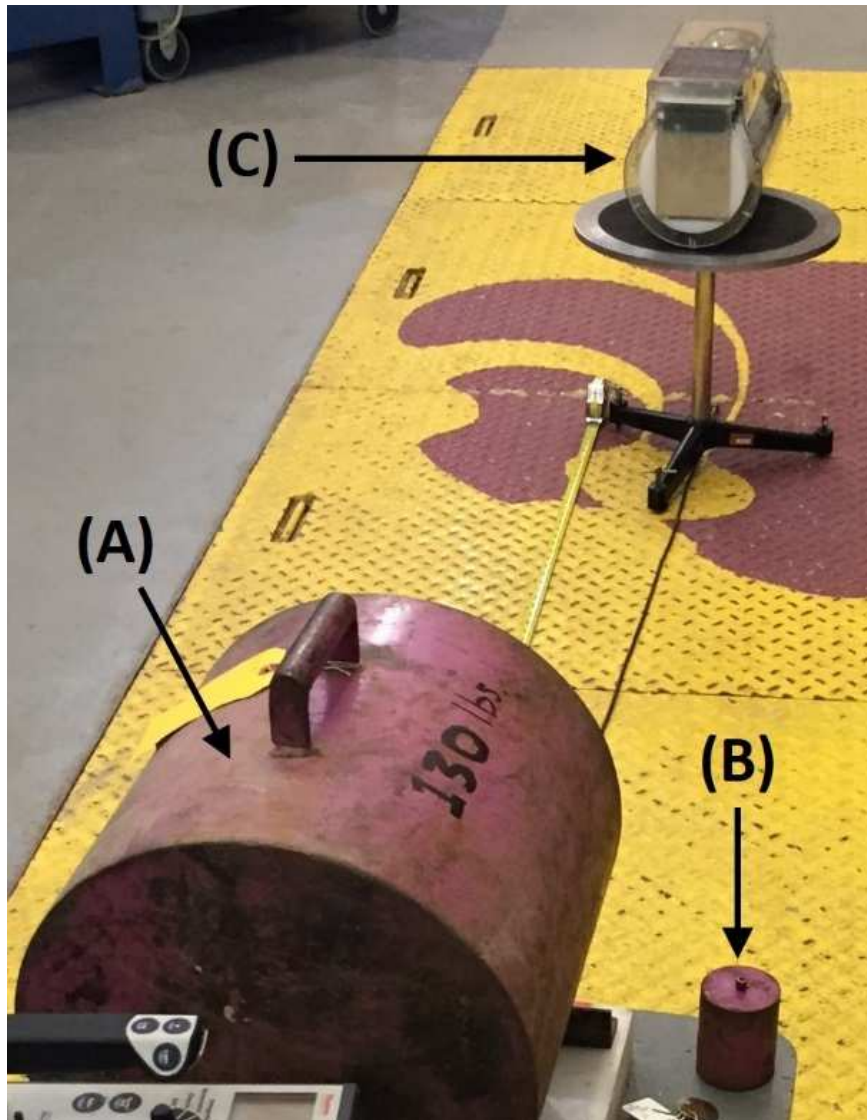


Figure 6.3.1. Photograph of the experimental MEM test setup at KSU, showing (A) an AmBe neutron source inside a Pb + HDPE shielding container, (B) the cylindrical cap of the shielding container (removed), and (C) the location/angular orientation of the 6C spectrometer.

With the AmBe library responses removed from the instrument software's extensive source-type library to simulate an encounter with an unknown source type, the 1-, 2-, and 3-dimensional template-matching techniques, introduced in chapter 4, were then applied to the room scatter-adjusted 6C spectrometer measurement, and unshielded ^{252}Cf was identified as the most similar neutron source spectrum. Using this ^{252}Cf reference spectrum as the default

fluence and measured data from the AmBe source (“unknown” source in this test scenario), the maximum entropy method unfolding algorithm was employed to determine the AmBe fluence. Fig. 6.3.2 depicts the results of this test. Each of the three plots in the figure is simply a different visual representation of the same data; top left is a log-log plot over the entire energy range ($1E-9$ – 100 MeV) to visualize the spectral structure in the low energy region, top right is a log-linear plot over the entire energy range for a more realistic depiction, and bottom center is a log-linear plot over the most important energy range to the majority of practical applications (0.01 – 40 MeV). In each plot, the ^{252}Cf default spectrum is shown in black, the result of the python MEM unfolding code is shown in red, and a reference AmBe spectrum is shown in blue for comparison to the MEM results. Note: the reference AmBe spectrum shown in these figures was obtained from [18], and it is the author’s opinion that this spectrum is likely to be accurate in the high energy range, $>\sim 0.01$ MeV, but since the spectral structure the thermal and epithermal regions appears unphysical, the spectrum is *not* likely to be accurate for energies $<\sim 0.01$ MeV.

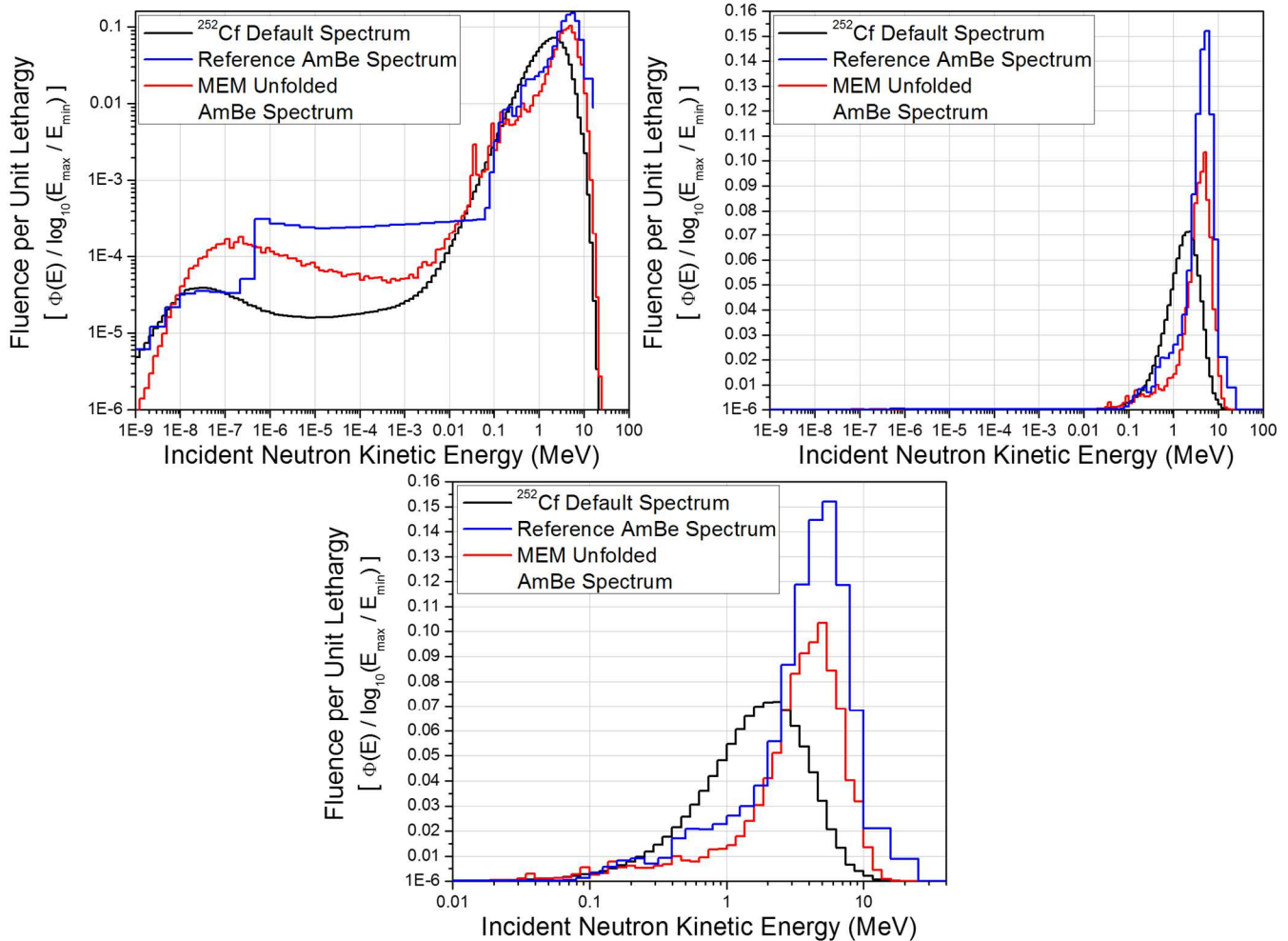


Figure 6.3.2 Maximum entropy method unfolding algorithm results, showing (Top Left) log-log plot $1E-9 - 100$ MeV, (Top Right) log-linear plot $1E-9 - 100$ MeV, (Bottom Center) log-linear plot $0.01 - 40$ MeV. (All Plots) y-axis from $1E-6$ to 0.16 in fluence per unit lethargy.

From this test, it is clear that the maximum entropy method shows great promise for unfolding unknown neutron spectra using 6C spectrometer measurements. Comparing the reference AmBe spectrum (blue), to the MEM unfolded spectrum (red), the benefits of the 6C spectrometer's 128 independent measurements in improving energy resolution (i.e., the 128 measurements allow for a fully-determined system of equations with a 128-energy-bin solution spectrum, the reference spectrum has the IAEA standard 60-bin structure over the

same energy range) are immediately apparent. While this MEM spectrum is in agreement with the reference spectrum in terms of peak position and general peak shape, it also suggests that the reference spectrum's peak-region plateau at \sim 0.4 MeV may be overestimated, and that the large plateau over the entire epithermal region is likely to be unphysical, as predicted. Although the top right plot of Fig. 6.3.2 suggests that the shadow shield method worked quite well, the thermal and epithermal regions of the MEM unfolded spectrum in top left plot show that environmentally scattered neutrons were likely not entirely accounted for; this suggests that the design of the shadow shield (discussed in section 2.2) could be improved upon in future work. The two sharp peaks in the MEM spectrum at \sim 0.035 MeV and \sim 0.09 MeV are likely unphysical artifacts, but this has not yet been confirmed. The author's current theory is that these peaks arise as a mathematical compensation for similarly sharp "dips" that exist in the instrument's response functions near these energies. Although these dips are physically realistic, arising from neutron absorption resonances of materials present in the instrument, application of smoothing techniques to the instrument's response functions, prior to MEM analysis, may eliminate false peaks in unfolded spectra, simultaneously confirming the current theory and improving MEM results. On the other hand, if the author's theory is incorrect, and these peaks in the AmBe spectrum truly exist, then this could be an important result in the field of nuclear physics, made possible by the improved resolution of this novel instrument. Thus, the author recommends investigation of response function smoothing approaches, in application to AmBe spectrum unfolding, for future work. For additional future MEM studies, the author recommends exploration of methods for autonomously optimizing the tunable parameters in the L-BFGS-B algorithm. Optimization of these parameters without human supervision could potentially allow for

neutron energy spectrum unfolding to be performed in the 6C spectrometer software by “non-expert” users.

6.4 Machine Learning Method Employing Artificial Neural Networks

This section presents the first results of a preliminary investigation into alternative machine learning approaches to the neutron energy spectrum unfolding problem, introduced in section 6.2. In the context of this problem (Eq. 6.2.3), instead of utilizing a given instrument measurement, \mathbf{N} , the known response matrix of the instrument, \mathbf{R} , and any a priori information available, Φ^D , to find the most probable solution fluence, Φ , the machine learning approach discussed in this section utilizes a “training” data set of many known instrument measurements, \mathbf{N} , from many known source fluences, Φ , to construct generalized mapping, called an artificial neural network (ANN), that approximates a deconvolution of the a physically convoluted neutron measurement process. Such a mapping would be analogous to constructing a model for \mathbf{R}^{-1} , such that solutions are simply given by $\Phi = \mathbf{R}^{-1}\mathbf{N}$ for any given instrument measurement, except the model for \mathbf{R}^{-1} would likely be highly nonlinear with respect to the measurement and solution fluence. If an ANN can be constructed that is truly capable of generalizing this severely ill-posed inverse problem for a particular instrument, then this network could be used to generate energy spectra from this instrument’s measurements in real time. Thus, although it is not yet known if such a generalization is even reasonably attainable, the potential benefits of the neural network approach are palpable.

Although many complex network designs were tested with the “PyBrain” python package [48], the relatively simple ANN construction discussed in this section produced the most promising results. This network consists of an input layer (instrument measurement layer, 128-dimensional vector, \mathbf{N}), with a linear transfer function ($m \cdot \mathbf{N}$) to a single fully-

connected (i.e., each input is mapped to each neuron, and each neuron is mapped to each output) hidden layer of 100 neurons, n_j , and a hyperbolic tangent transfer function to an output layer (energy spectrum layer, 128-dimensional vector, Φ). Each of the 100 neurons applies 128 weights, w_{ij} , one for each input (12800 weights total), as shown in Fig. 6.4.1.

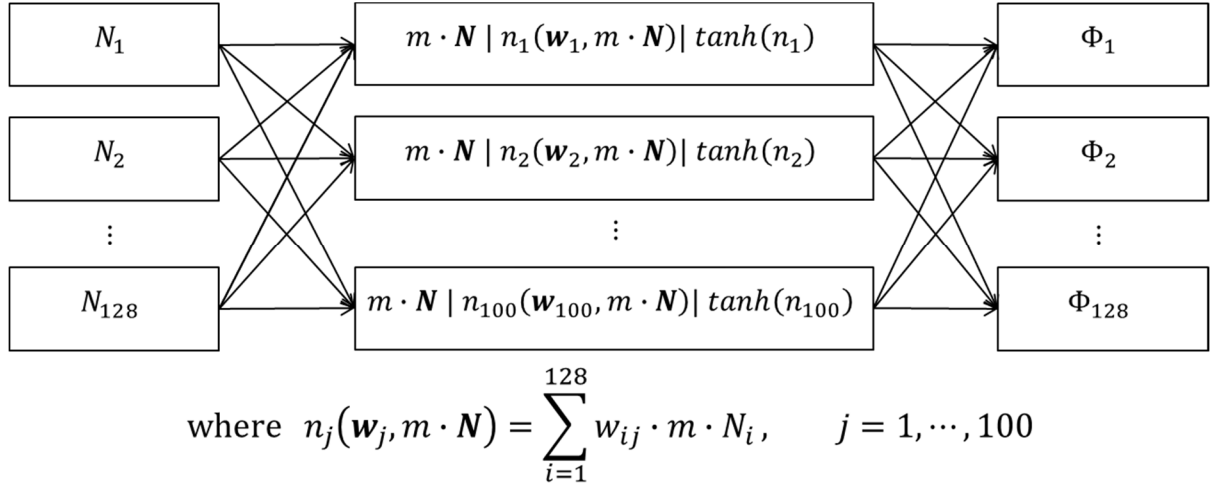


Figure 6.4.1. Artificial neural network construction.

Three different versions of this neural network construction were trained, to test the ANN method's capabilities of unfolding neutron spectra from instrument measurements taken at angular orientations of 0°, 45°, and 90°. To do so, a set of MCNP simulations were conducted, to generate expected 6C spectrometer responses to the ^{252}Cf , AmBe, and Pu metal spectra shown in Fig. 5.3.7, as well as 1"-HDPE-moderated variants of each (6 spectra total), at angles of 0°, 45°, and 90°. These simulations were used to build a training set for each network, with the simulation results used as inputs and the simulated spectra used as outputs. The three networks were trained (i.e., each of the weights, w_{ij} , were adjusted until all

training set inputs approximately mapped to their associated outputs) by applying the error backpropagation method to each training set. Figs. 6.4.2-6.4.4 show the results of each trained network applied to the unshielded training set measurements (indicating how well each network was trained), and Fig. 6.4.5 shows the results of each network applied to a simulated response to a PuBe (α, n) neutron source, to test the each network's predictive capability.

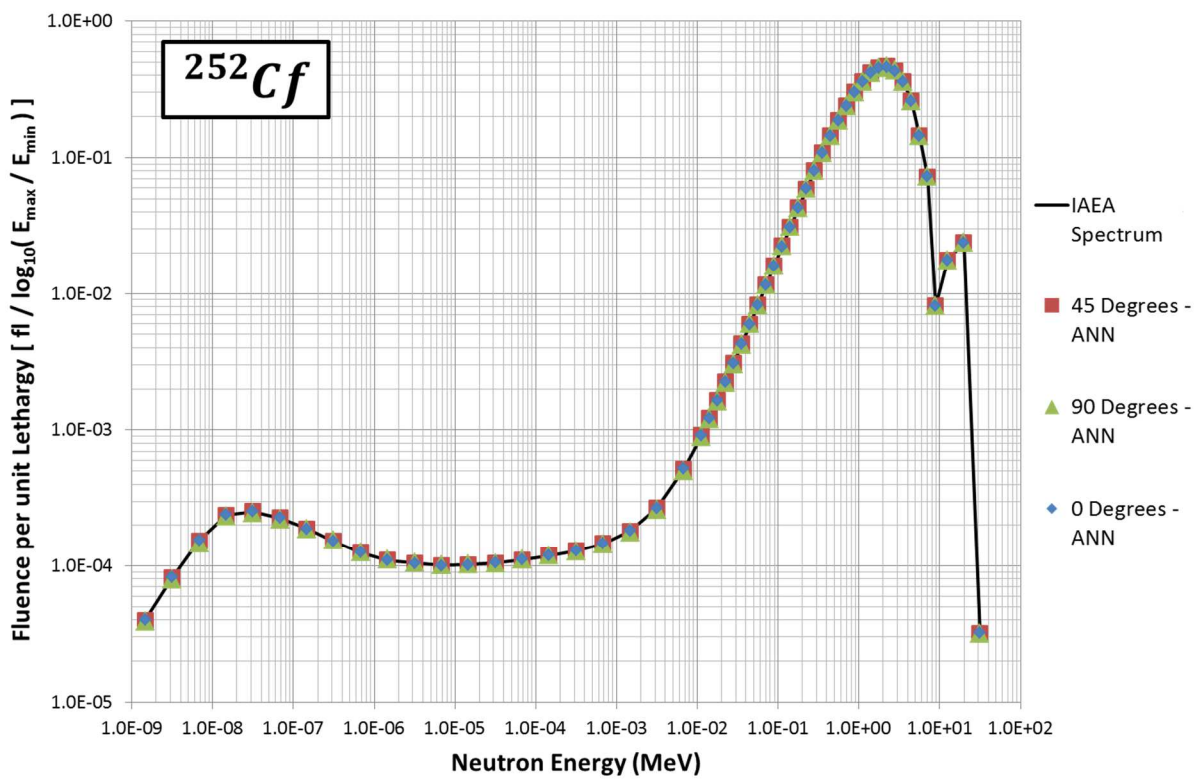


Figure 6.4.2. ANN method applied to ^{252}Cf training set data.

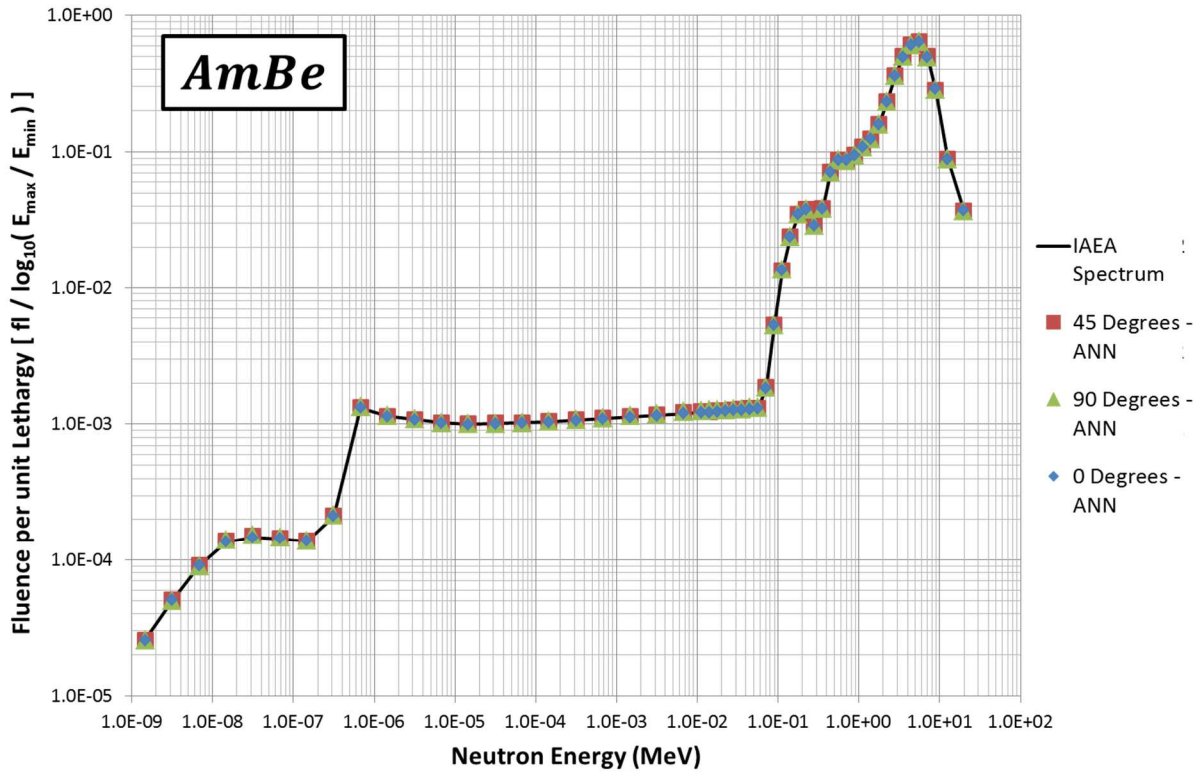


Figure 6.4.3. ANN method applied to AmBe training set data.

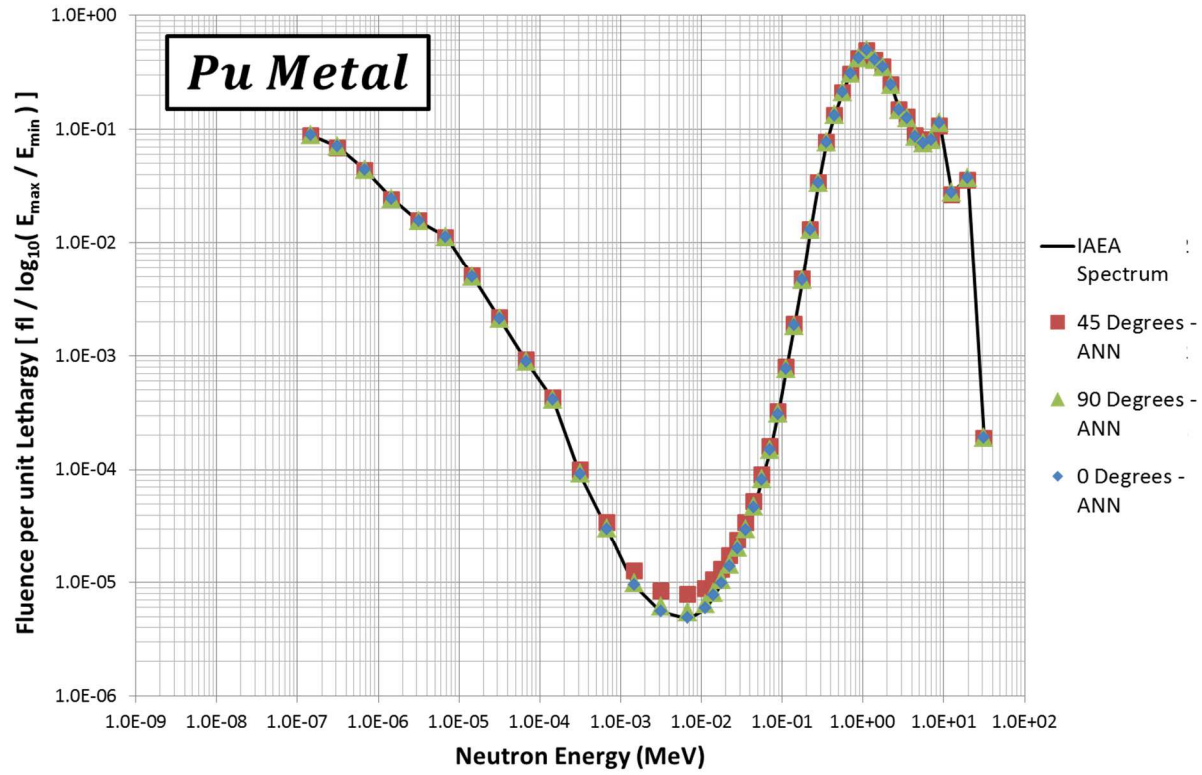


Figure 6.4.4. ANN method applied to Pu metal training set data.

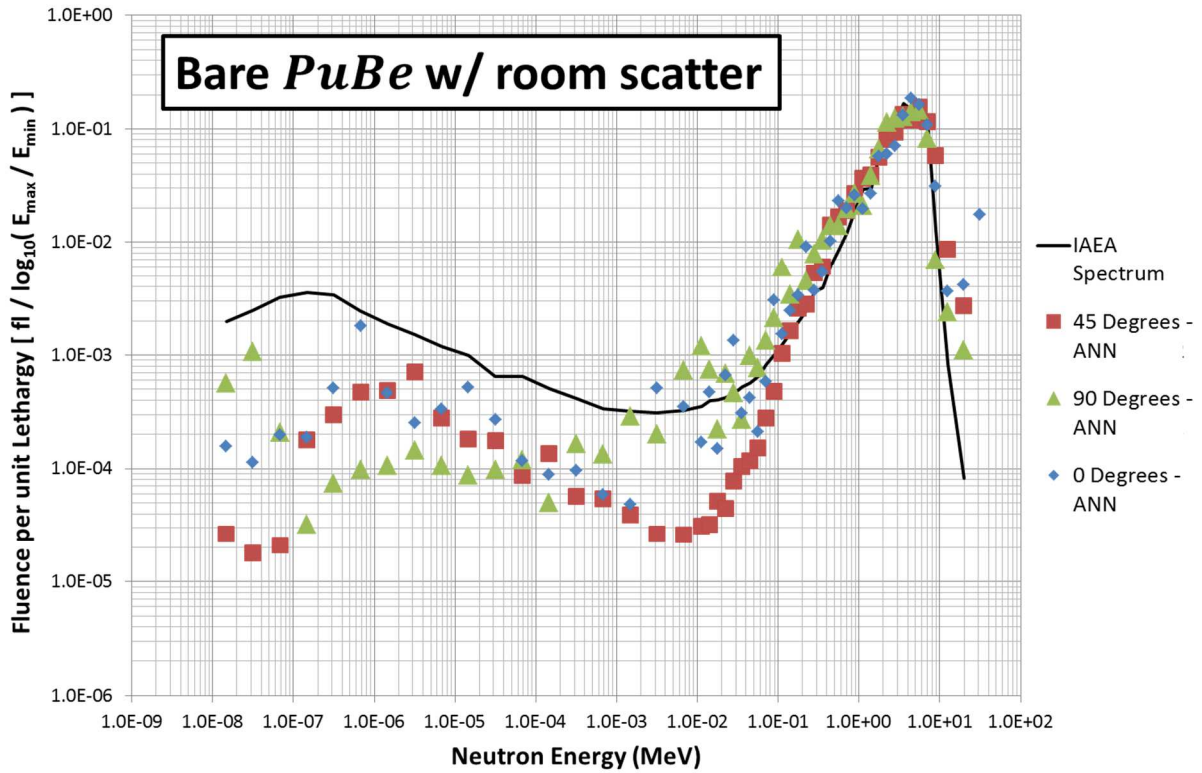


Figure 6.4.5. ANN method applied to simulated PuBe measurement data.

Figs. 6.4.2-6.4.4 show that each of the 3 ANNs trained quite well, with the exception of the 45° ANN's approximation of the low-fluence region in the Pu metal spectrum, ~1 keV to 10 keV. The results of Fig. 6.4.5 show that each ANN correctly predicted the position and general shape of the PuBe spectrum peak, but that each solution fluence begins to diverge below ~100 keV (underestimation), as well as above ~10 MeV (overestimation). Despite these divergences, the results in the peak region are extremely promising, especially since this region of the spectrum is the most significant energy range for the most common neutron source types, spontaneous fission and (α, n) . Additionally, this early attempt at the ANN approach was not necessarily expected to be predictive, since the training data set only included only 6 sets of inputs and outputs, and much larger data sets were thought to be

necessary. This suggests that if the training set size is substantially increased, greater spectrum diversity is introduced, and/or the network architecture is optimized, the ANN method could truly be capable of generalizing the neutron energy spectrum unfolding problem with the 6C spectrometer. Thus, the author recommends further exploration of the ANN concepts discussed in this preliminary work, as well as future investigation into the multitude of alternative methods in the field of machine learning.

CHAPTER 7

REVIEW OF CONCLUSIONS AND FUTURE RECOMMENDATIONS

In this work, four solid-state, moderating-type neutron spectrometers were designed, fabricated, and tested in an effort to improve on the neutron source detection and identification capabilities of long counters and Bonner-sphere-based instruments while making them portable (chapter 3). Through moderator geometry optimization, it was found that an instrument with a cylindrical moderator geometry can achieve a greater intrinsic neutron detection efficiency and greater energy sensitivity than an instrument with a rectangular prism geometry of the same weight. In studying the effects of individual MSND thermal neutron detection efficiency on overall instrument performance, it was shown that increasing the MSND thermal neutron detection efficiency above 22% provides diminishing returns to an instrument's intrinsic efficiency to bare ^{252}Cf . Through theoretical examination of the ratio between an instrument's outer moderator radius and outer detector radius , an outer detector radius of 3.8 cm and outer moderator radius of 7.8 cm (to reflect outbound neutrons) was found to be optimal for a cylindrical instrument of approximately 15 lbs. After investigation of various moderator materials' effects on operational performance metrics, it was shown that increasing the hydrogen concentration of the moderator material drastically increases an instrument's intrinsic neutron detection efficiency and energy sensitivity. In this materials study, high density polyethylene was found to be more optimal for a wider range of applications than the other materials tested. Of the four fabricated spectrometers, the **5C** design exceeds the others in every category of operation, but is the most complex, the most costly to build, and the most physically cumbersome to operate. The **6C**, **4RP**, and **4C**

designs were optimized and built to address the deficiencies of the **5C** design while simultaneously maximizing their individual operational performance, under increasingly restrictive cost and weight constraints, in order to mitigate the unavoidable tradeoffs associated with decreases in moderator volume and/or active detector area. These four instruments are the first representatives of a new class of hand-held, semiconductor-based, moderating-type neutron spectrometers of varying cost, weight, and design complexity, that provide a means to high intrinsic detection efficiency and neutron source identification through real-time energy-sensitive measurements of free neutron fields, ranging from thermal energies to the high end of the evaporation spectrum.

In chapter 4 [49], Two “core” algorithmic methodologies were presented for determining the relative location and the identity of sources of neutron radiation with a volumetrically-sensitive moderating-type neutron spectrometer. Two extensions of—and potential improvements to—these core methodologies were then proposed. The Neutron Response Vectorization (NRV) Method was introduced as the core methodology for determining the location of a neutron source relative to an instrument. It was shown that the NRV method, when applied to empirical 6C spectrometer measurements, provided an accurate determination of the relative horizontal-planar angular location of a bare ^{252}Cf neutron source, in a high-scattering environment, with an average angular error of $\pm 7^\circ$. Pearson product-moment cross-correlation spatial response analysis techniques (in 1, 2, and 3 spatial dimensions) were then introduced as the core methodologies for determining the most probable identity of a neutron source. It was shown that each of these spatial response analysis techniques, when applied to empirical 6C spectrometer measurements, were capable of correctly identifying a bare ^{252}Cf neutron source in less than one minute, and that

increasing the spatial dimensionality of the correlation analysis allows for a greater source identification confidence in less time. A methodological extension of the 2- and 3-dimensional Pearson cross-correlation techniques was then proposed to simultaneously determine the identity of a neutron source and its relative angular location in the horizontal plane. In a set of 432 simulation tests, the correct source type was identified in all trials, with average angular location errors of $\pm 2.5^\circ$ for the 2-dimensional method extension (i.e., a 64.29% improvement to the NRV method results) and $\pm 5^\circ$ for the 3-dimensional method extension (i.e., a 28.57% improvement to the NRV method results). Lastly, a post-hoc improvement to the NRV method, employing a continuous polynomial fit characterization, was proposed (the NRV-Poly method). In preliminary simulation testing, the NRV-Poly method was shown to be a very promising algorithmic improvement, decreasing the angular error from $\pm 24.96^\circ$ to $\pm 0.21^\circ$ (i.e., a 99.16% improvement) in the example discussed in section 4.5.

Through extensive empirical testing on multiple volumetrically-sensitive moderating-type instruments, the core methodologies introduced in this work (i.e., the Pearson correlation spatial analysis techniques and the NRV method) have proven to be accurate and reliable for determining the identity and horizontal-planar location of sources of neutron radiation in a variety of operational environments; however, the methodological extensions introduced in this chapter could provide improved accuracy and reliability, as well as ease of instrument use. While the initial theoretical results are very promising, thorough empirical tests of the two methodological extensions discussed in sections 4.4 and 4.5 have yet to be conducted, and are recommended to be the subject of future work. The author recommends that additional future works focus on extending the angular location methodologies discussed

here to include the vertical dimension, providing a means to real-time neutron-based source imaging with a portable moderating-type instrument.

Building on the methods discussed in section 4.4, an enhanced template-matching technique—employing kernel principle component analysis (KPCA) Hilbert space transformations—was presented in chapter 5, providing an accurate means to simultaneously determine the identity (source type/radioisotope) and horizontal-planar angular location of neutron radiation sources from hand-held moderating-type neutron spectrometer measurements. The kernel PCA concepts central to this technique were rigorously derived, in the context of such spectrometer measurements, to ensure mathematical consistency, and the general KPCA template-matching algorithm was then systematically outlined in terms of preprocessing and real-time analysis steps. Four kernel functions—the two-dimensional (2D) cosine, two-dimensional correlation, three-dimensional (3D) cosine, and three-dimensional correlation—were defined in this work, and their implementation in the general KPCA template-matching algorithm yields four unique method variants. These method variants were then subjected to extensive simulation tests, to compare their efficacy in distinguishing five unshielded source types— ^{252}Cf , AmBe, PuBe, PuO₂, and Pu metal—located at 72 discrete horizontal-planar angular orientations—0° to 355° in 5° increments—relative to the 6C neutron spectrometer (4 method variants × 5 source types × 72 angular orientations = 1440 tests total). For each method variant and each neutron source type tested, the average error in determining the angular source location in the horizontal plane was less than ±2.2°, and the true neutron source was correctly identified in all but one of the 1440 method tests. While all 4 method variants were shown to perform exceptionally well, the 2D-Cosine KPCA template-matching method was most accurate overall. Additionally, although trends in the

test results revealed particular strengths and weaknesses of each technique, the performance of all method variants were shown to be significantly dependent upon the neutron source types of interest. While the simulation tests conducted in chapter 5 were fairly extensive, the author recommends that future works focus on (1) testing these methods empirically, and (2) drastically increasing the number of source types/radioisotopes and shielded variants represented in the library dataset. Such an increase would multiplicatively increase the size of the library data set, which would, in turn, yield larger kernel matrices and increase the number of Pearson correlation calculations to perform in the algorithm's real-time analysis steps. It is recommended that these future studies seek an understanding of how such increases in computational complexity, and problem complexity, effect the algorithm's performance in analyzing 6C spectrometer measurements in real time.

In chapter 6, two methods for neutron energy spectrum unfolding were discussed. The first of these techniques, the maximum entropy method (MEM), was determined to be most logically and mathematically consistent technique for making energy-dependent neutron fluence determinations, based on the information provided by the moderating-type instruments introduced in chapter 3 of this work. Thus, the MEM method was employed to unfold the neutron energy spectrum of an AmBe neutron source from empirical 6C spectrometer measurements, for comparison to a reference AmBe spectrum. While this MEM spectrum was in agreement with the reference spectrum in terms of peak position and general peak shape, it also suggested that the reference spectrum's peak-region plateau at \sim 0.4 MeV may be overestimated, and that the large plateau over the entire epithermal region is likely to be unphysical. Although the results suggested that the shadow shield method (an experimental technique introduced in chapter 2 and used in this test) worked quite well, the

thermal and epithermal regions of the MEM unfolded spectrum showed that environmentally scattered neutrons were likely not entirely accounted for; this suggests that the design of the shadow shield (described in section 2.2) could be improved upon in future work. Two sharp peaks found in the MEM spectrum at \sim 0.035 MeV and \sim 0.09 MeV were determined to likely be unphysical artifacts, but this has not yet been confirmed. To address this, the author recommends investigation of response function smoothing approaches, in application to AmBe spectrum unfolding, for future work. For additional future MEM studies, the author recommends exploration of methods for autonomously optimizing the tunable parameters in the L-BFGS-B algorithm. Optimization of these parameters without human supervision could potentially allow for neutron energy spectrum unfolding to be performed in the 6C spectrometer software by “non-expert” users.

The first results of a preliminary investigation into alternative machine learning approaches to the neutron energy spectrum unfolding problem were presented in section 6.4. The unfolding techniques discussed in this section employed artificial neural networks to unfold neutron energy spectra from 6C spectrometer measurements in source-to-instrument angular orientations of 0° , 90° , and 45° . Application of each network to training set measurement data, from ^{252}Cf , AmBe, and Pu metal source types, showed that the 3 ANNs trained quite well, with the exception of the 45° ANN’s approximation of the low-fluence region in the Pu metal spectrum, \sim 1 keV to 10 keV. Application of each network to simulated PuBe measurement data (not included in the training data set) showed that each ANN correctly predicted the position and general shape of the PuBe spectrum peak, but that each solution fluence begins to diverge below \sim 100 keV (underestimation), as well as above \sim 10 MeV (overestimation). Despite these divergences, the results in the peak region are

extremely promising. Additionally, the tests discussed in this section suggested that if the training set size is substantially increased, greater spectrum diversity is introduced, and/or the network architecture is optimized, the ANN method could truly be capable of generalizing the neutron energy spectrum unfolding problem with the 6C spectrometer. Thus, the author recommends further exploration of the ANN concepts discussed in this section's preliminary work, as well as future investigation into alternative methods in the field of machine learning.

REFERENCES

- [1] A.N. Caruso, "The Physics of Solid-State Neutron Detector Materials and Geometries," *Journal of Physics: Condensed Matter* 22, 443201 (2010).
- [2] T. Goorley, et al., "Initial MCNP6 Release Overview," *Nuclear Technology* 180, 298-315 (2012).
- [3] T. Goorley, "MCNP6.1.1-Beta Release Notes," LA-UR-14-24680 (2014).
- [4] X-5 Monte Carlo Team, "MCNP – Version 5, Vol I: Overview and Theory," LA-UR-03-1987 (2003).
- [5] D.B. Pelowitz, Ed., "MCNPX Users Manual Version 2.7.0," LA-CP-11-00438 (2011).
- [6] M.B. Chadwick, M. Herman, P. Obložinský, M.E. Dunn, Y. Danon, A.C. Kahler, D.L. Smith, B. Pritychenko, G. Arbanas, R. Arcilla, R. Brewer, D.A. Brown, R. Capote, A.D. Carlson, Y.S. Cho, H. Derrien, K. Guber, G.M. Hale, S. Hoblit, S. Holloway, T.D. Johnson, T. Kawano, B.C. Kiedrowski, H. Kim, S. Kunieda, N.M. Larson, L. Leal, J.P. Lestone, R.C. Little, E.A. McCutchan, R.E. MacFarlane, M. MacInnes, C.M. Mattoon, R.D. McKnight, S.F. Mughabghab, G.P.A. Nobre, G. Palmiotti, A. Palumbo, M.T. Pigni, V.G. Pronyaev, R.O. Sayer, A.A. Sonzogni, N.C. Summers, P. Talou, I.J. Thompson, A. Trkov, R.L. Vogt, S.C. van der Marck, A. Wallner, M.C. White, D. Wiarda, P.G. Young, "ENDF/B-VII.1: Nuclear Data for Science and Technology: Cross Sections, Covariances, Fission Product Yields and Decay Data," *Nuclear Data Sheets* 112, 2887 (2011).
- [7] G.F. Knoll, Radiation Detection and Measurement, (John Wiley & Sons, 2010).

- [8] T.M. Oakes, S.L. Bellinger, W.H. Miller, E.R. Myers, R.G. Fronk, B.W. Cooper, T.J. Sobering, P.R. Scott, P. Ugorowski, D.S. McGregor, J.K. Shultis, and A.N. Caruso, “An Accurate and Portable Solid State Neutron Rem Meter,” Nuclear Instruments and Methods in Physics Research Section A: Accelerators, Spectrometers, Detectors and Associated Equipment 719, 6-12 (2013).
- [9] Richard L. Bramblett, R.I. Ewing, and T.W. Bonner, “A New Type of Neutron Spectrometer,” Nuclear Instruments and Methods in Physics Research Section A: Accelerators, Spectrometers, Detectors and Associated Equipment 9 (1), 1-12 (1960).
- [10] Walter J. McNeil, S.L. Bellinger, T.C. Unruh, C.M. Henderson, P. Ugorowski, B. Morris-Lee, R.D. Taylor, D.S. McGregor, Nuclear Instruments and Methods in Physics Research Section A: Accelerators, Spectrometers, Detectors and Associated Equipment 604 (1), 127-129 (2009).
- [11] A.O. Hanson and J.L. McKibben, “A Neutron Detector Having Uniform Sensitivity from 10 keV to 3 MeV,” Physical Review 72 (8), 673 (1947).
- [12] Y. Tanimura, J. Saegusa, M. Yoshida, “Design of a Single Moderator-Type Neutron Spectrometer with Enhanced Energy Resolution in the Energy Range from a Few to 100 keV,” Nuclear Instruments and Methods in Physics Research Section A: Accelerators, Spectrometers, Detectors and Associated Equipment 547 (2), 592-600 (2005).
- [13] H. Tsuji, S. Maeda, H. Tomita, J. Kawarabayashi, T. Iguchi, T. Matsumoto, J.I. Hori, “Epithermal Neutron Response on Moderated Neutron Spectrometer with Multi-Resonance Filters,” Progress in Nuclear Science and Technology 1, 316-319 (2011).

- [14] Andrew C. Stephan and V.D. Jardret, "Neutron Detector," U.S. Patent No. 7514,694 (2009).
- [15] Thomas M. Oakes, "Modeling and Analysis of a Portable, Solid-State Neutron Detection System for Spectroscopic Applications," Ph.D. Dissertation, University of Missouri (2012).
- [16] Marcel Reginatto, P. Goldhagen, S. Neumann, "Spectrum Unfolding, Sensitivity Analysis and Propagation of Uncertainties with the Maximum Entropy Deconvolution Code MAXED," Nuclear Instruments and Methods in Physics Research Section A: Accelerators, Spectrometers, Detectors and Associated Equipment 476 (1), 242-246 (2002).
- [17] Marcel Reginatto, "What Can We Learn About the Spectrum of High-Energy Stray Neutron Fields from Bonner Sphere Measurements?," Radiation Measurements 44 (7), 692-699 (2009).
- [18] R.V. Griffith, J. Palfalvi, and U. Madhvanath, "Compendium of Neutron Spectra and Detector Responses for Radiation Protection Purposes," Technical Reports Series No. 403, Supplement to Technical Reports Series No. 318, Vienna (2001).
- [19] Karl Pearson, "Note on Regression and Inheritance in the Case of Two Parents," Proceedings of the Royal Society of London 58, 240-242 (1895).
- [20] J.K. Shultz, D.S. McGregor, "Design and Performance Considerations for Perforated Semiconductor Thermal-Neutron Detectors," Nuclear Instruments and Methods in Physics Research A: Accelerators, Spectrometers, Detectors and Associated Equipment 606, 608-636 (2009).

- [21] Steven L. Bellinger, R.G. Fronk, T.J. Sobering, D.S. McGregor, "High-Efficiency Microstructured Semiconductor Neutron Detectors that are Arrayed, Dual-Integrated, and Stacked," *Applied Radiation and Isotopes* 70 (7), 1121-1124 (2012).
- [22] Steven L. Bellinger, R.G. Fronk, W.J. McNeil, T.J. Sobering, D.S. McGregor, "Improved High-Efficiency Stacked Microstructured Neutron Detectors Backfilled with Nanoparticle LiF," *IEEE Transactions on Nuclear Science* 59 (1), 167-173 (2012).
- [23] Marcel Reginatto, "Resolving Power of a Multisphere Neutron Spectrometer," *Nuclear Instruments and Methods in Physics Research Section A: Accelerators, Spectrometers, Detectors and Associated Equipment* 480 (2), 690-695 (2002).
- [24] Brian W. Cooper, S.L. Bellinger, A.N. Caruso, R.G. Fronk, W.H. Miller, T.M. Oakes, J.K. Shultis, T.J. Sobering, D.S. McGregor, "Neutron Energy Spectrum with Microstructured Semiconductor Neutron Detectors," *IEEE Nuclear Science Symposium and Medical Imaging Conference Records* 4783-4786 (2011).
- [25] Mark J. Harrison, Q. Cherel, M. Montral, "Design of a Moderated Multidetector Neutron Spectrometer for Optimal Specificity," *IEEE Nuclear Science Symposium and Medical Imaging Conference Records* 4787-4794 (2011).
- [26] Steven L. Bellinger, A.N. Caruso, B.W. Cooper, R.G. Fronk, C.B. Hoshor, D.S. McGregor, W.H. Miller, E.R. Myers, T.M. Oakes, B.J. Rogers, P.B. Ugorowski, J.K. Shultis, S.M. Young, "Apparatuses and Methods for the Localization and Identification of Neutron Sources and/or Neutron Shielding Materials and Neutron Dose Equivalent," U.S. Patent No. 9,081,100 (14 July 2015).

- [27] Paul Goldhagen, "An Extended-Range Multisphere Neutron Spectrometer with High Sensitivity and Improved Resolution," Nuclear Technology: Radiation Measurements and General Instrumentation 175 (1), 81-88 (2011).
- [28] Simon R. Bolding, "Design of a Neutron Spectrometer and Simulations of Neutron Multiplicity Experiments with Nuclear Data Perturbations," M.S. Thesis, Kansas State University (2013).
- [29] Andrea Saltos, "Cross Correlation Calculations and Neutron Scattering Analysis for a Portable Solid State Neutron Detection System," M.S. Thesis, University of Missouri, Columbia, Missouri (2015).
- [30] ICRP, "ICRP Publication 74: Conversion Coefficients for Use in Radiological Protection Against External Radiation," International Commission on Radiological Protection 26, 3-4 (1996).
- [31] Cory B. Hoshor, T.M. Oakes, E.R. Myers, B.J. Rogers, J.E. Currie, S.M. Young, J.A. Crow, P.R. Scott, W.H. Miller, S.L. Bellinger, D.S. McGregor, and A.N. Caruso, "A Portable and Wide Energy Range Semiconductor-Based Neutron Spectrometer," Nuclear Instruments and Methods in Physics Research Section A: Accelerators, Spectrometers, Detectors and Associated Equipment 803, 68-81 (2015).
- [32] A.V. Alevra, H. Klein, K. Knauf, J. Wittstock, "Neutron Field Spectrometry for Radiation Protection Dosimetry Purposes", Radiation Protection Dosimetry 44, 223-226 (1992).

- [33] Eliot R. Myers, "Neutron Response Vectorization and Optimization of Moderating Neutron Spectrometers for Active Interrogation", M.S. Thesis, University of Missouri-Kansas City (2015).
- [34] R.V. Griffith, D.R. Slaughter, H.W. Patterson, J.L. Beach, E.G. Frank, D.W. Rueppel, and J.C. Fisher, "Multi-Technique Characterization of Neutron Fields from Moderated ^{252}Cf and $^{238}\text{PuBe}$ Sources," California University No. UCRL--79483 (1977).
- [35] ISR, "Safety Support Series Volume 1: Radiation Counting Statistics," International Safety Research (2000-2013).
- [36] François Lemay, "Multichannel Statistical Analysis of Low-Level Radioactivity in the Presence of Background Counts," *Health Physics* 103 (6), 770-779 (2012).
- [37] Ivan Idris, NumPy Cookbook, (Packt Publishing Ltd., 2015).
- [38] R.A. Horn and C.R. Johnson, "Matrix Analysis," Cambridge University Press, Cambridge, UK, 146-147 (1999).
- [39] Yoshikazu Uchiyama, A. Abe, C. Muramatsu, T. Hara, J. Shiraishi, H. Fujita, "Eigenspace Template Matching for Detection of Lacunar Infarcts on MR Images," *Journal of Digital Imaging* 28 (1), 116-122 (2015).
- [40] Ruiming Liu, Y. Lu, C. Gong, Y. Liu, "Infrared Point Target Detection with Improved Template Matching," *Infrared Physics & Technology* 55 (4), 380-387 (2012).
- [41] Roberto Brunelli and T. Poggio, "Face Recognition: Features Verses Templates," *IEEE Transactions on Pattern Analysis and Machine Intelligence*, 15 (10), 1042-1052 (1993).

- [42] Nicolas Bourbaki, Elements of Mathematics: Topological Vector Spaces, (Springer, 2003).
- [43] Baback Moghaddam, “Principal Manifolds and Probabilistic Subspaces for Visual Recognition,” IEEE Transactions on Pattern Analysis and Machine Intelligence 24 (6), 780-788 (2002).
- [44] Karl Pearson, “On Lines and Planes of Closest Fit to Systems of Points in Space,” The London, Edinburgh, and Dublin Philosophical Magazine and Journal of Science 2 (11), 559-572 (1901).
- [45] G. Strang, Linear Algebra and Its Applications, (Academic Press, Inc., 1980).
- [46] Scott Kirkpatrick, C.D. Gelatt, and M.P. Vecchi, “Optimization by Simulated Annealing,” Science 220 (4598), 671-680 (1983).
- [47] Richard H. Byrd, P. Lu, J. Nocedal, and C. Zhu, “A Limited Memory Algorithm for Bound Constrained Optimization,” SIAM Journal on Scientific Computing 16 (5), 1190-1208 (1995).
- [48] Tom Schaul, J. Bayer, D. Wierstra, S. Yi, M. Felder, F. Sehnke, T. Rückstieß, J. Schmidhuber, “PyBrain,” Journal of Machine Learning Research 11, 743-746 (2010).
- [49] C.B. Hoshor, E.R. Myers, T.M. Oakes, S.M. Young, J.E. Currie, P.R. Scott, W.H. Miller, S.L. Bellinger, D.S. McGregor, and A.N. Caruso, “Real-Time Neutron Source Localization and Identification with a Hand-Held, Volumetrically-Sensitive, Moderating-Type Neutron Spectrometer,” Nuclear Instruments and Methods in

Physics Research Section A: Accelerators, Spectrometers, Detectors and Associated Equipment 866, 252-264 (2017).

VITA

Cory Blake Hoshor was born on January 8, 1986, in Kansas City, Missouri. He was educated at Pleasant Lea Elementary and Junior High School, and graduated from Lee's Summit High School in Lee's Summit, Missouri, in 2004, earning an A+ scholarship. Mr. Hoshor received an Associate of Arts degree from Longview Community College in 2007, and continued his undergraduate education at the University of Missouri-Kansas City, where he was awarded a Bachelor of Science degree in Mathematics and Statistics in 2010.

In 2011, Mr. Hoshor began a master's program in physics at the University of Missouri-Kansas City. He joined Dr. Anthony N. Caruso's research group as a graduate research assistant (GRA) in January 2012 to study neutron spectrometry. In his time as a master's student GRA, Mr. Hoshor published 1 first-author professional paper, authored 2 major technical reports, coauthored 2 major technical reports, coauthored 2 white papers and 1 full research proposal, gave 2 major conference presentations, coauthored 2 major conference presentations, was issued 2 intellectual property patents, filed 3 invention disclosures, and received an R&D 100 award. As a master's student at UMKC, Mr. Hoshor also served as a graduate teaching assistant (GTA), teaching undergraduate physics laboratories in classical mechanics and electricity and magnetism, and tutoring undergraduate physics students. He was awarded a Master of Science degree in Physics in December 2015.

From January 2016 to the present, Mr. Hoshor has been working toward an Interdisciplinary Ph.D. in Physics with a Mathematics co-discipline at UMKC, and has continued his research in neutron spectrometry. As a Ph.D. student GRA, Mr. Hoshor published a second first-author professional paper, has submitted a third first-author

professional paper for publication, authored 1 additional major technical report (3 total), and coauthored 1 additional major technical report (3 total). Upon completion of his degree requirements, Mr. Hoshor plans to accept a civilian research scientist position with the U.S. Navy.

Mr. Hoshor is a member of the Institute of Electrical and Electronics Engineers and the American Physical Society.